POLITECNICO DI MILANO

Scuola di Ingegneria Industriale e dell'Informazione
Corso di Laurea Magistrale in Ingegneria Elettronica

DEVELOPMENT OF AN IMPEDANCE-BASED DIAGNOSTIC INSTRUMENT FOR MALARIA

Relatore: Prof. Giorgio FERRARI

Correlatori: Ing. Marco GIACOMETTI

Tesi di Laurea Magistrale di

Giovanni BENEVENTO

Matricola 873439

Anno Accademico 2017-2018

Ai miei genitori e ai miei nonni,
per aver sempre creduto in me

Contents

List of Figures

List of Tables

Abstract

This thesis work is part of TidMekii project, winner both of Polisocial Award 2016 edition and Switch2Product 2018 one. In a former work the theoretical validation has been performed as well as a first electrodes' design for a cleanroom produced sensor. Test's working principle relies on the different magnetic behaviour between healthy red blood cells and infected ones: the formers don't exhibit any relevant magnetic property, while the latters show a paramagnetic behaviour. The test is performed by placing a drop of blood on a glass and landing on its top, down-facing, the aforementioned chip equipped with two strong magnets on its back. The separation takes place in that moment and infected cells are pulled toward the electrodes on top of the drop thanks to their magnetic properties, while healthy ones fall on the effect of gravity. By exploiting red blood cells isolating properties, the sensor is able to detect plasmodium's presence in the blood thanks to the liquid impedance variation.
Starting from the study of what was carried on beforehand it the general context is introduced. Then, a theoretical analysis, aiming to explain magnetophoretic working principle, is carried on. Going on, a detailed discussion of the steps followed in the fabrication process at PoliFab is presented.
Then, experimental results are shown, both obtained with hemozoin crystals (parasite's waste) and with bovine treated red blood cells.
On this basis an electronic readout was designed in order to allow a correct acquisition of the signal coming from the sensor. Every choice of the design phase is discussed and analyzed, with particular attention paid to stimulus and reading stages. The system is interfaced with a PC thanks to MATLAB and an Arduino Due, thus obtaining a simple and user-friendly GUI for the on field use.

Riassunto

Questo lavoro di tesi si inserisce nel progetto TidMekii, vincitore nel 2016 del Polisocial Award e dell'edizione 2018 di Switch2Product. In un lavoro precedente è stata svolta la validazione del modello teorico e una prima progettazione degli elettrodi per un sensore fabbricato in cleanroom. Il principio di funzionamento del test risiede nelle diverse proprietà magnetiche dei globuli sani e malati: i primi non godono di rilevanti proprietà magnetiche, mentre i secondi sono paramagnetici. Il test viene effettuato ponendo una goccia di sangue su un vetrino e calando, rivolto verso terra, il chip con due forti magneti alle sue spalle. La separazione tra globuli malati e sani ha inizio e quelli infetti vengono attratti in prossimità degli elettrodi alla sommità in virtù delle loro proprietà magnetiche, mentre i sani precipitano per gravità. Sfruttando le proprietà elettricamente isolanti dei globuli rossi, il sensore è quindi in grado di rilevare la presenza del plasmodio della malaria nel sangue attraverso la variazione di impedenza vista nel liquido in cui è immerso.
Partendo da uno studio di ciò che era stato dimostrato precedentemente viene introdotto il contesto e successivamente ripresa un'analisi teorica che spiega il principio di funzionamento magnetoforetico. Si procede quindi a descrivere i passi seguiti nella fabbricazione dei sensori sviluppati presso PoliFab.
È presente poi una sezione in cui si vanno a mostrare i risultati di esperimenti effettuati sui chip prodotti sia con cristalli di emozoina (lo scarto del parassita), sia con globuli bovini trattati.
Su queste basi si è poi progettata e realizzata un'elettronica che garantisce la corretta acquisizione proveniente dal sensore. Ogni scelta progettuale è discussa ed analizzata, con attenzione particolare agli stadi di stimolo e lettura del sensore. Il tutto viene interfacciato con un PC grazie anche a MATLAB e un Arduino Due, permettendo quindi un utilizzo intuitivo per l'operatore grazie a un programma dalla semplice interfaccia.

Chapter 1

Introduction

1.1 Pathology

Accounting for 200 million cases every year and almost 450 thousands deaths only in 2016 [1] malaria is the predominant parasitic disease worldwide. A very significant area in which malaria has spread is south-eastern Asia, where the estimated cases are roughly around 15 million, but Africa is the most affected area, counting on its own up to 200 million cases as clearly reported in Figure 1.1[1].

	Number of cases (000)					
	African	Americas	Eastern Mediterranean	South-East Asia	Western Pacific	World
Lower 95% CI	176 000	665	3 600	10 900	1 200	196 000
Estimated total	**194 000**	**875**	**4 300**	**14 600**	**1 600**	**216 000**
Upper 95% CI	242 000	1 190	5 900	19 800	2 100	263 000

Figure 1.1: Malaria cases estimate sorted by world area. Cases are shown with 95% lower and upper confidence intervals (CI)

It represents the most significant part of medical budget for over 100 countries with peaks of 40% of the total medical expenses. Equatorial regions are the most affected ones, being Africa the most touched by this problem hosting almost 90% of cases and more than 90% of total malaria deaths as shown in Figure 1.2.
Malaria transmits via the bite of specific infected mosquitoes named *Anopheles*. Malaria occurs in humans when an infected mosquito bites a man injecting *Plasmodium sporozoites*. Once inside a human being these parasites can multiply in the liver in first place (hepatocytes), then in red blood cells (RBCs or erythrocytes). Following generations of parasites can multiply in

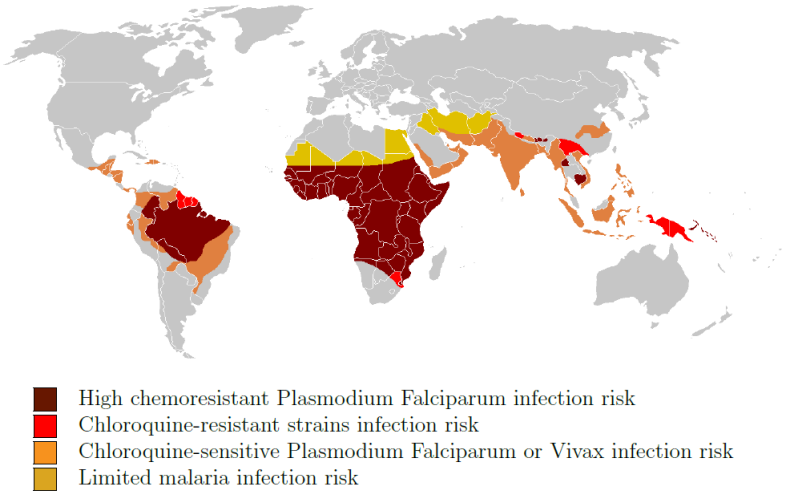

Figure 1.2: Malaria worldwide diffusion map

RBCs and consequently being released by them in the form of *merozoites*. The cycle repeats and when a non infected mosquito bites an infected human it takes away infected blood. In this way it vehicles the plasmodium and makes malaria spreading possible. In other words there are two hosts: mosquitoes which transport the parasite and human beings that make it grow. Indeed mosquitoes do not suffer from parasite presence and therefore they are ideal vectors, on the other hand humans show symptoms. In Figure 1.3 the cycle is visualized.

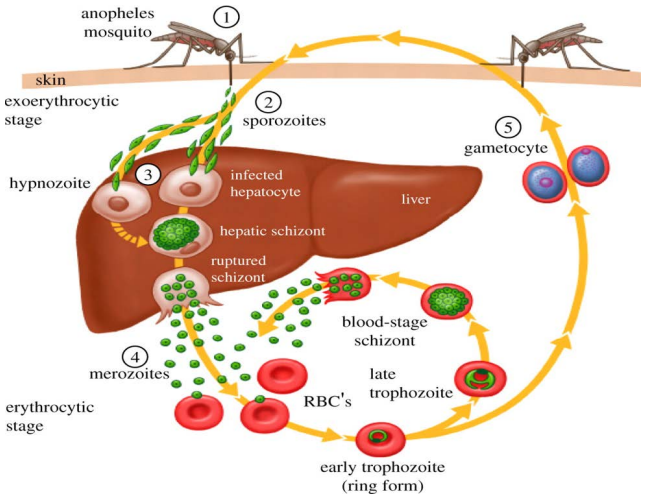

Figure 1.3: Plasmodium life cycle

Plasmodium feeds itselfs with RBC's haemoglobin releasing an insoluble crystal called *hemozoin* until the membrane explodes.
This phase of the infection lasts 24–72 hours in which first symptoms associated with the malaria attack (such as fever, headache and chills) appear, but they are impossible to unequivocally associate to malaria, therefore leading to a difficult early diagnosis. Even if there are several ways to pharmacologically treat this pathology early stage detection is of fundamental importance but right now diagnostic tests are expensive and time consuming, leading to very inefficient population screening.

1.1.1 Hemozoin

Hemozoin crystal (HC) has been proved to include an atom of iron (Fe^{3+}) [2] which in the end is responsible for their magnetic behaviour. It has been proved also to have interesting optical properties like dichroism which causes visible light to be split up into distinct beams of different wavelengths, or which causes light rays having different polarizations to be absorbed in different amounts [3]. For the purpose of this thesis work optical properties will not be taken into account.
RBCs are nearly 2μm thick and have a diameter of approximately 6-8μm [4], while HCs are roughly 1μm x 400nm x 200nm [5] but they are way more numerous being almost 20 times higher in number with respect to infected red blood cells (iRBCs). HCs can have pretty different sizes, and every parasite can produce up to 5 HCs. Various images are shown in Figure 1.4.
In addition to different dimensions and optical properties it has been demonstrated that HCs have paramagnetic behaviour [6, 7]. Therefore also erythrocytes which contain HCs become slightly paramagnetic with respect to the surrounding medium (blood plasma or PBS).

1.2 Prevention and treatment

As said before, malaria is a disease which becomes lethal only if neglected in early stages. Unfortunately malaria's early symptoms are quite general and include fever, headache and nausea, therefore a fast diagnosis is not quite easy to make.
Today's diagnostic tools, discussed more in depth in Subsection 1.2.3, are not very cheap nor extremely fast as they should go through laboratory analysis which can be costly and time consuming.
This project aims to realize a fast and economic on-chip laboratory which can diagnose malaria *in loco*.

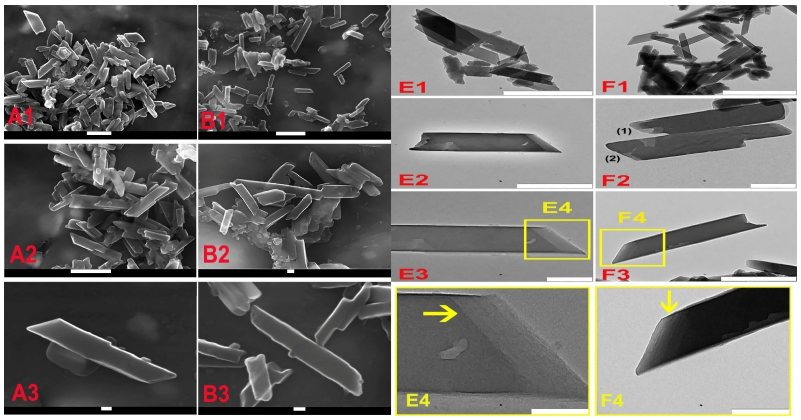

Figure 1.4: Various magnification SEM images showing heterogeneity of shape and size for crystals of native hemozoin from P. Falciparum strains. Yellow arrows and squares indicate the layered structure at the edge of the tips. Scale bars are 1 μm for A1, A2, B1, E1, F1, 500 nm for E2, F3, 200 nm for E3, F2, F4, 100 nm for A3, B2, B3, E4

1.2.1 Social relevance

This project has a social relevance of no doubt resulting even in the winning of Polisocial Award in 2015-2016 edition [8]. Thanks to the user basin and its promising future it also won Switch 2 Product 2018, therefore the social relevance coming from the number of people that could benefit from it.
Thanks to the analysis in Section 1.1, it can now be evident how relevant is malaria as a global problem especially in endemic areas such as Africa, Asia and South America.
Malaria is an extremely well know pathology and it is widely spread in economically disadvantaged places. For instance, it is most present in Africa where lack of diagnostic instrumentation and specific drugs made possible an endemic situation having now impact both at social and economic level.
This project's goal is to develop an early, low cost, fast diagnosis tool to be able to contain malaria diffusion and reduce the time delay between infection and received health care.

1.2.2 Prevention

As previously said malaria has two key hosts: mosquitoes as vectors and humans as incubators. Its prevention strategy therefore can be carried on fight-

ing against mosquitoes spread or against its development inside human beings. The first can be pursued with insecticide-treated mosquito nets (ITNs) and indoor residual spraying of insecticides (IRS). As shown in Figure 1.5(a) more than 40% of sub-Saharan population was not protected by ITNs or IRS. Preventive measures are of vital importance for the groups most at risk, in particular pregnant women and children under 5 years of age. These prevention measures include seasonal malaria chemoprevention (SMC) and intermittent preventive treatment (IPTp) for pregnant women and the corresponding data are shown in Figure 1.5(b)[1].

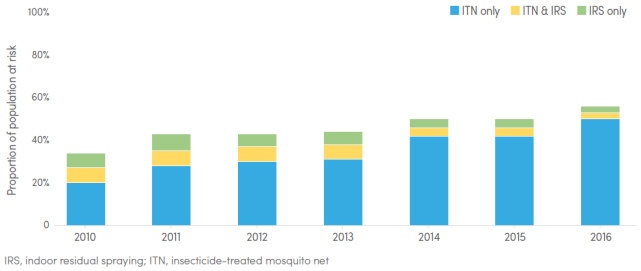

(a) Proportion of the population protected by IRS or sleeping under an ITN in sub-Saharan Africa, 2010–2016

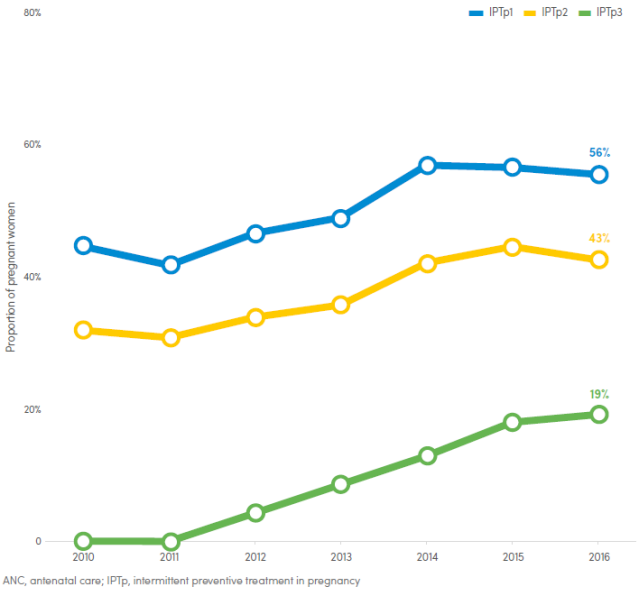

(b) Proportion of pregnant women receiving IPTp, by dose, sub-Saharan Africa, 2010–2016

Figure 1.5: Trend of prevention in sub-Saharan Africa [1]

1.2.3 Treatment

Treatment aims to eliminate Plasmodium parasite from the human circulation. In this way two goals are accomplished: first, and obvious, a human life has been saved, second, but not of less importance, social infection has been contained due to fewer incubators. The way a malaria-ill patient is treated depends on many factors such as the quantity of Plasmodium actually present in his circulation, measured as number of Plasmodium parasites over μl of blood, its developed resistance to drugs and others external factor like being pregnant for women. In the worst cases, or in those cases in which the patient has allergies to drugs to be assumed *per os*, only an intravenous infusion treatment can be carried on. A more radical approach to fight against malaria can be Plasmodium removal by hemodialysis like mPharesis system [9]. This is still in an early research stage and it exploits a magnetic separation as well as Tid Mekii project does. However, the goal is different: Tid Mekii's goal is an early diagnosis, while mPharesis aims to heal a sick patient. Its working principle is very similar to traditional dialysis where in this case an external auxiliary circulation is used to clean blood from iRBCs by separate them from healthy RBCs exploiting their magnetic properties difference with a very high magnetic field gradient.
The mPharesis filter uses a series of cascaded channels through which the infected blood slides in a laminar flow and it is surrounded by said magnetic gradient. This is generated by placing a set of ferromagnetic microstructures close to the former flow where a high force field is created therefore separating iRBCs and healthy ones. This working principle is graphically visualized in Figure 1.6.

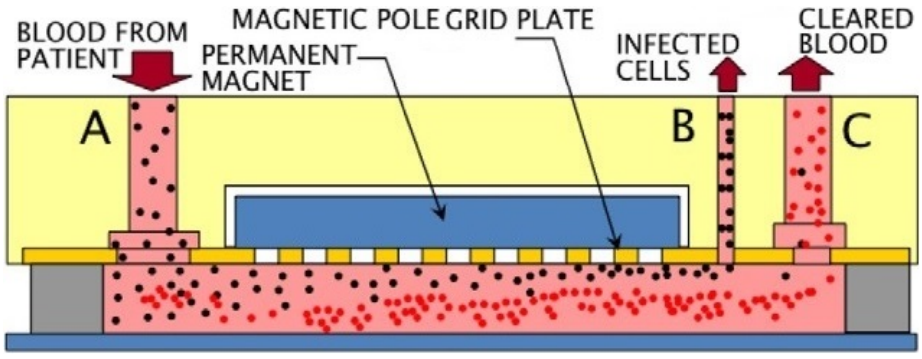

Figure 1.6: Working principle of mPharesis systems [9]

1.3 State of the art

1.3.1 Diagnostic

Nowadays there are various methods to diagnose malaria: the highest sensitivity one being based on gene recognition of the Plasmodium strains through polymerase chain reaction (PCR). Unfortunately this method has many limitations such as fragility and dimensions, thus it is not very popular in Africa. Moreover it should be taken into account that it is not a pan-plasmodic diagnostic test, therefore it is not sensitive to Plasmodium mutations and can even output wrong results not being able to detect the strain causing malaria. It is still considered gold standard counting iRBCs in a blood drop under a microscope. As old-fashioned as it could seem it is a very good compromise between relative quickness, necessary equipment and need of qualified staff [10]. Nevertheless it is not an objective test since there is much space to operator interpretations. A magnetic deposition microscopy could improve the detection effectiveness by magnetically concentrating the infected cells in small areas [11].
Recently a new kind of diagnostic test arise, named "rapid diagnostic tests" (RDTs), which are based on antibody-antigen interaction. In this test a blood drop is commonly obtained from a finger-prick. An antibodies-soaked test strip is put in contact with the aforementioned blood drop, then, when the antigen is captured by the corresponding antibody, it produces a visible coloured line. RDTs provide evidence of the presence of parasites in human blood, and are therefore a valid option as a diagnostic method, particularly where good quality microscopy services cannot be readily provided. This test has been successfully introduced also in Africa. However also in this case the test is not pan-plasmodic since the antigen bounds only with Plasmodium Falciparum, some other cross strains tests have been developed though never reaching true pan-plasmodic standard. Moreover the real downside of this kind of tests is represented by their own cost, and in addition to that they do not exhibit gold standard sensitivity. In addition to that, in an endemic area like Africa, where malaria is common, keeping in mind that antigens remain inside the blood for months, this could lead to false positives.
As briefly mentioned earlier there are some implementation proposals, in which hemozoin crystals sensing happens by means of a magneto-optical (MO) method, magnetically inducing a rotation and then measuring the presence of crystal using a laser [12, 13]. Nevertheless, this solution is not appropriate for the African context due to the complexity of its required instrumentation. TID MEKII project tries to pick the strengths of any other method. A summary of what said before is presented in Table 1.1[10].

Technique	Detectable parasite density (per μL)	Plasmodium species	Infection stage	Sensitivity	Cost (per test)	Operation time (per test)
Microscopy	5-20, 50-100	All species	All stages	Gold standard	5000€ for a microscope, 0.12€-0.40€ per test	30-60 min
RDT	>100	All species	N/A	∼95%	∼1€	∼20min
DEP Deformation	N/A	P. Falciparum	All stages	N/A	<0.1€	Depending on sample volume
Electromagnet with wedge-shaped poles	N/A	P. Vivax, P. Malariae	N/A	∼25%	<0.1€	6-12h
Magnetophoretic between stainless wool in a large chamber	5000 for the first chamber, 50 for the second one	P. Falciparum	Trophozoites and schizonts	N/A	<0.1€	∼15min
Magnetophoretic in a microchannel between two magnets	N/A	All species	All stages	N/A	<0.1€	Depending on sample volume
Magnetophoretic between stainless wool in column tube	400	P. Falciparum	Trophozoites and schizonts	∼95.7%	<0.1€	Depending on sample volume
Magnetophoretic with magnet nanoparticles	30	N/A	N/A	N/A	<0.1€	Depending on sample volume
Magnetophoretic with ferromagnetic material	N/A	P. Falciparum	All stages	∼99%	<0.1€	Depending on sample volume
Magnetic relaxometry	<10	P. Falciparum	All stages	∼100%	N/A	∼30min

Table 1.1: Recap of the state of art diagnostic techniques

1.3.2 Separation

Right now there are only few methods that exploit magnetic properties of hemozoin crystals [11, 14], instead, the most common techniques make use of microfluidic channels.
One of the most popular methods uses a 3-way microfluidic channel to better separate leukocytes and RBCs [15].
Once blood flow is started in that channel an external magnetic field can be applied with the help of a ferromagnetic wire that produces an high magnetic field gradient. By doing this, paramagnetic RBCs are pulled closer to the wire while diamagnetic leukocytes are pushed away from it as shown in Figure 1.7.

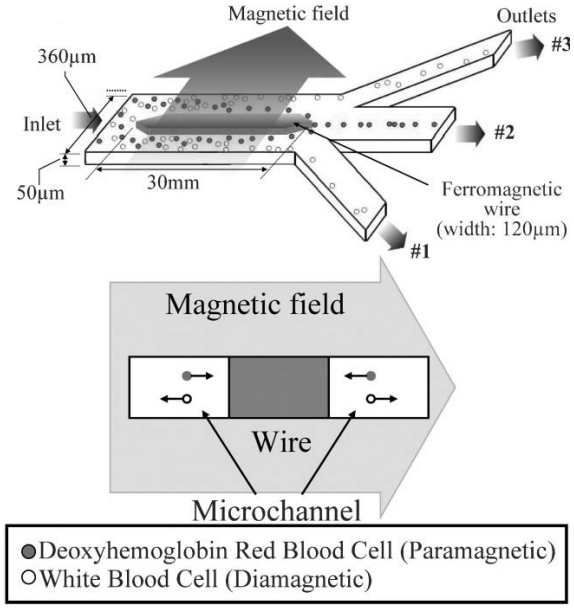

Figure 1.7: Working principle of microfluidic channel

This method can be operated continuously: it is sufficient to force a continuous blood flow through the microfluidic channel. Its main downsides are represented by the intrinsic slowness of such process and the difficulty of use as particles are very different in sizes and some of them can even obstruct the channel.

1.3.3 Detection

A LoC approach offers a simple, cheap and non-invasive way of monitoring biological particles or measuring impedance.

The first developed cytometer was the so-called *Coulter counter* [16] which is still in use nowadays. It measures the DC resistance variation of a particle flowing through a small channel as shown in Figure 1.8.

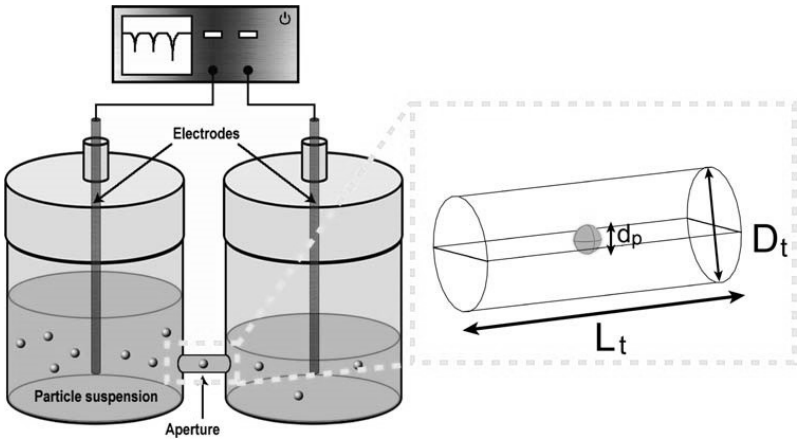

Figure 1.8: Scheme of the Coulter counter

In this test every current pulse correspond to a single particle flowing in the channel. A proportional relationship with the displaced fluid and therefore with the particle size regulates its amplitude.
Of course also AC measurements can be performed retrieving impedance properties to diagnose various diseases affecting cells.
The most problematic aspect of such systems is their dimension-sensitivity trade-off. The more the channel becomes small the more the sensitivity grows. In other words, to obtain a high sensitivity the channel must be very small, thus increasing its obstruction probability. For this reason microfluidic channel based systems are not advisable.
Another important system is based upon interdigitated electrodes (IDE) which are represented in Figure 1.9.
Here, in opposition to what happens in a microfluidic channel, the fluid is not flowing, but it is just laying on top of the electrodes. It can be placed over them with the help of a pipette or it can even surround the whole sensor in techniques employing sensor immersion. Note as well that in this system the contact area between sensed material and electrodes is maximized.
The impedance measurements are usually performed by electrical impedance spectroscopy which substantially measures resistance and capacitance of the electrodes through the solution at different frequencies.

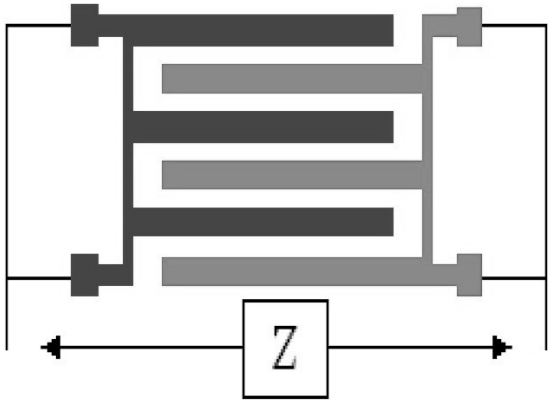

Figure 1.9: Scheme of a IDE configuration, Z is the measured impedance

1.3.4 Lab-on-Chip

A Lab-on-Chip is a device engineered to embed in a single chip various analyses usually performed in a laboratory. Among them operations like counting and detecting both cells and particles are particularly important. Scaling of biochemical operations makes them cheaper, thanks to the need of less sample and agent volume for both device fabrication and analysis. In addition to that, scaling brings advantages in terms of speed thanks to shorter mixing time, higher surface/volume ratio and smaller thermal capacities. Considering all those positive sides in the end a higher control over the whole process can be achieved, thus enhancing performance.
However, detection principles not always advantageously scale as well due to the fact that a high level of miniaturization brings to light unfavourable physical or chemical phenomena that were previously negligible, such as surface roughness, capillary forces and chemical interactions that may now become even predominant. The process used for LoC fabrication is the so called photolithography, explained further in Chapter 3.

1.4 Tid Mekii project

This project's name is "TID MEKII", which is "malaria" translation into Cameroon's dialect. Its goal is to develop a pan-plasmodic diagnostic *Lab-on-Chip* test which has to be fast, but not at the expenses of reliability that must be at least of the same order of today's diagnostic techniques [8]. This test should be used to detect malaria in its early stages on the field, giving to medical staff much more time to take action. For example, 0.002% value of parasitemia is gold standard, therefore this project's target, while roughly at

0.1% - 1% fever attack usually occurs, thus being the most common moment in which a diagnosis is performed.
TID MEKII project also won Polisocial Award 2015/2016 edition, Switch 2 Product 2018 and it is proposed and coordinated by Professor R.Bertacco of NaBiS group.
As briefly said previously this device will separate the magnetic (infected) part of blood containing hemozoin crystals from healthy ones. This way a direct evaluation of parasitemia, defined as the ratio between iRBCs and healthy RBCs, is possible hopefully in an early stage, namely before the first Plasmodium reproductive cycle happening in 48/72 h.

1.4.1 Working principle

This project's aim is to exploit an innovative technology to develop a tiny, low-cost and disposable system, using a Lab-on-Chip approach, which allows scaling and optimization of complex operations right inside the chip. The device is composed by magnetic concentrators into a silicon wafer and measurement gold electrodes on top of that surface. The conceptual scheme described above is represented in Figure 1.10.
The blood drop under test is put into a gasket and in parallel the chip is placed on top of the magnet, then the chip gets flipped facing down and is put on top of the previous mentioned blood drop and gasket. At this point, the generated high magnetic gradient pulls iRBCs and HCs upward toward the surface of electrodes, which in the end detect an impedance variation due to the particles by using electrical impedance spectroscopy. On the other hand, healthy erythrocytes, leukocytes, platelets and thrombocytes do not show paramagnetic properties thus depositing on the bottom of the drop, being pushed toward ground by gravity.
Some key expected features are:

- High sensitivity (5-10 parasites per μL)
- Quickness of the test (<10 minutes)
- Low cost, <1€ for the disposable part and <100€ for the reading part
- Ease of use, without needing qualified staff

Last two points should not be overlooked as they will be those that will allow a wide spread of the device.
In addition to the former features it is important to point out that even what is *not* needed is of fundamental importance in this project as it is addressed to highly economically disadvantaged areas. Some of those are:

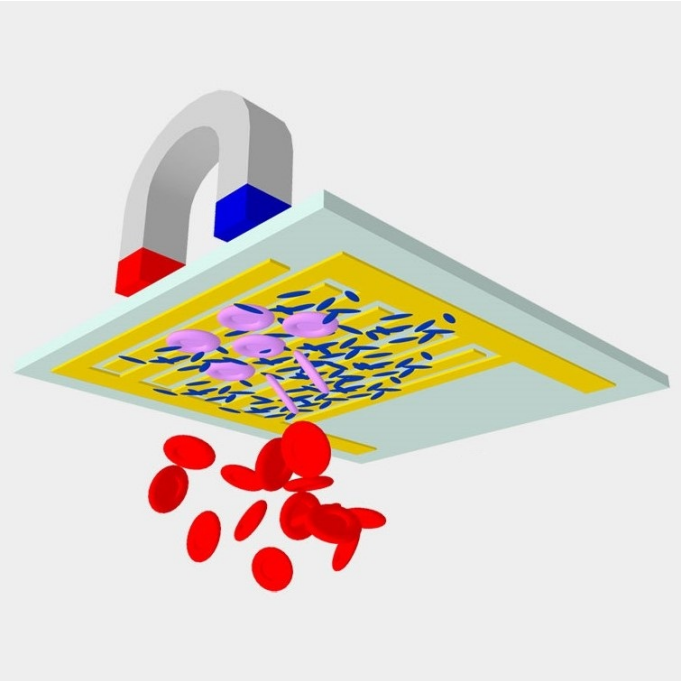

Figure 1.10: Schematic device working principle, showing iRBCs in pink and the smaller HCs crystals getting attracted and healthy RBCs in red staying on the bottom. Gold electrodes are used to sense them.

- Lack intense oscillating magnetic field, created by expensive machines
- No need for unreliable and slow microfluidic processes
- Absence of expensive chemical products

1.4.2 Team Work

TID MEKII project is highly multidisciplinary as Table 1.2 points out.
This project involves many different skills held by various groups. To start, NaBiS group led by Professor R. Bertacco and I^3N by Professor M. Sampietro assessed the project feasibility, then their groups carried on device fabrication. Bovine erythrocytes were provided by μBS Lab that also performed different treatments to simulate malaria infected blood and label iRBCs with a fluorescent marker to use it under a microscope. Another important aspect of the tests performed was to understand what device geometry was actually the most efficient one (more on this in Chapter 2). Human blood samples have been tested only once to make sure that it features the same behaviour

Subject	Related activity	Group
Physics, Magnetism and Nanotechnologies	Development and realization of the magnetic nanostructures	NaBiS (DFIS) Professor R. Bertacco
Electronics	Impedance measures development and realization	I^3N (DEIB) Professor M. Sampietro
Bioengineering	Hematic treatment	μBS Lab (DEIB) Professor B. Fiore
Biology, Medicine, Tropical diseases	Healthy and infected blood harvest. Comparison with gold standard	Tropical Disease Center at Sacco Hospital Professor S. Antinori
Medicine, Tropical diseases	First eld evaluation on a small range of blood samples	COE sanitary operators in Cameroon Dr. B. Lemen

Table 1.2: Work division

as the bovine one, which it did in the end. Bovine blood is easier to manipulate and faster to obtain, therefore successive tests have been carried on with it.
This thesis work, in particular, mainly developed in the actual chip fabrication and then to its electronic readout designing a board suited to that.

Chapter 2

Theoretical and design recalls

In this chapter a brief recall of what has been assessed in the previous thesis work is performed highlighting the key magnetic laws and properties involved in the project.
The second part of this chapter will be devoted to explain how the electrodes design was carried on highlighting the most important features that help a better understanding of the problems.

2.1 Magnetism

When a magnetic field $\mathbf{H}$ is present in the environment every object shows a magnetic induction, also known as flux density $\mathbf{B}$, which depends on the object's magnetic properties. Moreover, the magnetization $\mathbf{M}$ basically describes the magnetic response on the inside of the object, to an external field. The equation linking $\mathbf{B}$, $\mathbf{H}$ and $\mathbf{M}$ are the following Equation (2.1) and (2.2):

$$\mathbf{M} = \chi \mathbf{H} \tag{2.1}$$

$$\mathbf{B} = \mu_0(\mathbf{M} + \mathbf{H}_0 + \mathbf{H}_d) = \mu_0(\mathbf{M} + \mathbf{H}) = \mu_0(1 + \chi)\mathbf{H} = \mu_0\mu_r\mathbf{H} \tag{2.2}$$

where μ_0 is the vacuum permeability constant and μ_r is the one relative to the material, while χ is the volume magnetic susceptibility. Moreover $\mathbf{H}_0$ is the stray magnetic field outside of the object and $\mathbf{H}_d$ is the demagnetizing field inside of it.
Depending on its magnetic permeability, or its susceptibility, given the relation $\mu_r = 1 + \chi$, a material responds differently to an external magnetic field and can be identified as diamagnetic ($\mu_r<1$), paramagnetic ($\mu_r>1$), or ferromagnetic ($\mu_r \gg 1$).
Basically the magnetic permeability describes if an object is attracted ($\mu_r>1$) to an external magnetic field or repulsed ($\mu_r<1$) by it.

Moreover, it is important to notice that paramagnetic and ferromagnetic materials tend to concentrate flux lines, visually depicted in Figure 2.1.

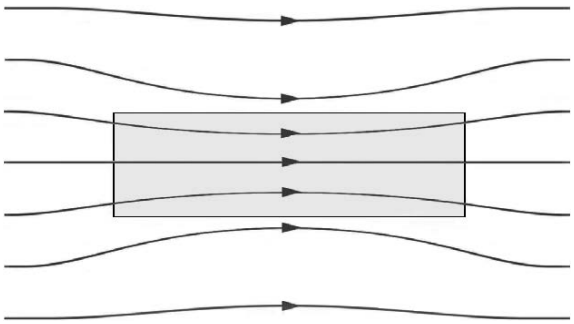

Figure 2.1: A magnetic material (μ_r>1) tends to concentrate flux lines: the higher is χ, the more concentrated are the lines

The magnetic force acting on a single particle suspended in a medium is:

$$F_m = \frac{\mu_0}{2} V_p(\chi_p - \chi_m)\nabla \mathbf{H}^2 \tag{2.3}$$

Where V_p is the particle volume, $\Delta\chi$ is the difference between particle and medium susceptibility.
For this project a magnetic gradient is of fundamental importance to be able to act on red blood cells applying a force to them. Indeed, neglecting buoyancy and drag, a simple force balance can be drawn on a single cell, as depicted in Figure 2.2.

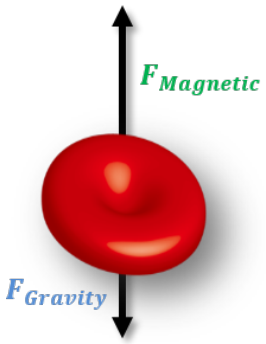

Figure 2.2: Visualization of the working principle of magnetic attraction

If the magnetic gradient is strong enough to create a magnetic force bigger than gravity the cell will be pulled up toward electrodes, thus allowing its

sensing. To create such gradient an array of magnetic concentrators is embedded in a silicon wafer, as it will be discussed more in depth in Chapter 3. To further clarify, Figure 2.3 visualizes this theoretical recall thanks to a simulation where a vectorial sum between a uniform stray magnetic field $\mathbf{H}_0$ and a demagnetizing field $\mathbf{H}_d$ is done, thus assessing the flux density vector $\mathbf{B}$. It is useful to note that the resulting magnetic field has a gradient which is particularly high on the edges of the micro-concentrators, this is what it is used in this project.

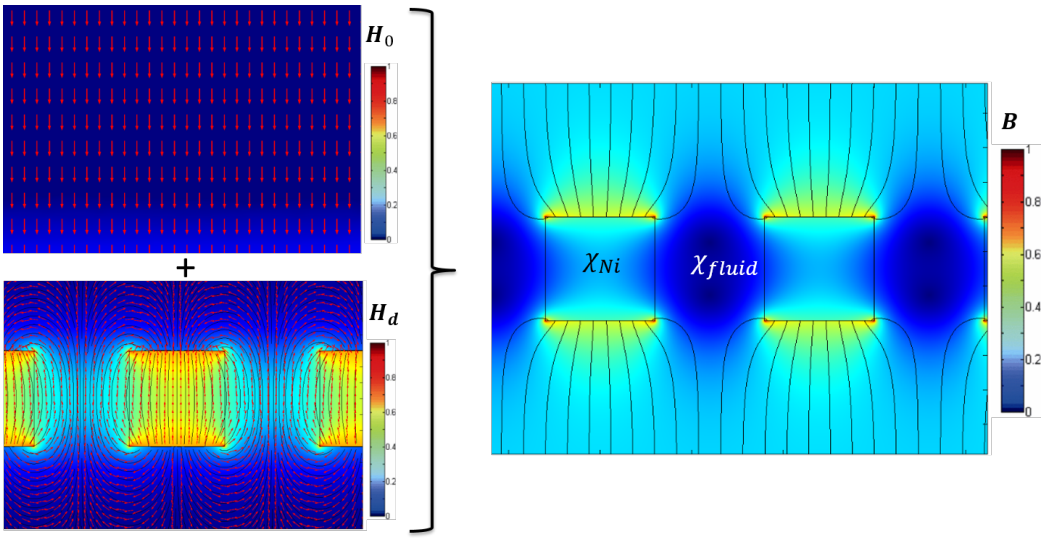

Figure 2.3: Simulation of the vectorial sum of $\mathbf{H}_0$ and $\mathbf{H}_d$ to assess the magnetic gradient in presence of magnetic concentrators

2.2 Electrical impedance spectroscopy

Once magnetic iRBCs have been separated from healthy RBCs it is important to count them using electrical impedance spectroscopy (EIS). It consists of an electrical excitation of the device measuring its response.
The most popular way to implement EIS is performing a voltage frequency sweep and measuring the obtained current. A frequency sweep is basically a set of the same measures differing only on the frequencies at which they are taken. Thanks to this, according to Ohm's first law (reported in Equation (2.4)), a plot showing the impedance dependence on frequency can be drawn.

$$Z = \frac{V}{I} \tag{2.4}$$

The conceptual scheme of EIS in sensor application is shown in Figure 2.4.

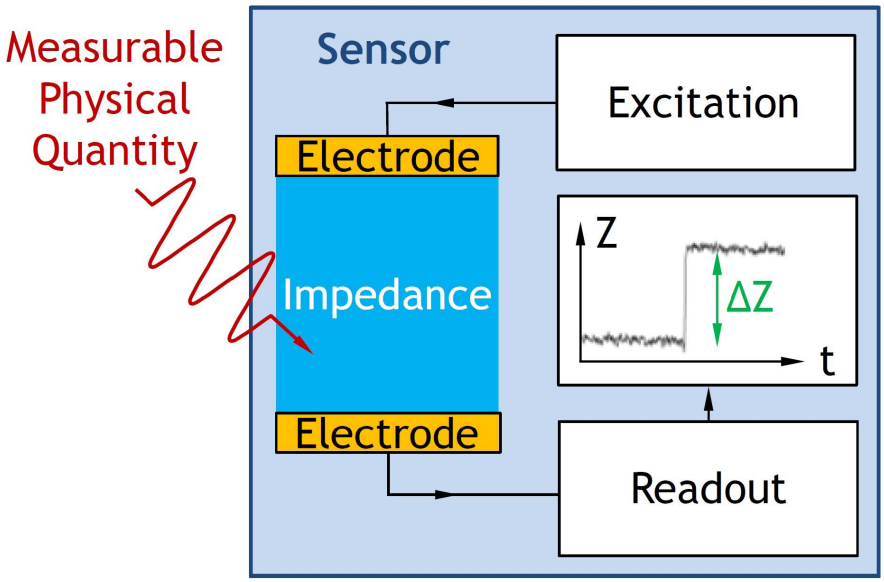

Figure 2.4: EIS working principle

This kind of approach is very much appreciated in biomedical applications, for its promising properties, such as being real-time, and non-invasive above all.
In addition to that it has been demonstrated that EIS can be used directly on blood[3], which is really valuable for a disposable sensor like the one in this project.
The most common configuration for EIS is the one using interdigitated electrodes; in Figure 2.5 some important geometrical parameters are highlighted.

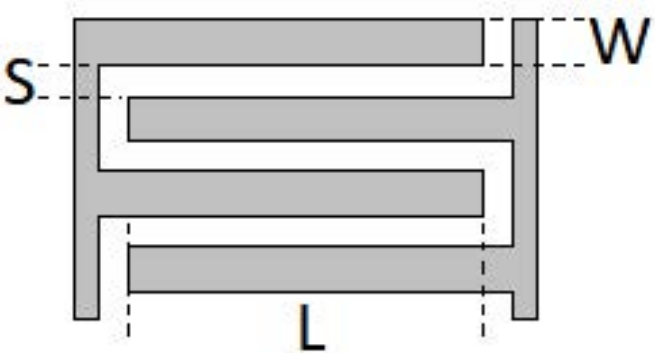

Figure 2.5: Geometrical parameters used for interdigitated electrodes

In Figure 2.6 the simplified electrical model of an interdigitated electrode is shown.

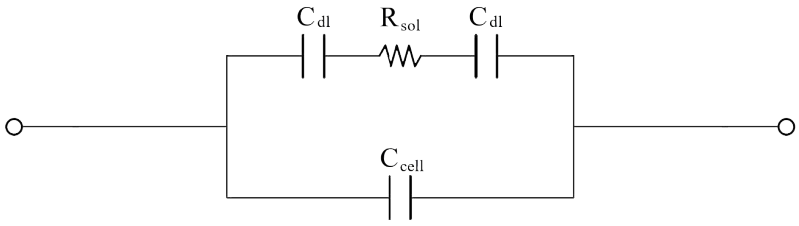

Figure 2.6: Simplified model of an electrode

There is a vast bibliography[17] in which every model's constitutive component is estimated. Electrodes parasitic capacitive coupling C_{cell} as well as double layer capacitance C_{dl} can be assessed by means of Equations (2.5) and (2.6).

$$C_{cell} = \frac{\varepsilon_0 \cdot \varepsilon_{sol}}{K_{cell}} \tag{2.5}$$

$$C_{dl} = \frac{1}{2} \cdot W \cdot L \cdot N \cdot C^0_{dl} \tag{2.6}$$

where C^0_{dl} is the characteristic capacitance of the system per unit area.
Going on, solution resistance R_{sol} can be inferred by using Equations (2.7), (2.8) and (2.9).

$$R_{sol} = \frac{K_{cell}}{\sigma_{sol}} \tag{2.7}$$

where K_{cell} is the cell constant expressed by Equation (2.8)

$$K_{cell} = \frac{2}{(N-1) \cdot L} \cdot \frac{K(k)}{K(\sqrt{1-k^2})} \tag{2.8}$$

The function K(k) is the incomplete elliptic integral of the first kind and it expressed by:

$$K(k) = \int_0^1 \frac{1}{\sqrt{(1-t^2)(1-k^2t^2)}} dt, \qquad k = cos\Big(\frac{\pi}{2} \cdot \frac{W}{W+S}\Big) \tag{2.9}$$

It has been however demonstrated that Equation (2.10) can approximate very well the previous complicated system of equations for $0.1 < \frac{S}{W} < 10$.

$$R_{sol} \simeq \frac{2}{\sigma_{sol}(N-1)L} \sqrt[3]{\frac{S}{W}} \tag{2.10}$$

Where:

- R_{sol} is the solution resistance seen from the electrodes
- σ_{sol} is the solution conductivity
- N is the number of electrodes
- L is the electrodes length
- S is the electrodes spacing
- W is the electrodes width

However, for this project, it is not needed to know exactly the value of the resistance, but only its order of magnitude to successfully estimate the expected thermal noise and the percentage variation given by the infected cells. It is way more important to have a precise knowledge of the resistance variation instead, being it the signal that is going to be read by the subsequent electronics.

2.2.1 Frequency analysis

The cell is made of a conductive internal cytoplasm inside an insulating external membrane. Keeping in mind the presence of the double layer capacitance a frequency modulation is mandatory. Being its cut-off frequency around a few MHz, the signal frequency should be kept under 10 MHz, in order not to bypass the membrane[26]. For this reasons a careful study of electrodes impedance expected spectrum was previously performed leading to the results shown in Figure 2.7.
There are two corner frequencies shown:

$$f_{low} = \frac{1}{\pi \cdot R_{sol} \cdot C_{dl}} \tag{2.11}$$

$$f_{high} = \frac{1}{2\pi \cdot R_{sol} \cdot C_{cell}} \tag{2.12}$$

To have the most reliable readout electronics the measurement frequency should be as low as possible, but a capacitive measurement exploiting C_{dl} is not supposed to give a useful signal as this capacitance varies in the nearest 1 - 5 nm at the electrode-electrolyte interface, so a RBC will not produce a proper variation. Instead f_{high} does not depend on geometrical parameters,

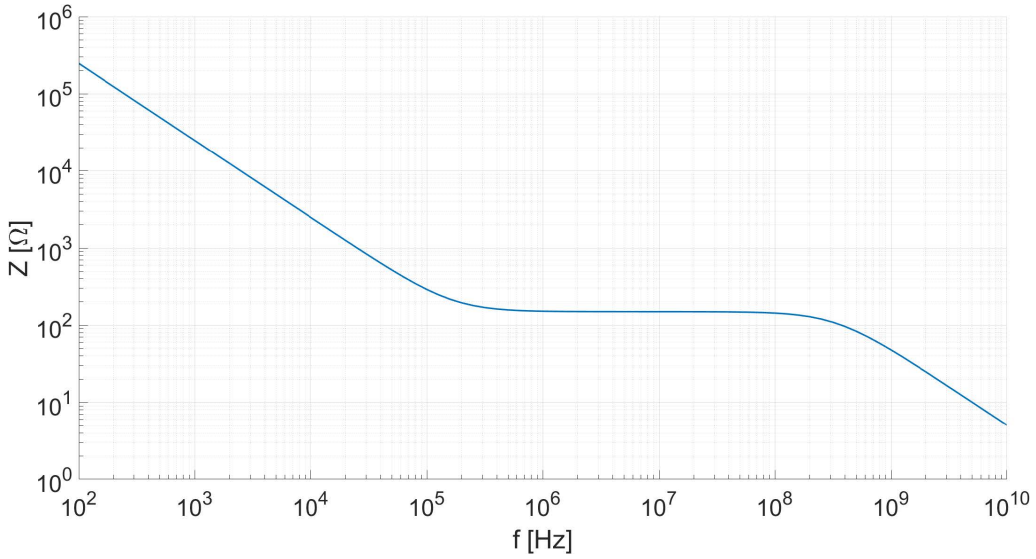

Figure 2.7: Expected impedance spectrum shown by the electrodes, where a large resistive plateau is desired

but anyway it is not exploitable since it is placed around 100MHz, but at 10MHz there is a limit given by RBCs as explained before. At medium frequencies, namely between 1 and 10 MHz there is a resistive plateau, which can be widened by moving f_{low} to lower frequencies, by acting on electrodes geometry. This is not easy since increasing C_{dl} requires a considerable effort, the only other way is to increase R_{sol}. This can be achieved by reducing electrodes number N (and so the total area, being the capture efficiency equal), their length L, or the $\frac{S}{W}$ ratio, assuming that σ_{sol} is set by the medium. However this would not lead to any benefit as the double-layer capacitance would decrease as well, so the pole would not move at all. In the end W is the only parameter that represents a true degree of freedom in this design without affecting significantly C_{dl} as shown in Equation (2.13).

$$f_{low} \simeq \frac{\sigma_{sol}}{\frac{\pi}{2} \cdot K_{cell} \cdot W \cdot L \cdot N \cdot C_{dl}^{0}} \simeq \frac{\sigma_{sol}}{\pi \cdot C_{dl}^{0} \cdot W} \tag{2.13}$$

So, by estimating the solution conductivity around 1 $\frac{S}{m}$, C_{dl}^{0} of about 0.2 $\frac{F}{m^2}$ an electrode width of 3 μm was chosen. With those parameters, a f_{low} around 500 kHz was estimated, which must be compared with the results obtained and shown in Figure 2.7.

2.2.2 Percentage variation

As said above impedance variation is the key detection parameter, as it produces the signal that the following readout electronics will use to understand if the blood was indeed infected or healthy. Moreover, impedance percentage *variation* is of fundamental importance, rather than its absolute differential value, because of two issues.
Firstly, temperature variation of the solution over time, since this is expected to be a slow measurement. This produces a drift due to the fact that solution resistivity changes of about 2% per K, which can overwhelm the expected impedance variation due to the particles. Some faster temperature fluctuations, in the order of seconds, are present as well and can hinder the measure.
The second issue is about noise. The dominant contribution is the well-known thermal noise[18].
It can be both expressed in terms of equivalent voltage spectral density (Equation (2.14)) or current one (Equation (2.15)):

$$\overline{E_n^2} = 4 \cdot k_b \cdot T \cdot R_{sol} \tag{2.14}$$

$$\overline{I_n^2} = \frac{4 \cdot k_b \cdot T}{R_{sol}} \tag{2.15}$$

Where:

- k_b is Boltzmann constant
- T is the absolute temperature of the conductor
- R is the resistance of the conductor

Flicker noise is not of interest, since its contribution becomes negligible in the MHz range, where this measurement is expected to be taken.
To address the impedance variation of a solution with particles inside, also called mixture, Maxwell mixture theory was used[4]. From this Equation (2.16) was derived:

$$\sigma_{mix} = \frac{1 + 2\Phi\left(\frac{\sigma_p - \sigma_m}{\sigma_p + 2\sigma_m}\right)}{1 - \Phi\left(\frac{\sigma_p - \sigma_m}{\sigma_p + 2\sigma_m}\right)} \tag{2.16}$$

where σ_p is the conductivity of the particle (RBC or HC) and σ_m the one of the medium (plasma or PBS), while Φ is the volume fraction, namely solution's concentration. To correctly apply Maxwell mixture theory Φ must be

below 10%, and by supposing that $\Phi \ll 1$, Equation (2.16) can be approximated with Equation (2.17)

$$\sigma_{mix} \simeq \sigma_m \cdot \left(1 + 3\Phi \frac{\sigma_p - \sigma_m}{\sigma_p + 2\sigma_m}\right) \tag{2.17}$$

In this project's case RBCs are insulating, therefore it can be assumed that $\sigma_p \ll \sigma_m$. Moreover, by writing this relation in terms of resistivity Equation (2.18) is assessed:

$$\rho_{mix} \simeq \rho_m \left(1 + \frac{3\Phi}{2}\right) \tag{2.18}$$

By taking S = W in Equation (2.10) and performing the difference between mixture and solution (or medium) resistance Equation (2.19) is assessed:

$$\Delta R = R_{mix} - R_{sol} = \frac{2}{\sigma_{mix}(N-1)L} - \frac{2}{\sigma_{sol}(N-1)L} \tag{2.19}$$

Finally, impedance percentage variation was inferred:

$$\frac{\Delta R}{R} = \frac{3}{2} \cdot \frac{V_p}{(2N-1) \cdot L \cdot W \cdot H} \tag{2.20}$$

where H is the sensitive height of the electrodes and V_p is total particles' volume. It is important to notice that σ_{sol} does not appear in Equation (2.20).

2.3 Electrical model

In the measurement frequency range roughly of 1MHz to 10MHz the resistive part R_{sol} is the most significant part of the impedance. A deeper analysis of the parasitic effects will now be carried on.

2.3.1 Parasitic effects

A parasitic effect is an unwanted behaviour for any component not showing only its ideal properties. In biomedical applications, especially at sensor level, parasitic effects often imply unwanted capacitances, more rarely resistances or inductances. In Figure 2.8 the complete model of the device is shown and it will now be explained in more detail.
Two main parasitic components are expected in this device, namely due to substrate and solution, plus other minor parasitic ones.
The first is present due to the fact that SiO_2 acts as a dielectric over a

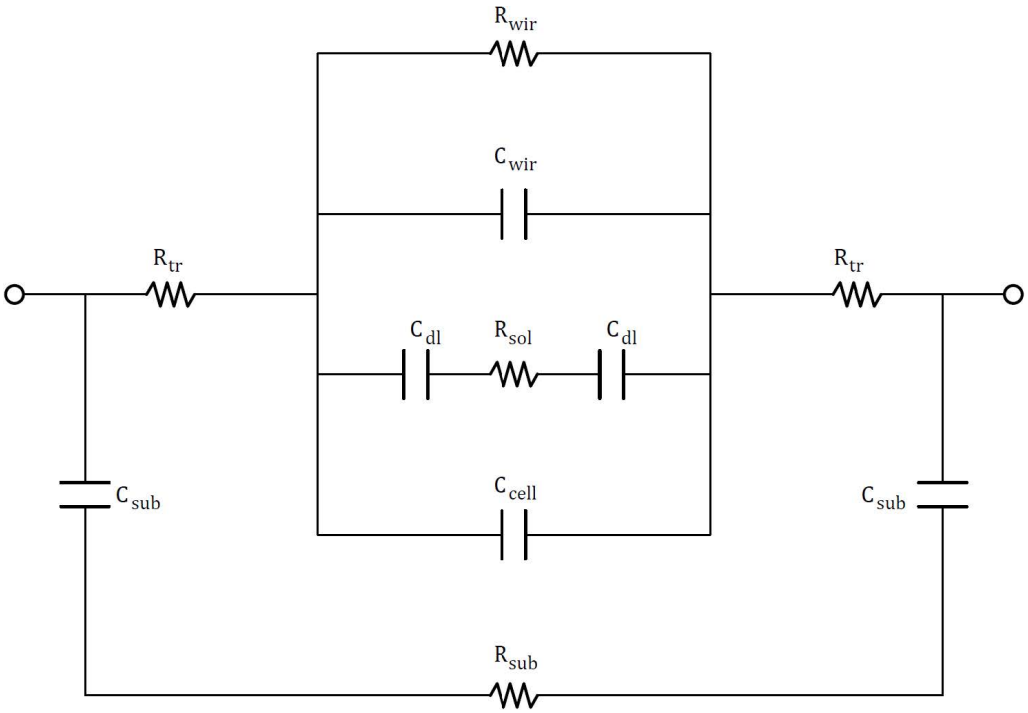

Figure 2.8: Complete electrical model of the device with brief definitions:

- R_{sol}: solution resistance
- R_{tr}: pads to active area metallic resistance
- R_{wir}: trace to electrodes metallic resistance
- R_{sub}: substrate resistance
- C_{dl}: double-layer capacitance
- C_{wir}: wirings capacitance across the solution
- C_{sub}: substrate capacitance
- C_{cell}: electrodes capacitance across the solution

conductive substrate like silicon thus forming a parallel plate capacitance which shows a low impedance in the high frequency range therefore becoming the preferred path for currents and limiting the possibility to perform high frequency measurements. This effect is proportional, in first approximation, to the total area A of gold deposited on the substrate to form electrodes and inversely proportional to the distance d separating the two plates, which is SiO_2 thickness actually. So:

$$C = \varepsilon_r \varepsilon_0 \frac{A}{d} \tag{2.21}$$

The biggest contribution to this kind of parasitic effect is given by connection pads being them almost $(1\text{mm})^2$. In a previous thesis work they were eliminated directly bonding the chip to an external PCB. It must be noted, though, that bondings are very difficult to manage in a experimental environment, even more so if samples are biological. In this case there is the need to properly wash the chip after every experiment, which will brake bondings. On the other hand realizing a disposable system in this phase of the project was not a viable solution, hence the need for a more robust connection.
Now, in fact, pads are linked to the PCB by means of a spring contact set by Mill-Max. Those are mounted on top of an auxiliary interface PCB fabricated in PoliFab, where its probes are in contact with pads ending into a Picoblade connector which is used to allow the communication between the auxiliary interface PCB and the external world.
Another capacitive parasitic effect is given by the solution which at sufficiently high frequency acts as a dielectric material in such a way to insulate the conductive electrodes and the wirings which have different polarities. The effect of electrodes' capacitance has been measured to be evident at very high frequencies well beyond the measurement interval.
Instead, at low-to-medium frequency, an effect called *double-layer* arises and it is covered more in depth in the following subsection.
Resistive parasitic effects are mainly due to wirings and traces of all the electrodes, with the latter that happens to be electrically in series to R_{sol} and can even be dominant if not carefully designed.

2.3.2 Double-layer capacitance

Depending on their behaviour in liquid,, electrodes are divided into two categories: polarizable and non-polarizable[19]. The first category behaves like a capacitor and for instance inert metal electrodes belong to this category (like gold, platinum and titanium). When in contact with an electrolyte solution, like phosphate buffered saline (PBS), an intrinsic charge density due to an excess of electrons at the electrode-electrolyte interface[19–22] will

arise because ions cannot react with the metal as it is inert so they can only accumulate in a thin layer at the interface near the electrodes (up to a few nanometers), as illustrated in Figure 2.9.

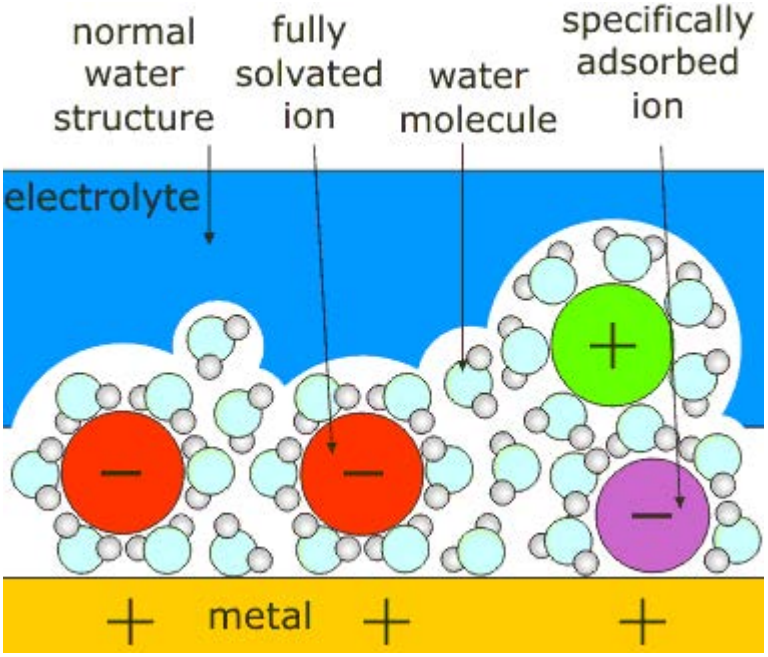

Figure 2.9: Scheme of the formation of a double-layer capacitance

Double-layer capacitance happens to be in series with the solution resistance, therefore, at low frequency, it is the most predominant contribution of the total impedance, hence the need to use a modulation. It has been proved that a constant phase element (CPE) would be a better model for this phenomenon[23], but for the sake of simplicity it will be treated as a capacitor. In addition to that, as it has been already decided to use a modulation, what happens at low frequency is not very relevant. What is really important, on the contrary, is the low frequency pole which must be pushed as low as possible to increase the frequency width of the resistive plateau. It is not an easy task though because to decrease its frequency one should increase C_{dl} on purpose thus increasing electrodes area which goes to the detriment of the relative variation of the solution given by a single infected cell.
On the other hand, a non-polarizable electrode features an ideally constant interface potential, even when a high current is passing through it. Using non-polarizable electrodes would be an effective way to completely remove the double-layer effect, using materials such as silver-silver chloride which is not inert[19, 24, 25]. In addition to that, they tend to erode pretty quickly and are difficult to be done in microfabrication.

For this project polarizable electrodes are used, bringing the advantage of not having reactions in the liquid but also the main disadvantage of the double layer capacitance which in turn leads to a mandatory modulation to bypass it and successfully read an analog signal.

2.4 Differential measurement

A differential measurement can be exploited to enhance resolution and sensitivity of the system.
Medium fluctuations, for instance drifts in temperature, are relevant, but they can be assumed approximately constant across a single droplet, therefore, by having a reference electrode right on the side of the measurement one, they will electrically produce a common mode signal which can be discarded with a differential measurement. In an ideal situation, the current flowing through the two electrodes should be equal, and the resulting current would be:

$$I = I_{meas} - I_{ref} = 0 \tag{2.22}$$

Now, being RBCs insulating, if one of them lands on top of a measurement electrode it will produce a lower current, therefore an unbalance will be present and a signal arises. What should be avoided is that a certain number of insulating particles, namely RBCs, in the droplet splits between the measurement and reference chips not to lower the differential signal. To this aim the choice was to put magnetic concentrators only under the measurement electrodes in such a way to guide iRBCs, which are paramagnetic and electrically isolating, only on top of those, leaving the reference one unchanged.
In brief, magnetic concentrators are pillars of nickel embedded inside the silicon wafer, acting on the magnetic flux lines as depicted in Figure 2.1 (more on this in Chapter 3).
As non idealities are taken into account the first thing to notice is that it is very hard to fabricate two sets of perfectly equal electrodes, thus a current unbalance will be always present even without any hemozoin signal. This phenomenon can be negligible by fabricating the aforementioned electrodes on the same substrate with the same process. In other words, as it will be discussed more in depth further, the useful signal will be represented by the variations of a bigger one arising from the resistance mismatch, which can range from 1% to 10%. In addition to that, it must be said that those differential current variations can be as low as 30nA, and it represents this project's current order of magnitude. This limit is close to electronic instrumentation's one, which is around 5 to 10 nA, but not given by that. Instead,

when setting up the experiment magnets and chip are far apart. As magnets are slowly approached to the chip a minimum signal of 30nA arises, giving in turn the aforementioned resolution limit (more on this in Chapter 4). It is still not completely clear how this signal comes up, but probably the reason is that magnets are strong enough to produce a micro bending in the chip, thus deforming it and producing a very tiny current.
Another non-ideality that has to be taken into account is the drift caused by evaporation, in fact a single droplet of blood is subject to evaporation, therefore its ions concentration changes if water in the droplets evaporates as well. This could be avoided, or at least minimized, ensuring a good sealing between gasket and chip.
The choice to use exactly the same area for both measurement and reference electrodes could be in principle only area consuming and thus costly, but it should be taken into account that a precise study on how temperature drifts and other non-idealities affect the signal has not been performed, so to lower them as much as possible they are fabricated this way.
In future versions of this project a more careful study could be carried on thus inferring some proportionality constant between measurement electrode and reference one and therefore decreasing latter one dimensions being even more cost effective. Moreover, having both the chips of the same dimensions, all electrical parameters are approximately the same, so the electrical complexity is simplified not having scaled versions of the same parameters such as currents which should be then processed in different ways.

2.5 Design optimization

In this section the rationale on how to design electrodes will be briefly presented, justifying all the decisions taken. Note that the chip is designed to have two layers: the first one is inside its own silicon and it is made by magnetic concentrators, the second is the outer one which hosts the gold electrodes on top of a SiO_2 insulating layer dividing them.

2.5.1 Magnetic layer

Magnetic field is of fundamental importance in this project and it is used both at macroscopic level and at microscopic one. The former employs a set of two magnets (0.9 Tesla each) to create a magnetic field *gradient* that can attract particles in the long range of a drop thickness, the latter instead is constituted by a matrix of nickel micropillars to concentrate magnetic flux lines for a distance of about 50μm.

2.5.2 Microstructures

Once the particles are attracted, they need to be concentrated by microstructures to be effectively measured. The optimal pattern and shape for microstructures was previously found by means of FEM simulations in an array of nickel cylinders[23].
This pattern is subject to an important trade-off: to increase attraction cylinders must be closer and closer, thus having an higher density of elements is important, but for impedance variation they should be as few as possible to have a significant variation.
In addition to that, pillars physical parameters present a trade-off as well: for the sake of attraction they should exhibit a large height-diameter ratio, but this leads to fabrication issues.

For instance in the usage of reactive ion etching (RIE) technique, and the consequent fill by means of electroplating, high aspect ratios are not advisable since this could lead to heavy uniformities.

, so, for these reasons their height is fixed at 20μm.
Various centre-to-centre spacing configurations have been tested varying also pillar's diameter, the most significant ones were with diameters of 20μm or 40μm and the spacing was 80μm or 160μm, thus obtaining 4 different combinations, also called "geometries".
With respect to the previous thesis work a substantial improvement on timing was performed thanks to the addition of a vibrational motor helping mobility of iRBCs, thus worst case capture time went from 20 minutes to 5 now. This is very helpful also to mitigate temperature drift effect being it a slow change.

2.5.3 Sensor geometry

The main application of interdigitated electrodes in biochemistry field is to sense diffused corpuscles. As in this device only few concentrated particles are supposed to be on the magnetic concentrators, a step in which the detection electrodes were optimized has been carried out in order to weigh only the points where the cells are actually located, leading to better optimization. To connect the electrodes with a single photolithographic step, a planar structure is needed, with wirings 40μm wide, spaced 160μm. Moreover it should be noted that particles are attracted to the edges of the magnetic concentrators, so the geometry must take into account this fact. For this reason a circular electrode has been designed as shown in Figure 2.10.

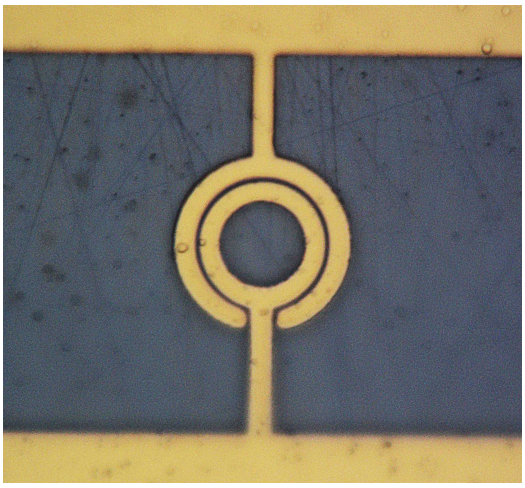

Figure 2.10: Particular of an interdigitated circular electrode

2.5.4 Wirings

Width and spacing of the wirings affect mainly three parameters:

- Series resistance of the wirings
- Parallel resistance of the wirings through the solution
- Capacitance through the solution

Wirings must be as spaced as possible and slim to decrease the effect of the last two parameters. However, this is not possible because the series resistance of the wirings would be higher than the resistance of the solution between the two electrodes. Ohm's second law is still valid even if gold is deposited as thin 100nm layer[27], so it is:

$$R_{wir} = \frac{\rho_{Au} \cdot L}{t \cdot W} \tag{2.23}$$

Where:

- ρ_{Au} is gold bulk resistivity
- L is wirings length
- t is their thickness
- W is the width

It is clear that ρ_{Au} is fixed being a physical parameter, t is a process parameter, thus it is fixed as well, L is geometrically fixed by the device length. The only degree of freedom left is represented by W. To have R_{wir} sufficiently low W was set to 40μm. In Figure 2.11 the main device components are shown.

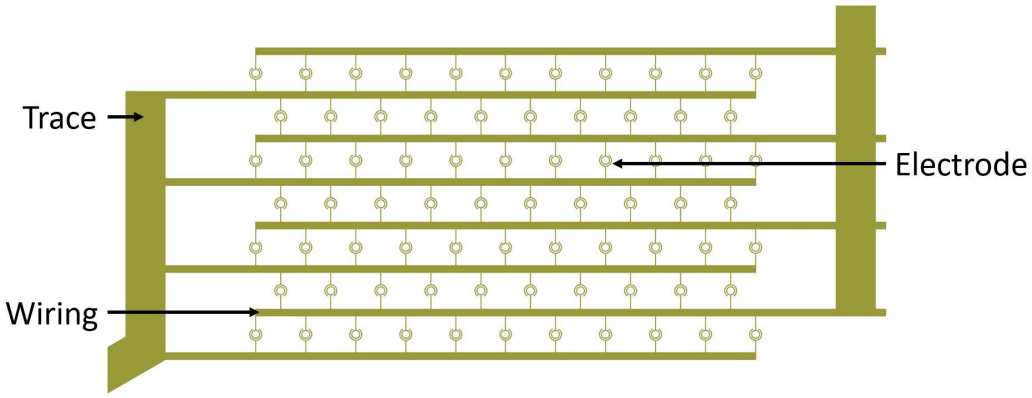

Figure 2.11: Schematic design layout of the active area of the device

2.5.5 Insulating layer

To further decrease the wiring contributions through the solution, a thick insulating SU-8 photoresist layer is required to be laid on top of the entire surface of the device, leaving uncovered only the active areas over the magnetic concentrators and electrodes. Doing so, the parallel resistance becomes huge, negligible with respect to the solution. 5μm is the minimum SU-8 photoresist thickness which has been previously shown to be more than enough.

Chapter 3

Device Fabrication

This chapter presents the method followed for the microfabrication of the device. It starts with the design of the electrodes using AutoCAD and goes on with the actual manufacturing thanks to cleanroom facility at PoliFAB [28].
The presented work flow results from the refinement and optimization of previous thesis works [23, 29]. The main steps are:

- Electrodes design
- Photolithography or optical lithography
- Reactive ion etching (RIE) to create cavities for the pillars
- Electron beam evaporation to deposit a thin nickel layer
- Electroplating to grow the aforementioned pillars
- SiO_2 deposition through chemical vapour deposition (CVD)
- Sputtering to deposit a uniform gold layer
- Lift off to remove gold from every part of the area which should not be electrode
- SU8 coating to protect the produced chip

Now a deeper step-by-step analysis will be performed.
The actual fabrication of the device is composed by two main parts being this a multi-layer device. The first part aims to fabricate magnetic concentrators, the second one is devoted to the fabrication of the electrodes. Every step must be accomplished with the so-called planar process, widely used in the

semiconductor industry, whose key concept is to view a device as a layered two-dimensional plane, each layer representing a step.

3.1 Magnetic layer

3.1.1 Photolitography

Photolithography, also called optical lithography, is a microfabrication process aimed to pattern a substrate. It uses UV light to exploit solubility change in a photoresist (PR), which is a light-sensitive polymer. Every step of photolithography is analyzed in more detail in a specific sub-section.
To start, once it has been decided to produce a new group of chips, the first thing to do is to get a new silicon wafer.
Every wafer is polished on one side: the one that will be used in every step of the process. In principle they should be perfectly clean, but to be more sure a preliminary cleaning with acetone, isopropyl alcohol rinsing and nitrogen drying.
Every process described below up to the development has been made in a so called yellow room which is a specific part of the cleanroom illuminated only with yellow light so that UV part of the spectrum is cut out and every photoresist is protected through the whole process.

3.1.2 Spin Coating

First step is to put a layer of AZ40XT positive photoresist on top of the clean wafer. To have the most possible uniformity across the whole surface spin coating technique is used. The machine that takes care of the spinning process is the "Karl Süss RC8" spin coater shown in Figure 3.1.
Among other parameters the most important ones are:

- Revolutions per minute: 2750 rpm
- Time duration: 45 seconds
- Acceleration: 500 rpm/s

It must be also noted that the aforementioned parameters are the results of multiple iterations to properly calibrate the so called "recipe", which is the complete parameters list. To start the calibration photoresist's datasheet was very useful.
A schematic view of the steps described here is available in Figure 3.2.

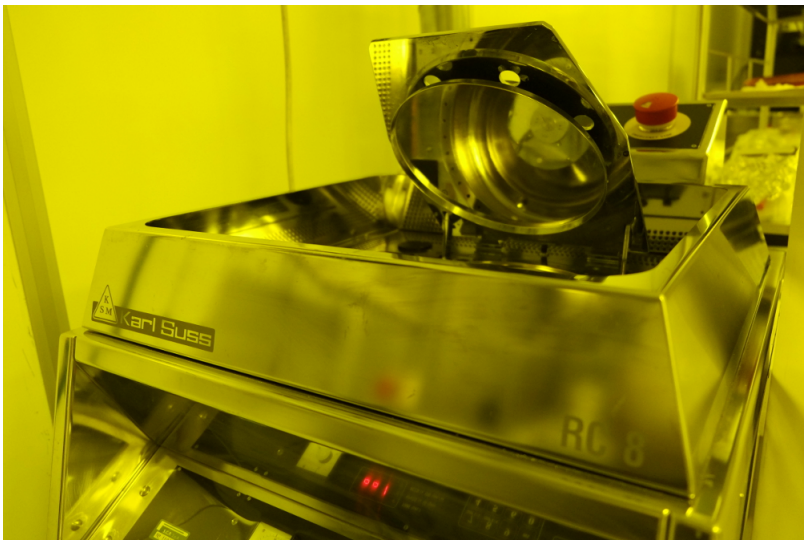

Figure 3.1: Karl Süss RC8 spin coater, note yellow ambient light

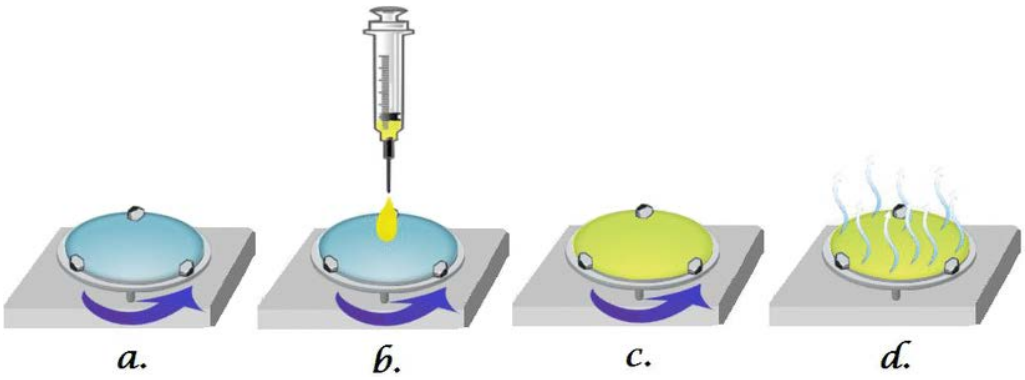

Figure 3.2: a. Placement of the sample on the spincoater b. Deployment of the liquid photoresist or primer c. Spinning phase, the liquid reaches the desired thickness d. Evaporation of the solvent, facilitated by employing a hotplate

Once the spin is complete a 20μm photoresist layer has been correctly deposit. Now a preliminary bake, named "soft bake", is performed with a 7 minutes long process starting at a low 50°C temperature going slowly up to 120°C. This gradient is of fundamental importance to let photoresist's solvent evaporate gradually. Its absence would lead to an almost instant solvent evaporation in the lower part of the resist. As AZ40XT is a viscous photoresist small bubbles form on the lower layers, which appear as a foam. Soft bake aims to allow a complete evaporation of the solvent containing the

polymer and to improve resist adhesion on the sample surface. Also, polishing the back side of the wafer is a very useful expedient, as resist leftovers may lead to an angle offset in the exposure procedure in the MLA100.
Once this bake is complete the wafer is ready for the next step.

3.1.3 Maskless Aligner

Patterns on the sample can be created using a photomask or a maskless system, in this thesis work the latter has been used thanks to the "Heidelberg MLA100" shown in Figure 3.3: a maskless aligner which uses a laser diode to draw the aforementioned AutoCAD patterns on the wafer. It features a

Figure 3.3: Heidelberg MLA100 maskless aligner

maximum power of 10W and a wavelength λ of 365nm.
The most significant advantage of using a maskless system is the possibility to make changes in AutoCAD patterns without any additional cost related to the generation of a new photomask. The downside instead is represented by the slowness of the process when large areas need to be exposed.
Now the most important parameter is the exposure energy density, also known as *dose*, set to 1250 $\frac{mJ}{cm^2}$ for patterning AZ40X.
There are two different typologies of photoresists: negative and positive ones with the conceptual difference summarized in Figure 3.4.
In negative resists the area exposed is made less soluble, in positive resists instead it is made more soluble to its proper solvent, called "developer", thus allowing its removal more easily in the following developing stage. In other words for the latter case the UV light provides the energy required to break the polymeric chains, letting the solubility of the photoresist to grow in the

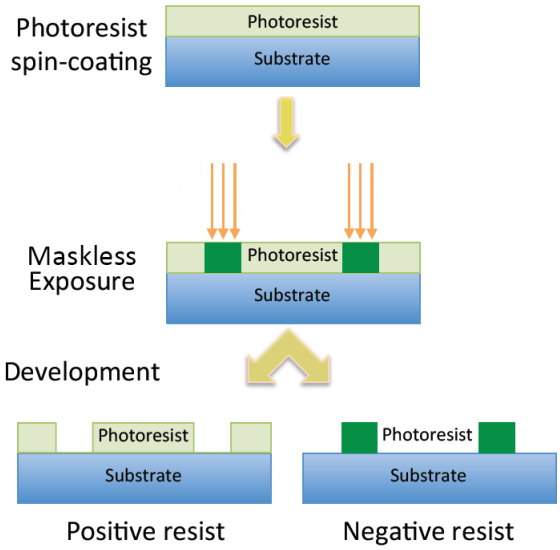

Figure 3.4: Conceptual difference between positive and negative photoresists

exposed area, so that its removal during the development step is easier. Note that the AZ40XT is a positive photoresist, this means that the exposed area coincides with the one that will be removed. Furthermore with this particular photoresist a post exposure bake is mandatory and it is carried on at 105°C for 100 s to complete the photoreaction and make the resist easy to develop. As for the previous bake this has to be performed gradually to avoid high temperature steps.

3.1.4 Development

Once all the exposure processes are completed an appropriate resting time must be waited to safeguard the sample from cracking due to the high temperature difference with respect to the solvent. The soluble part of the resist should be removed, thus letting the pattern take place. To this purpose an appropriate solvent, named *developer*, must be used depending on which photoresist has been previously adopted. In our case it was the AZ40XT, so the recommended developer is the AZ726MIF.
Developing stage is highly critical because once the resist has been removed there is no way to recover an error unless doing it all over again: in this case an overdevelopment was done. To be on the safe side a conservative development, of around 1 minute is performed then the sample is carefully washed in water. At this point it is inspected with the help of a microscope

and, in case of an underdevelopment, a secondary very short development is performed again until the result is considered satisfactory.

3.1.5 Reactive Ion Etching

At this point the sample has a photoresist mask on top of itself with the desired pattern. Next step aims to fix it in place by means of the etching removal of the material on areas where the PR mask leaves the silicon uncovered.
A very detailed explanation of how RIE works is out of the scope of this thesis work and therefore will not be carried on: only the most relevant aspects of it will be presented.
Reactive ion etching, also known as RIE, is a dry etching technique which uses chemically reactive plasma generated by an electromagnetic plasma in vacuum. The most significant advantage of a dry etching with respect to a wet one is represented by its directionality: this is very important in our application since we need to dig thousands of 20μm holes inside a silicon wafer (or 40μm, depending on the chosen geometry). This directionality is the result of how the etching process of a RIE works. It uses a chemically reactive plasma to etch away materials, in this case wafer's silicon. This plasma gets generated under vacuum thanks to a radio frequency (RF) electromagnetic field, usually at 13.56 MHz with some hundred W of power. The actual etching happens when massive reactive ions impact wafer's surface, thus reacting with it. Combining both physical and chemical etching this results in a hybrid technique which has very good directionality properties.
Particular attention must be paid to the fact that the digging process is not unique: a cycle of 180/185 sub-processes is performed alternating an etching cycle with a passivation one to make sure that the directionality is preserved. In the passivation cycle, C_4F_8 plasma in the chamber deposits a uniform protective polymer on all surface; in the etch cycle, the accelerated ions directionally remove the passivation layer from the base of the trenches, but not from the side walls, finally a SF_6 plasma in the chamber attacks the exposed silicon areas at the base of the trenches digging a bit more in depth. The passivation, etch and attack cycles are iterated until desired etch depth is achieved as shown in Figure 3.5.
Once the etching process is complete an electron beam evaporation is performed depositing a 30nm thin layer of nickel that covers up all the sample. This layer, named "seed layer", is employed to ease the successive electroplating step.
Once this has been done, resist is no more needed, thus it has been washed out carefully in acetone with the help of ultrasounds.

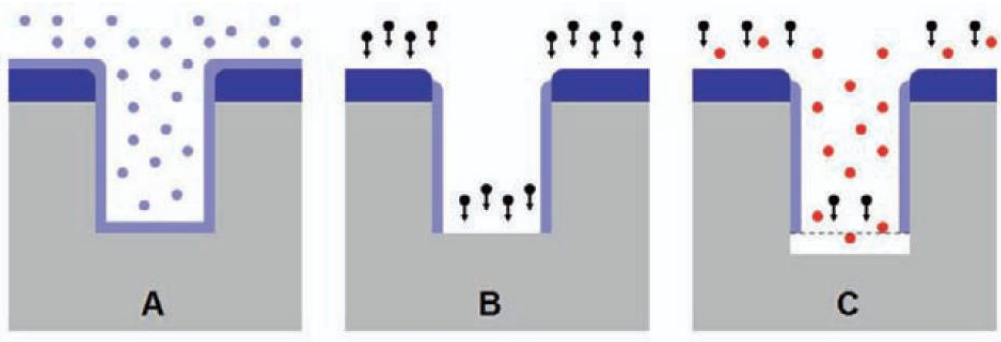

Figure 3.5: A. Passivation B. Passivation removal C. Etching

3.1.6 Electroplating

Electrochemical deposition, also known as *electroplating* is a technology which lets us deposit a metallic coating on a substrate. For a thickness lower than 1μm there many techniques, one of which is evaporation. To deposit 20 μm of nickel this was not a viable solution, hence electroplating was the only way to proceed. It has some disadvantages like the lack of a complete reproducibility, a lower degree of uniformity of the layer, as well as a not very controllable process. Nevertheless, allowing the deposition of such a thick layer of nickel, this was the selected procedure. The electrolytic cell shown in Figure 3.6 highlights its main components which are:

- 2 electrodes, anode and cathode
- A power supply to allow current flow
- The electrolyte solution

Whenever a positive electrical voltage is applied to the system negative ions migrate to the positive electrode (anode) and positive ions do the opposite (to the cathode). At the solution-cathode interface, being nickel ions positively charged (Ni^{++}),they get reduced to nickel atoms thus depositing in previously etched holes and forming nickel pillars as shown in Figure 3.7.
Standard electroplating uses direct currents, but in *pulse platings*, alternate currents are involved. The power supply applies short current pulses, usually in the range of 50 - 1 000 Hz, which favour the formation of grain nuclei and increases the total number of grains per unit area, thus leading to better overall properties [30]. For this project a period of 15ms has been used and, in addition to that, this square wave has a duty cycle of around 80%, where for this part of the period a positive current is applied. In this time

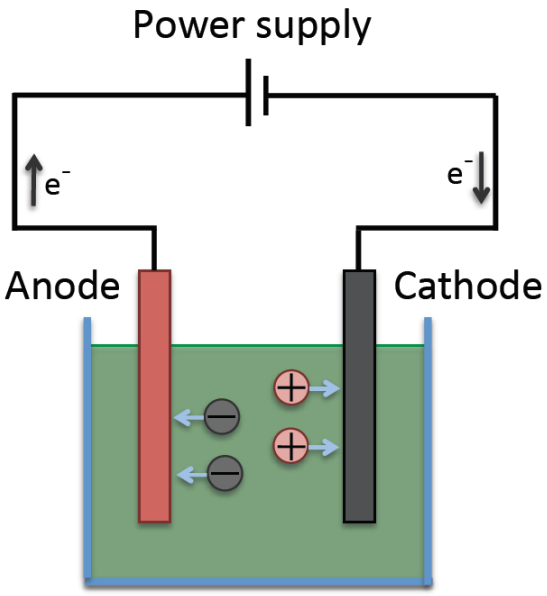

Figure 3.6: Conceptual scheme of an electrolytic cell

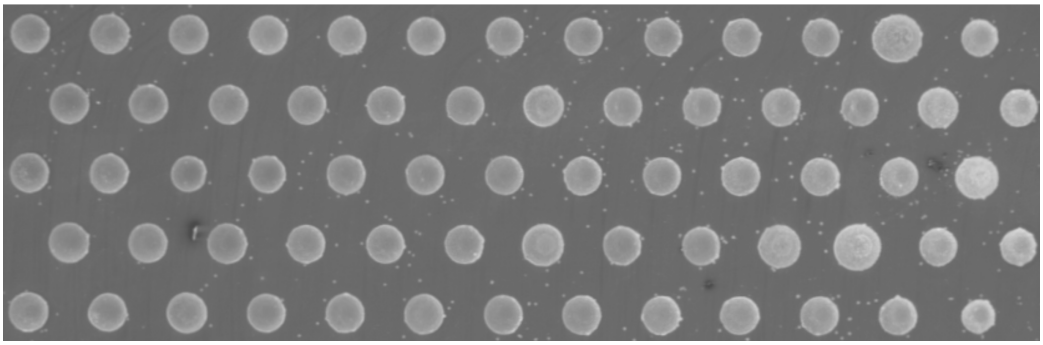

Figure 3.7: SEM detail of nickel pillars seen from above

electroplating deposits on hole's bottom, but also on its outer edges, thus risking to close it. In order to contrast this behaviour, in the remaining 20% of the period a negative current is applied which is not long enough to detach nickel from the bottom, but prevents the hole from closing by eroding the one deposited on the edge. The liquid in which the sample is positioned, at a temperature of 52°C, is called "nickel sulfamate" ($Ni(SO_3NH_2)_2$), and the current density is $14\frac{mA}{cm^2}$.
In principle nickel should progressively fill up the cylindrical holes like shown in Figure 3.8 and electroplating time duration should be tuned such that the process stops when nickel barely fills the hole.

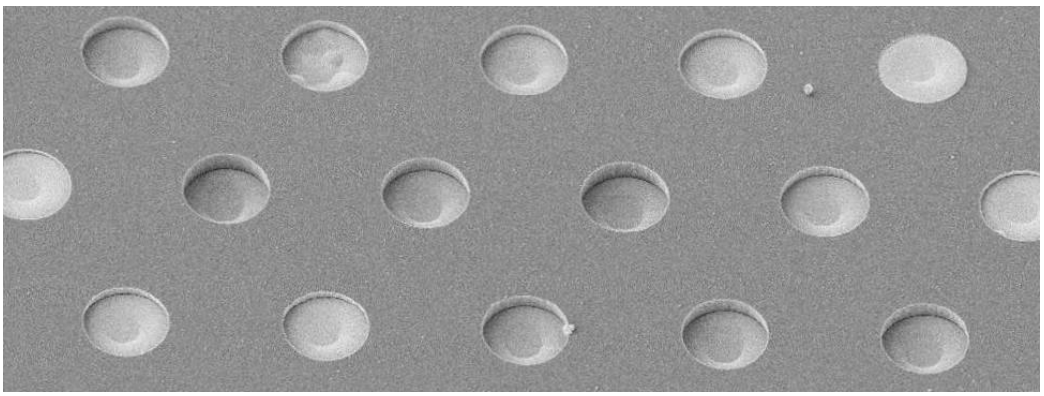

Figure 3.8: SEM image of an incomplete filling of the magnetic pattern

In practice this is not possible and to obtain a complete fill, an excess of nickel has to be deposited. This leads to what is shown in Figure 3.9, which is a 15μm nickel hill. In order to eliminate this overfill an additional refinement step must be performed.

3.1.7 Refinement and covering

Electroplating process ends up in big disuniformities across the sample, being some holes barely filled and others overfilled as shown in Figure 3.9.
At this point, the only thing doable to bring back a sufficient degree of uniformity, is lapping away the overfilling nickel. Due to poor reproducibility of hand made processes, a lapping machine by Seikoh Giken, shown in Figure 3.10, has been used with sandpaper sheets of 3μm grain for 5 minutes, at first without load on top.
After this preliminary step a complete and careful wash of the sample is performed and it is inspected under a microscope. If necessary the above

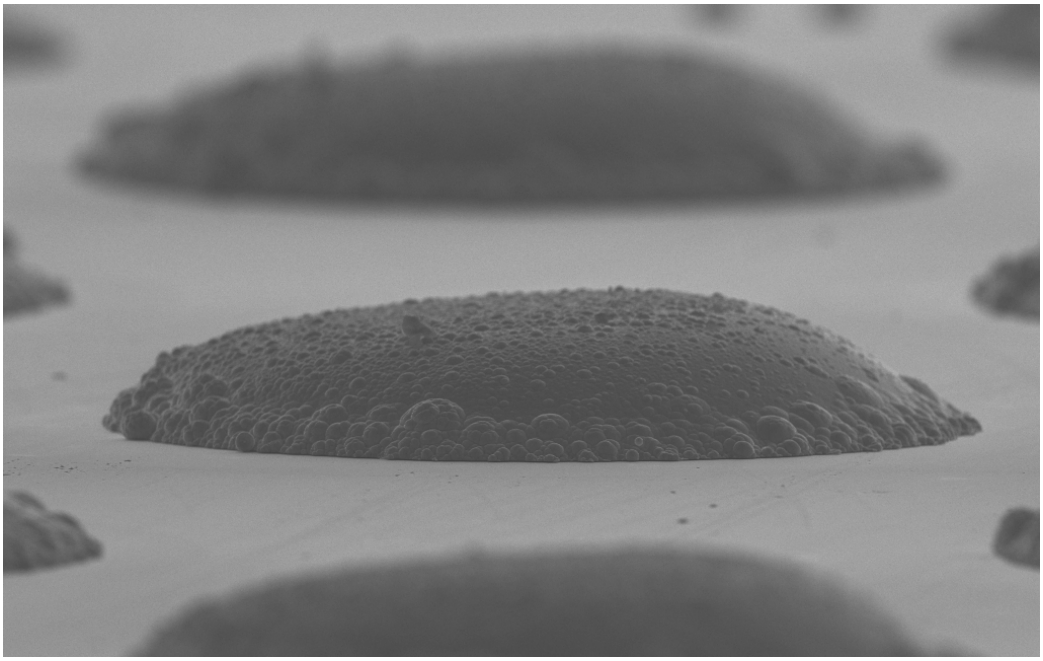

Figure 3.9: SEM image of the overfill

Figure 3.10: Seikoh Giken SFP-550 polishing machine

mentioned step is repeated until a complete lapping takes place. The last step consists of a soft polishing paper of 1μm grain with load gently placed on top of the machine not to produce any residue that could scratch heavily the sample itself. Once this step is complete it is time to cover the whole surface in a SiO_2 coating once again in the electron beam evaporator with a few tens of nm and after that with CVD for a couple of μm. Up to now the goal of having the magnetic concentrators under a clean surface was achieved. On top of this the electrodes will be placed.

3.2 Electric layer

At this point the wafer contains a group of patterns under a SiO_2 insulating layer. Now it must be prepared to host the electrodes on top of it. To this aim the former steps described in this chapter must be repeated with slights adjustments up to the development. Pay attention that now it is of fundamental importance to be able to pattern the electrodes layout perfectly aligned on top of the concentrators below.
Even if conceptually there is not much difference a brief explanation of the adjustments taken will be presented especially for what concerns photolithography.
In Figure 3.11 the target design made with the help of AutoCAD is shown. As can be seen the device will feature 8 sensitive areas divided in 4 groups of 2 areas each, thus resulting in a 4-channel device.

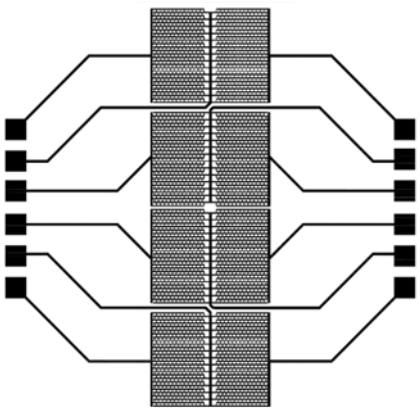

Figure 3.11: Target design made in AutoCAD

3.2.1 Spin Coating

To enhance resist grip to the substrate a layer of adhesion promoter Ti-Prime Primer by MicroChemicals has been deposited by means of spin coating. The machine used is again "Karl Süss RC8" spin coater shown in Figure 3.1. This time, however, the program was set to 4500 RPM for 45s, then it has been heated up on a Sawatec Hotplate HP401 being baked at 120°C for 120s.
Next step involves the deposition of MicroChem AZ5214E negative photoresist, employing once again the Spin Coater at 6000 RPM for 60 s, in order to have a 1.6-μm-thick layer and then facilitate the solvent evaporation by means of a 110°C bake for 100 s.
Pay attention to the fact that AZ5214E is a *negative* photoresist, thus once the exposure is performed the part easily removable with development is the *non*-exposed one as shown earlier in Figure 3.4.

3.2.2 Maskless aligner and flood exposure

Now that the resist has been uniformly spread on top of the sample it is time to expose it by means of the previously used "Heidelberg MLA100" shown also in Figure 3.3. The dose used was $32\frac{mJ}{cm^2}$. Then a reversal bake, a critical step, must be performed with 115°C for 90 s to supply the resist the needed energy to cross link.
Then, a 90 s flood exposure is needed to weaken the non-cross-linked resist, carried out at $5.1\frac{mW}{cm^2}$ in "Karl Süss Mask Aligner MA6/BA8" shown in Figure 3.12.

3.2.3 Development

For the AZ5214E the appropriate developer is once again the AZ726MIF. Development phase lasts approximately 30 seconds. As soon as it is developed the sample gets washed in deionized water to stop the spurious development carried on by AZ726MIF residues.

3.2.4 Sputtering

The most significant difference with respect to the process described before for the magnetic layer is that once the photoresist has been correctly exposed and developed the sample passes through a magnetron sputtering where in the end a 100nm thin layer of gold is deposited on top of a 30nm chromium one.

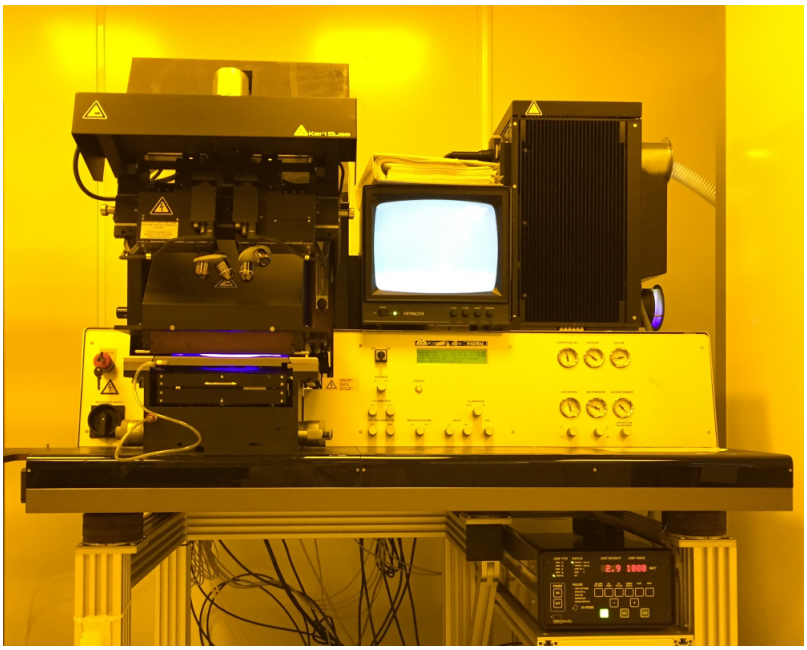

Figure 3.12: Heidelberg MLA100

The machine used is the "Magnetron Sputtering System Leybold LH Z400". Magnetron sputtering [31] is a physical vapour deposition technique, which allows a good film adhesion to the substrate, and a high control on the thickness, uniformity and composition of the deposited material. Its working principle is displayed in Figure 3.13.
First a gaseous plasma, usually of Argon gas, is create. Then, thanks to a voltage difference between anode and cathode, it accelerates the ions from this plasma into some source material, which is eroded by the arriving gas ions via energy transfer and is ejected in the form of neutral particles, either individual atoms, clusters of atoms or molecules. As these neutral particles are ejected, they will travel in a straight line unless they come into contact with something, namely other particles or a nearby surface. By just placing an object like a silicon wafer in the path of those particles it will be coated in a thin layer of the source material. In magnetron sputtering, there are, on the target's back, permanent magnets. Those are employed to confine the free electrons in a magnetic field directly above the target surface. In this way a couple of advantages are obtained. The first is represented by the free electrons, which are rejected by the negatively charged target, so they are prevented from bombarding the substrate, hence avoiding overheating and possible structural damage. The second, instead, is represented by the path followed by free electrons along magnetic field lines, which, being tortuous,

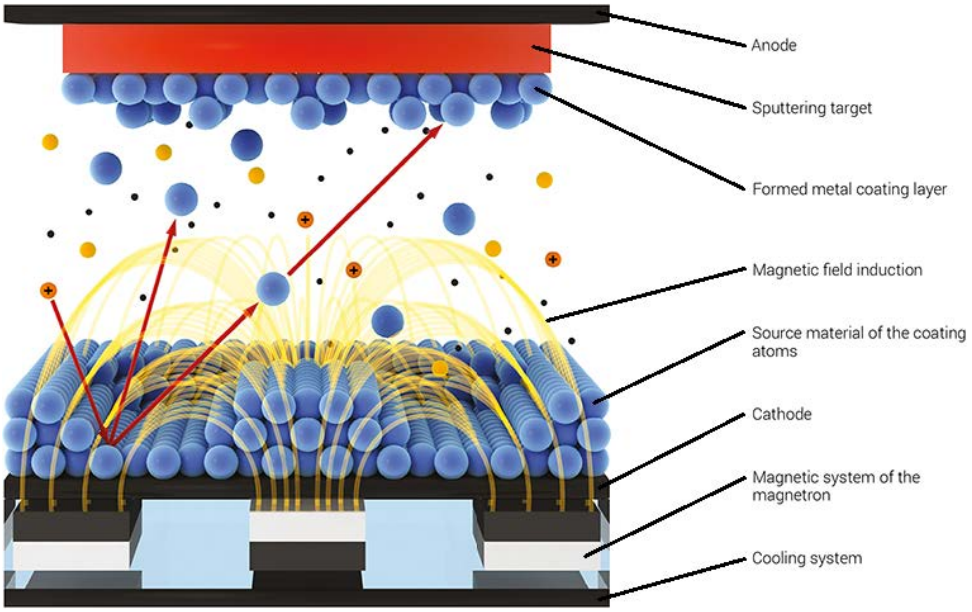

Figure 3.13: Working principle of a magnetron sputtering system

enhances greatly the probability of ionizing neutral Ar atoms. As a result, this increase in available ions significantly raises the rate of erosion of the target material, thus also its deposit rate onto the substrate.
To deposit gold it is first mandatory to make a 30nm-thin layer of chromium which will promote gold adhesion, then gold itself will be deposited in a 100nm-thin layer. At this point a layer of gold completely covers the sample and it is impossible to see the pattern.

3.2.5 Lift-off

Now the lift-off phase takes place and, by dissolving the photoresist which was exposed before the gold layer sputtering stage, the pattern comes out. Now the sample is carefully cleaned in acetone with ultrasounds once again and it gets prepared for the last stage of fabrication: a SU-8 protective coating. At this stage the pattern is already visible and in Figure 3.14 it is shown a particular of one area. For reference, compare it to the theoretical layout represented in Figure 2.11

3.2.6 Wirings coating

SU-8 from MicroChem is a negative photoresist. It is highly difficult to remove, therefore it is most suited for permanent applications like in this

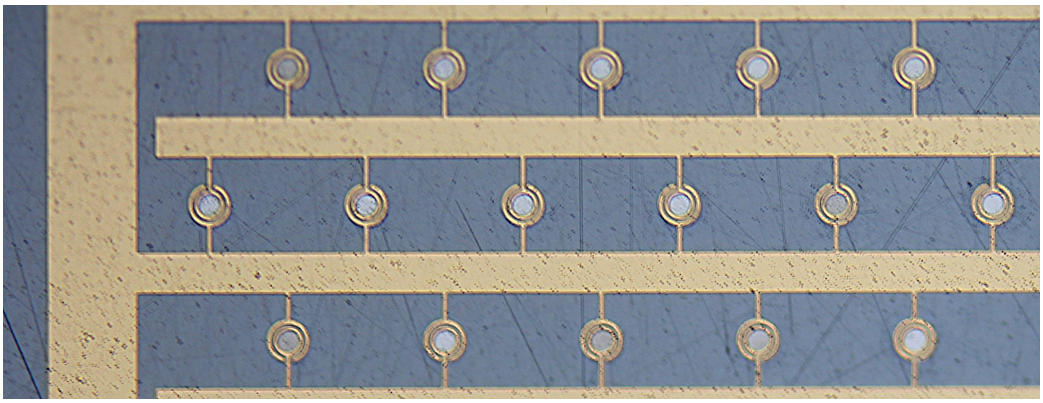

Figure 3.14: Actual result obtained after lift-off phase

case, where there is the need to leave uncovered only the part of the pattern with the electrodes, covering instead all the traces and wires of connection. The coating procedure is the same described above, a spin coating at 4000 RPM for 30 seconds is performed and then a 95°C bake for 3 minutes is carried on. For the exposure the MLA 100 is used once again with a dose of $700\frac{mJ}{cm^2}$ for a Si substrate. Particular attention must be paid to the fact that alignment is fundamental once again because SU-8 must cover only wirings and traces, leaving the electrodes naked.
A post exposure bake is performed at 95°C for 2 minutes. To correctly develop this resist, its specific "SU-8 Developer" and IPA are needed. The procedure can be carried out with naked eye. Su-8 Developer starts dissolving the resist and to stop its action IPA is used to wash it out. If some SU-8 residues are still present, in contact with IPA, they form a white foam on the sample, thus indicating its presence. Additional developing must be done until, when washing with IPA, no foam will be created. In the end a so called *hard bake* is performed. It should be at 10°C higher than the maximum operating temperature. To be on the safe side a 115°C one for 2 minutes has been chosen. Moreover, it has been noticed that said hard bake improves resist adhesion on the substrate as well as its resistance to thermal transients.
The obtained result is shown in Figure 3.15(a), whereas in Figure 3.15(b) a particular of a single electrode is displayed.

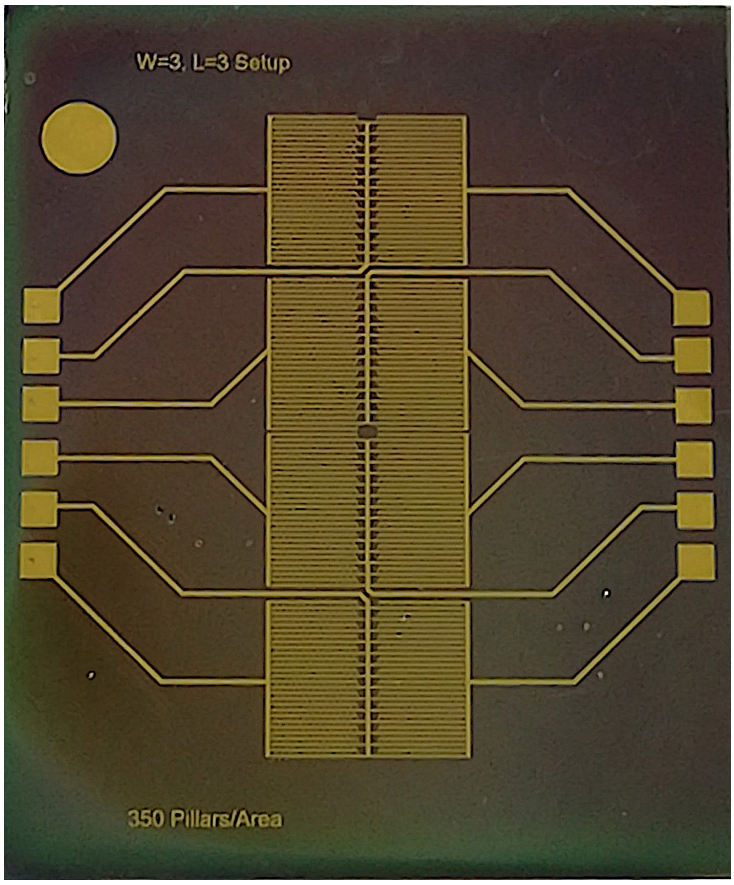

(a) Final result, plain view of the fabricated chip

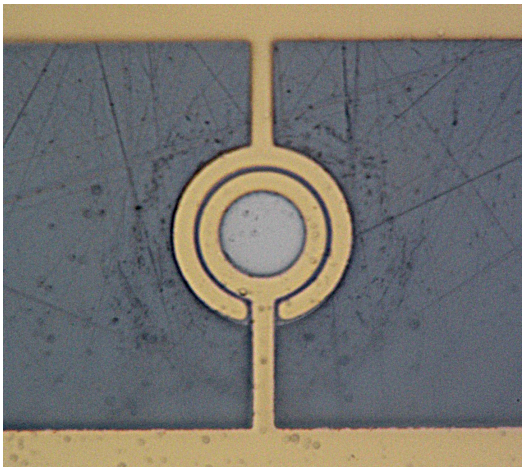

(b) Particular of a single electrode and its pillar underneath

Figure 3.15: Final results obtained on a real chip

Chapter 4

Validation and experimental results

This chapter is firstly devoted to recall the working principle of a Lock-In Amplifier (LIA). Following, an analysis of what concerns this project's requirements is performed, thus understanding and justifying the choices of the equipment used.
The designed setup will be then presented and the chapter will end showing as well some experiments done and their results.

4.1 LIA's working principle

Before starting the core of the chapter, a brief recall of what is the working principle of a Lock-in amplifier will be carried on.
The necessity of such a technique arises when the measurement of a narrow band signal must be performed in heavy noise, both white and 1/f. To overcome low frequency disturbances a modulation must be performed. Going on, to solve the problem of white noise a very narrow frequency filtering must be performed. A LIA is a continuous synchronous band-pass filter and it is used to extract a signal modulated on a known carrier frequency [32], where *modulated* means that the signal of interest is multiplied by a specific frequency sinusoid. It is also known as Phase-Sensitive Detector (PSD).
Basically, it is composed of two parts: the first one demodulates the signal through a multiplier, while the second part low-pass filters demodulator's output.
As shown in Figure 4.1, a sinusoidal wave excites the device under test (DUT), thus producing a signal, named $V_s(t)$ in the scheme, modulated

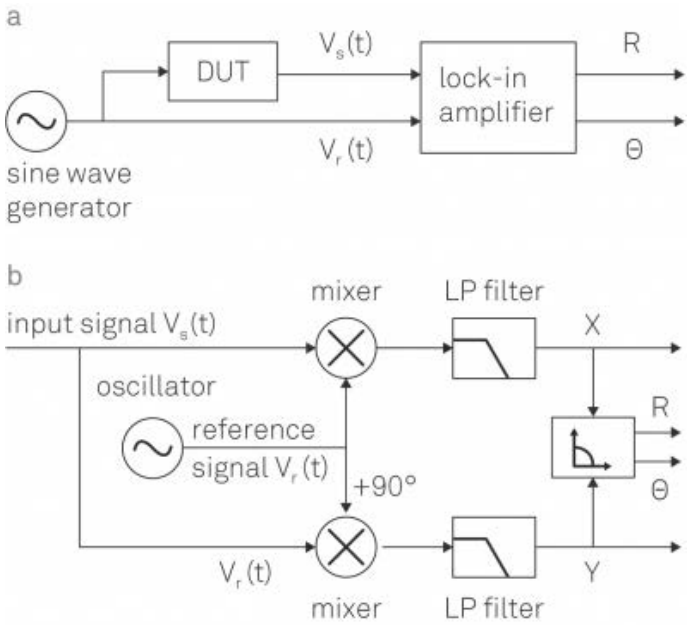

Figure 4.1: a. Working principle of a lock-in measurement b. Schematic of a dual-phase demodulation lock-in amplifier

around its frequency. In parallel to this branch a secondary one, which is the same of the first one, is brought to the LIA without passing through the DUT and acting as a reference, called $V_r(t)$, as can be seen in Figure 4.1a. The LIA, in this case, performs two simple mathematical operations to extract R, which is signal's absolute value, and Θ, that is its phase:

$$R = \sqrt{X^2 + Y^2} \tag{4.1}$$

$$\Theta = tg^{-1}\left(\frac{Y}{X}\right) \tag{4.2}$$

Dual-phase demodulation is the adopted technique to determine amplitude and phase of the signal of interest. In this technique the input signal is duplicated, then it is multiplied by a sine wave, while its copy by a cosine wave, obtaining thus two signals labelled as X and Y, representing respectively the real and imaginary part of the signal itself. As stated earlier, they are then low-pass filtered and by exploiting Equations (4.1), (4.2) R and Θ are inferred.

Keeping in mind what has been previously discussed about parasitic effects and the resistive plateau, one can realize how important this technique is for this project, since it allows the measurement to be performed at a frequency decided in advance, therefore finely tunable and optimizable. In this

project's case the importance lies in the fact that thanks to the modulation a bypass of the double layer capacitance can be achieved, therefore being sensitive only to the signal given by RBCs capture.

4.2 Experimental Setup Design

At this point, an investigation on which were the requested performance for the electronic system in order not to worsen sensors' resolution was done. This has been already assessed in former thesis work [23] and in the worst case it is:

$$\frac{\Delta R}{R} = 0.1\% \tag{4.3}$$

The total resistance is expected to be around 100Ω, so, by a simple multiplication, a resistance variation of about 100mΩ is inferred. To have some margins, an additional decade has been taken, addressing a design capable of detecting 10mΩ variations.
In order to achieve this performance the conceived experimental setup consists mainly of three parts: a Zurich Instruments HF2LI (Lock-in) with its HF2TA (transimpedance amplifier), and a stepper motor to control chip's positioning on the z axis to ensure a proper sealing between gasket and chip. A complete view of the system is shown in Figure 4.2. To present in further detail those parts a specific subsection has been dedicated.

4.2.1 Lock-in amplifier

To obtain this performance a Zurich Instruments HF2LI was used, as it covers with ease the frequency range of interest, even up to 50MHz with a demodulator output resolution of 64-bit, while its A/D conversion is performed with 14 bits at 210 MSPS and its D/A with 16 bits at the same speed[33].
The HF2LI has a couple of tasks to take care of in this initial experimental setup, which are:

- Stimulus
- Demodulation
- Low pass filtering

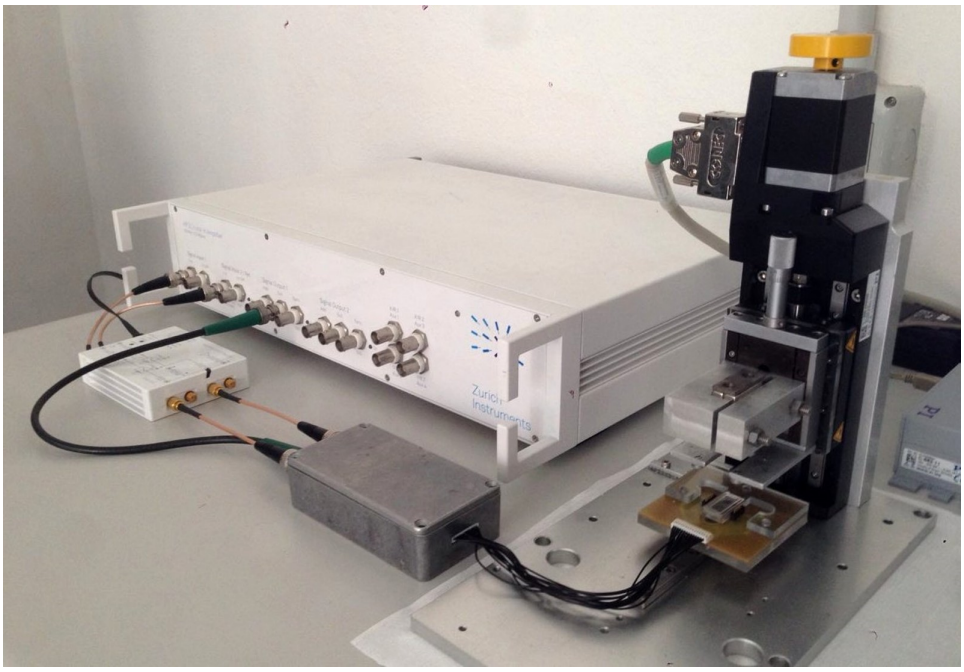

Figure 4.2: General view of the complete setup

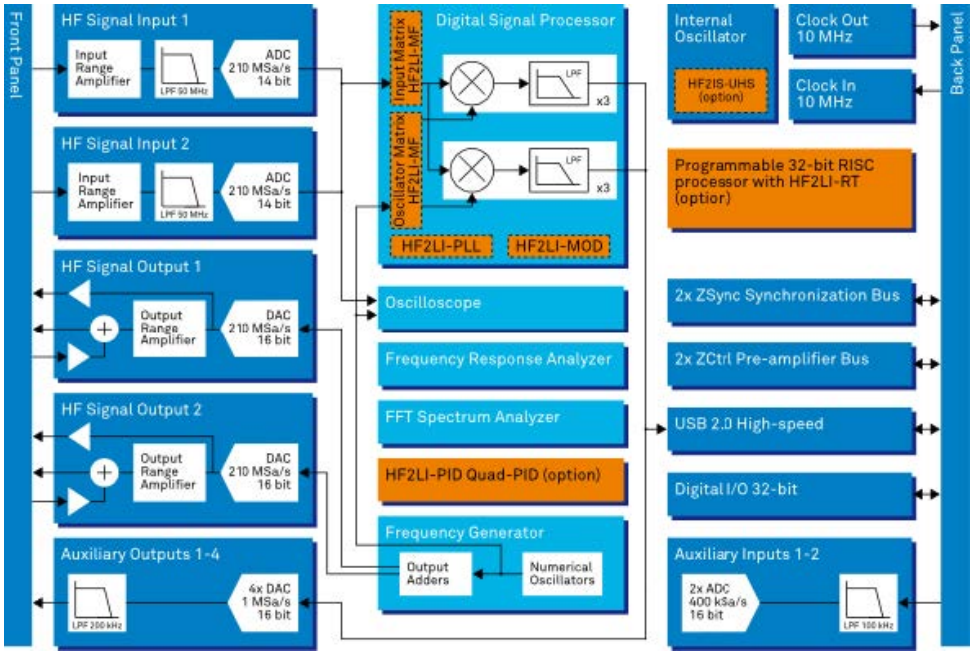

Figure 4.3: Block diagram of the Zurich Instruments HF2LI [33]

HF2LI's block diagram[33] is represented in Figure 4.3.
For what concerns the stimulus, it was decided to apply a continuous 100mV_{pk} amplitude sinusoid, at the frequency of 1MHz, to every sensor. Those choices were made to bypass the C_{dl}, as well as not to trigger red-ox reactions.
The stimulus must be precisely controlled, therefore the HF2LI is perfectly suited for the job.
Demodulation and low pass filtering are the core parts of HF2LI instrument, since it is embedded with a digital signal processor performing both of them with 64-bit precision.
Connected to a PC by high-speed USB, a graphical user interface program, named LabOne (formerly ZiControl), allows data acquisition at high rate. In addition to that, this application lets the user control every aspect of the instrument, for instance, individually for each channel, settings about the analog input and output amplitude, phase, frequency, samples per second, etc.
The device under test is of course the chip discussed in the previous chapters, keep in mind that it features 4 differential channels and 8 total areas. Figure 4.4 shows the electrical model of a single channel, which is made of two areas.

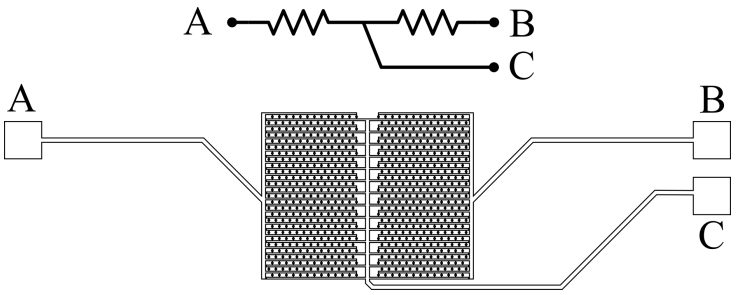

Figure 4.4: Equivalent model of a channel, consisting of two areas

In theory, there are two ways to carry on this type of measure. The first one stimulates the middle point of the two resistances and reads the obtained currents at the two ends. With this first method a subsequent stage to perform the difference between those currents is mandatory to get information about the resistance variation.
Another way embeds this difference in the way the chip is stimulated. Indeed, by applying a differential voltage at the two ends, namely a sinusoid and its anti-phase copy, the middle point should always stay at a fixed zero potential level, and current should flow perfectly in the series of the two. A visualization of what has been said is provided in Figure 4.5(a) for the single ended stimulus, and in Figure 4.5(b) for the differential one.

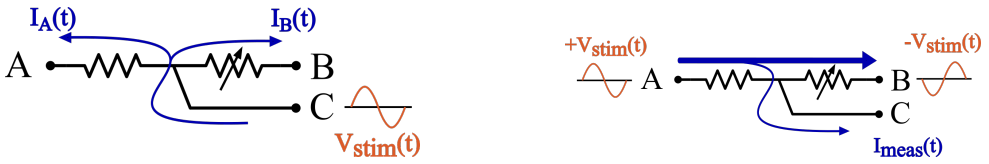

(a) Single ended stimulus

(b) Differential stimulus

Figure 4.5: Schematic view of the two possible way of driving this project's sensors

When one of the resistances changes, however, the value of that point moves in voltage. If now a suitably biased amplifier virtual ground is connected to that middle point, the excess current flows directly into it, thus making this type of measure natural for a current signal like that.
Moreover, this second way of measure enhances resolution properties, since the difference is inherently performed by the device. On the other hand, in the opposite case, the two currents should be separately read, converted into voltages and, to perform a difference, they have to be fed to a differential amplifier. Those two branches add their own noise and they are subject to disturbances which may not be seen as common mode, therefore could not be rejected later with the differential amplifier. For all these reasons it has been decided to use the stimulus shown in Figure 4.5(b) for the final version with the dedicated PCB. On the contrary, for this early stage experiments, the first middle point stimulation way was adopted, because the HF2LI in use could not provide two different sinusoids. In Figure 4.6 a schematic view of the first method, namely with a single stimulation, is displayed. Note that, as mentioned, there is only one voltage stimulus, but two current signals arise.

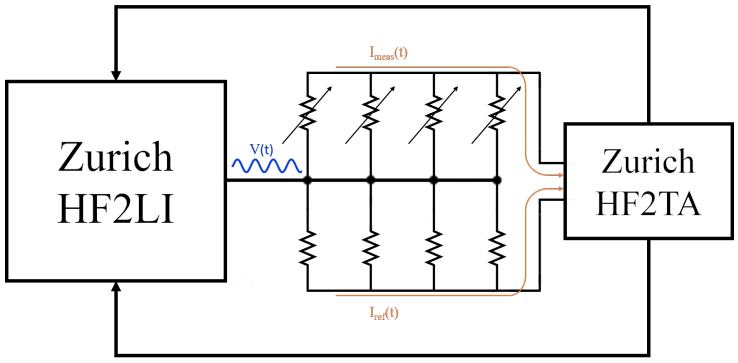

Figure 4.6: Schematic view of the conceived setup from the electrical point of view

4.2.2 Transimpedance amplifier

HF2TA is a Current Amplifier which, acting as a transimpedance amplifier (TIA), is used to convert the currents coming from the virtual grounds into suitable voltages, then read by the HF2LI itself. HF2TA has 2 independent channels so it is used for the aforementioned single-ended approach. It is important to note that, at this early stage, channel reading was not performed by multiplexing them, but only one is physically connected for the whole experiment duration, while the other three are left floating.
Moreover, it should be noted that, thanks to the JFET input stage, its equivalent input voltage noise power spectral density is very low, limited to $S_v = \left(5\frac{nV}{\sqrt{Hz}}\right)^2$. In addition to that, the input bias current is ultra-low, being only of 2pA, which must be compared to a minimum signal of 30nA, and a parasitic signal in the order of 10μA arising from the resistances mismatch. This way a precise measurement can be carried on, even if the signal amplitude is very small [34].
This was the experimental setup of a first set of tests in which hemozoin crystals (HCs) and treated bovine red blood cells (tRBCs) have been used.
At first, heavy problems due to the formation of air bubbles getting trapped at the interface between liquid and chip prevented any valid measurement to be obtained. Bubbles formed due to the lack of uniformity in the downward movement of the chip. Indeed, at first, said positioning was achieved with a setup made by three screws pressing the chip on the underlying gasket and manually tightening them. To solve this inconvenient a stepper motor, controllable through a PC interface was added (more on this in the following subsection). As showed in Figure 4.7(a), on top of a glass substrate, a 40μm polymeric gasket has been built to contain the drop of liquid. From above, the chip, down facing, is positioned. The height of 40μm was chosen because it has been previously demonstrated that this is the maximum range of attraction of the magnetic gradient.

4.2.3 Positioning motor

To solve the problem given by air bubbles getting stuck inside, there was the need of a much more accurate positioning. Targeting at the full contact with the liquid, as represented in Figure 4.7(b), a L406-20SD00L stepper motor provided by Physik Instrumente (PI) was employed. It features a 52mm total

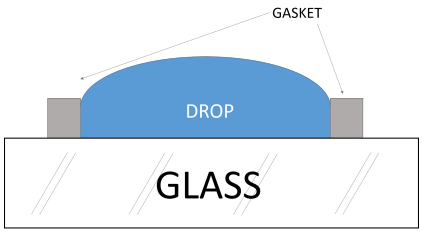

(a) Glass substrate with the drop on top, confined in the gasket

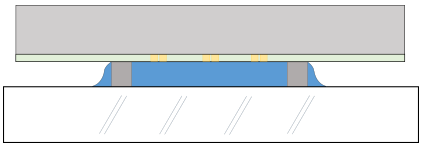

(b) Scheme of the chip facing downward getting in contact with the drop

Figure 4.7: Drop of liquid before and after chip contact

travel range, while its minimum step of only 200nm leads to a very accurate positioning.
The routine followed starts by loading the chip, down facing, into its slider. Next, the glass with its gasket on top is placed underneath, obtaining the setup in Figure 4.8(a). On its side, Figure 4.8(b) shows the setup once a blood drop has been landed inside the gasket.

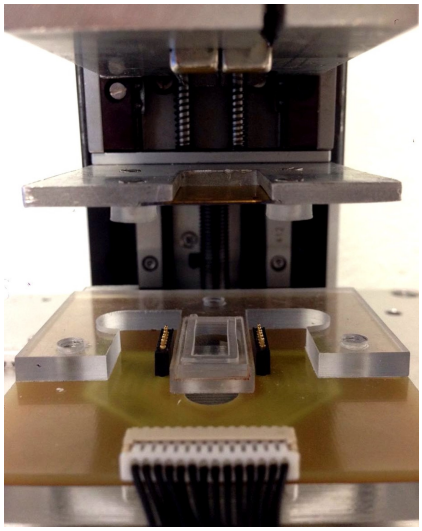

(a) Initial system, ready to host the blood drop

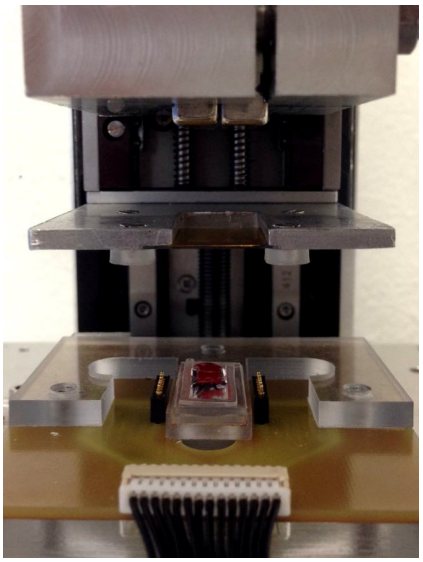

(b) Drop of blood inside the gasket before chip contact

Figure 4.8: First two experiments' steps

Now, very carefully, the motor pushes the chip in contact with gasket's surface, thus creating a sealed room as shown in Figure 4.9(a). Moreover, it is at this point that an electrical contact is made thanks to the set of spring

contacts on the gasket's side. Now, the electrical measurement is automatically started, but, since magnets are still far from the chip, no attraction is present. In other words the signal read in this third phase is the reference one, on which the comparison will be done. Indeed next phase is the correct positioning of magnets on the back of the chip, thus creating the magnetic environment discussed in Chapter 2. The obtained setup, while performing a measurement, is reported in Figure 4.9(b).

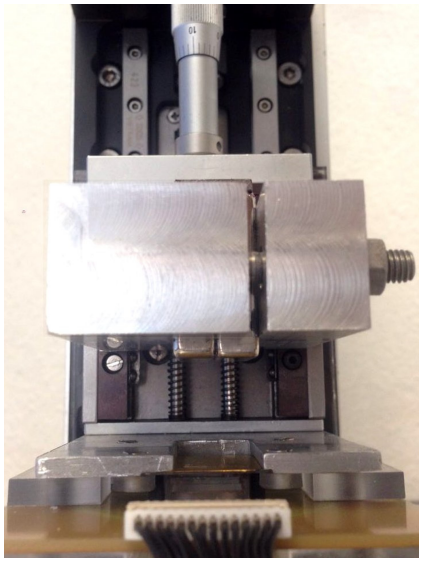

(a) Chip lay down phase and electrical contact

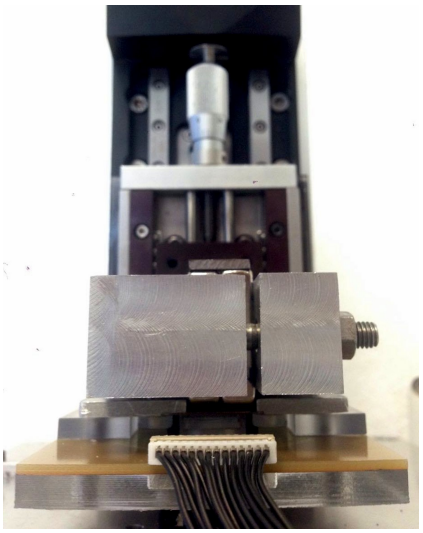

(b) Magnet lay down, attraction starts

Figure 4.9: Chip and magnets positioning

Picoblade by Molex[35], also shown in previous figures, is the selected connector thanks to its small footprint, abundance of lines and relatively high flexibility. Unfortunately, another problem that had to be faced was due to the connections between chip and HF2TA. Picoblade's lines were too close each other, so a non negligible crosstalk arose, hence the need of a further isolation provided by shielding each line individually in a separate moment. To take even more care, it was deemed useful to connect all the grounds and also the shieldings to be sure to have as few disturbances as possible.
Another countermeasure taken was the deposition of a think gold film on chip's back connected to ground as well.

4.3 Experimental Results

4.3.1 Tests on hemozoin crystals

A first set of experiments has been carried on with hemozoin crystals (HCs). The setup used was not featuring PI motor at first and manual adjustments were provided by the operator. In this initial setup there were two rails: one for the chip to place it in contact with the gasket, and a second one who hosted magnets, which were positioned manually with the help of a micromanipulator. Figure 4.10 shows the signal arising at the HF2TA input. Note that the current increases when magnets are removed and decreases accordingly when they are put back, since HCs are insulating. At first, a concentration of $15.63\frac{\mu g}{ml}$ was adopted and a resulting signal of 300nA showed. Moreover, this was a very clean signal, thus leaving much space for improvements, namely to address more sensitive measurements, thus sensing a smaller HCs concentration.

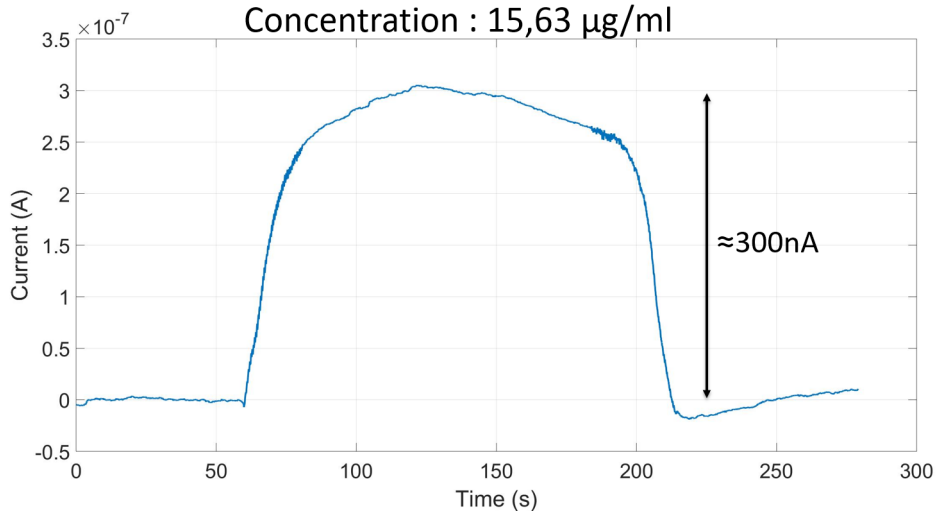

Figure 4.10: Removal and re-application of magnets causing signal to arise

Since the setup features very sophisticated equipment like the Zurich HF2LI it was addressed the resolution limit of the setup, which is around 20nA and it is given by the motion of magnets causing a signal to arise. To address a better resolution, the concentration of HCs was decreased to almost $3\frac{\mu g}{ml}$, giving a signal of nearly 65nA. Since it was again very clean, another test, featuring an even further decrease in HCs' concentration, was done. This time, with $1.25\frac{\mu g}{ml}$, a signal of 35nA was obtained, therefore almost getting to the aforementioned setup limit. In Figure 4.11 a comparison, which shows the signal getting more noisy as the HC decreased, is reported.

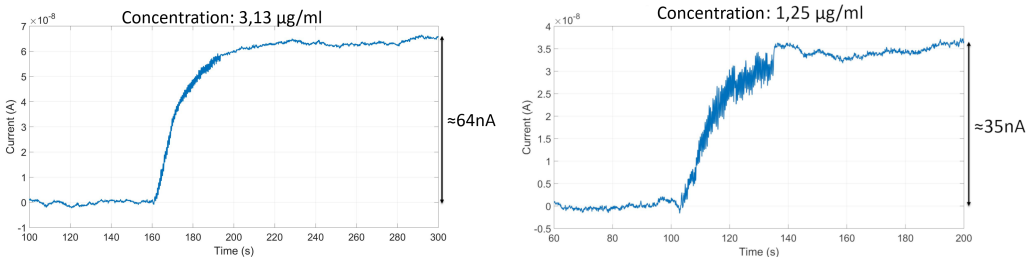

Figure 4.11: Comparison and resolution limits obtained

In addition to that, note the time axes, where the measurement can be considered concluded in nearly 5 minutes. For the sake of completeness Figure 4.12 shows the current obtained from each one of the two areas (namely measurement and reference one).

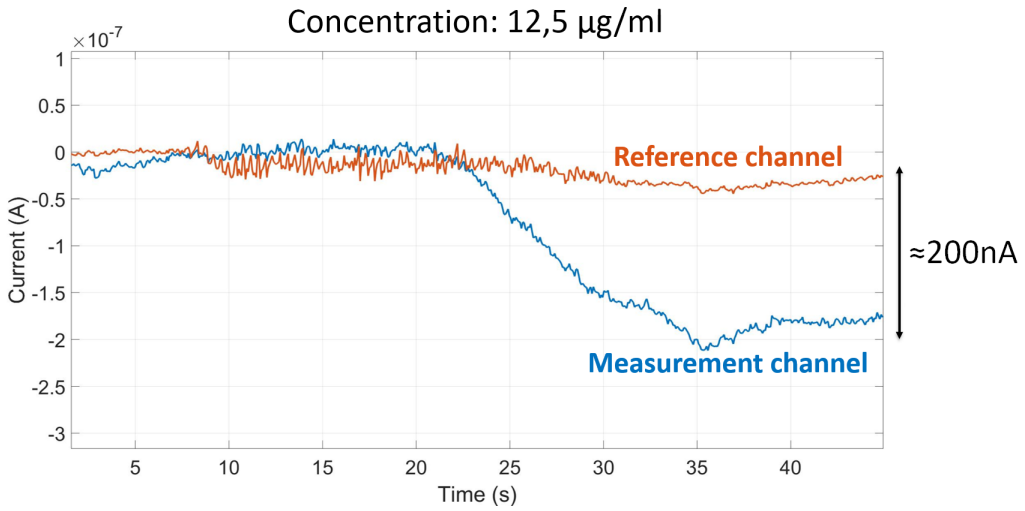

Figure 4.12: Comparison between reference and measurement channel current

This image clearly displays the correlation of the two currents when no magnetic gradient is applied and then how only the measurement part, which has magnetic concentrators underneath, changes its current value. Note also that, when applying magnetic gradient, the measurement current decreased with respect to reference one since HCs are isolating. To have a concrete view of what is happening Figure 4.13 is reported.
In this case, however, the geometry of operation is not inverted due to physical constrains given by the microscope. A pure sedimentation, nevertheless, lets understand clearly that micro-concentrators are really effective. Indeed,

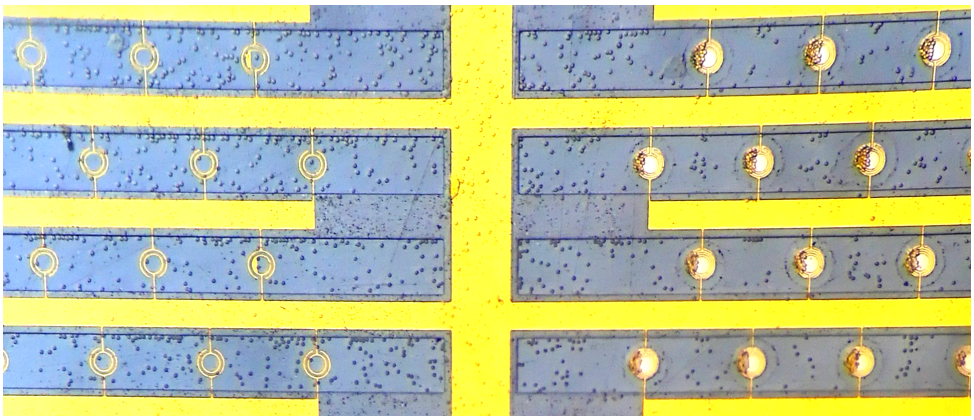

Figure 4.13: Comparison between reference and measurement channel sedimentation

on the right part, it can be easily seen that magnetic cells are attracted, while on the left part, without concentrators underneath, the disposition is random.
To further validate the obtained data and to put them in agreement with theoretical forecasts they were compared each other and the obtained results are shown in Figure 4.14. There, it is clearly visible how the theoretical line is passing through the obtained data points.

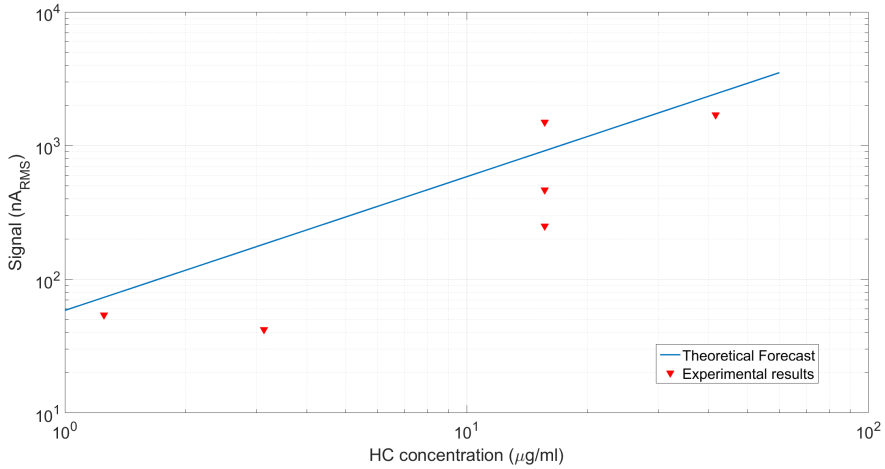

Figure 4.14: Current signal as a function of HC concentration, comparison between theoretical forecast and read data

To express those results in terms of equivalent parasitemia, which will be useful to compare HCs test with tRBCs ones, let's consider that that $1\mu g$

of HCs contains roughly 24 000 of them. Knowing that for every iRBC usually 20HCs are released, an average of $1200\frac{iRBCs}{\mu l}$ is inferred. Now, by also knowing that usually $5\,000\,000\ \frac{RBCs}{\mu l}$ are present, a useful conversion factor is obtained, thus understanding that $1\frac{\mu g}{ml}$ translates into an equivalent parasitemia of 0.024%. Thanks to that, it can be noted that the experiment with $1.25\frac{\mu g}{ml}$ is equivalent to one with the parasitemia of 0.03%.
For convenience, Table 4.1 sums up the results obtained in tests employing HCs.

Concentration $[\frac{\mu g}{ml}]$	Equivalent Parasitemia [%]	Current [nA]
15.63	0.375	300
12.5	0.3	200
3.13	0.075	64
1.25	0.03	35

Table 4.1: Differential current and equivalent parasitemia summing table for HC experiments

4.3.2 Test on red blood cells

Thanks to this results the project could make a big step forward aiming to tests with treated red blood cells (tRBCs), obtained by bovine blood. From the original sample five smaller ones were obtained, diluting every one of them differently, thus simulating various parasitemia levels, ranging from 0.005% to 5% and, in addition to that, a non treated sample was prepared as well. To have a yardstick, let's consider a patient who experienced his first fever attack, in his blood iRBCs can range from 0.1% to 1%. Moreover, this project achieved 0.005% on tRBCs, which is in line with the actual gold standard techniques. By comparing them with the theoretical dependence, as done in Figure 4.15, a clear correlation is highlighted.
For convenience, Table 4.2 summarizes the obtained differential current values, showing once again that the smallest signal's order of magnitude is in the tens of nA.
Another very important result is represented by system's selectivity. To prove this, another experiment employing the earlier mentioned non treated sample was used. The goal of this test is to show that no signal arises when only non treated RBCs (simulating healthy blood) are present in the solution. As

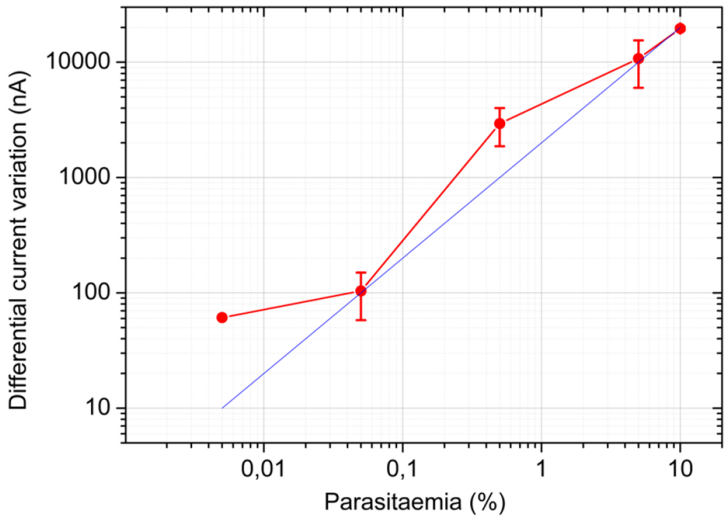

Figure 4.15: Comparison between theoretical dependence and real data on tRBC

Parasitemia	Current Variation
0.005%	61nA
0.05%	104nA
0.5%	2.9μA
5%	10.7μA

Table 4.2: Current and parasitemia sum up table

displayed in Figure 4.16, the signal originated from on treated RBCs, also called "aspecific", is near 15nA, which is given by setup limit, therefore, it is not significant and only due to noise.

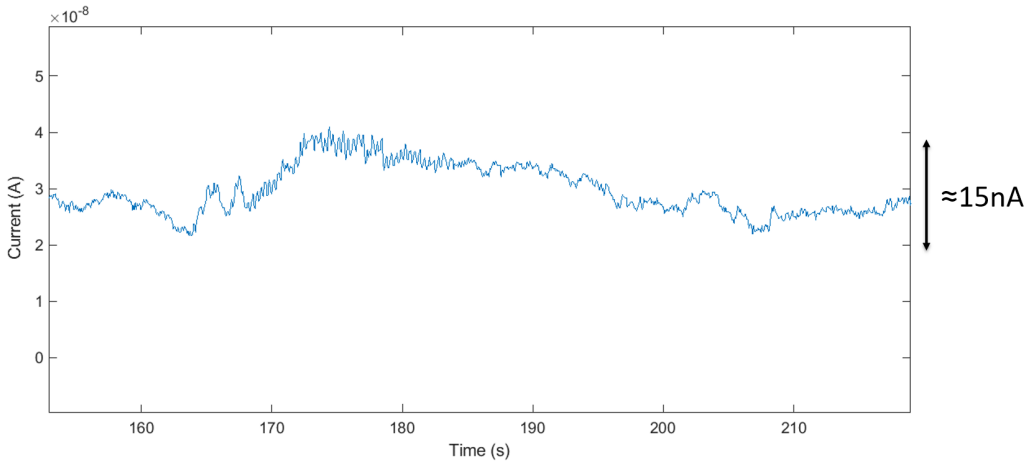

Figure 4.16: Current signal given by non treated RBCs, namely aspecific signal

In conclusion, a new set of experiments has been done with the same parasitemia values to further prove project's reliability. Table 4.3 sums up the different values measured. Once again, it is important to underline that the minimum signal obtained is setting electronics readout requirements, thus it was very important to make those measures in order to have a concrete example of the values in play.

Equivalent Parasitemia	Differential Current Variation	
	4/10/2018	19/10/2018
0.005%	61nA	60nA
0.05%	104nA	170nA
0.5%	2.9μA	2μA
5%	10.7μA	13μA

Table 4.3: Differential current variation summing table for the two sets of experiments

In addition to that, note how the limit of detection with HCs was equivalent to 0.03%, with respect to 0.005% achieved with RBCs. To justify this result, Equation (2.20) must be recalled, considering that RBCs are almost a factor of 10 bigger than HCs, thus directly translating in a sensitivity improvement

of the same factor. Moreover, it is useful to notice that to obtain a 60nA signal from HCs an equivalent parasitemia of 0.075% is required, while using tRBCs a 0.005% one is enough. Again, comparing a 0.3% equivalent parasitemia in HCs solution, giving 200nA current signal, with an almost equal 0.5% one with tRBCs shows a difference of a factor of 10 in the obtained current. Being this project aiming to be an early test it is mandatory to have good performance in an environment where iRBCs are present (even before the first fever). Those experiments undoubtedly prove that this method is not only fast, but also reliable and repeatable. On this basis a custom electronics, to readout and manage the signal, was developed.

Chapter 5

Readout Board Design

This chapter is devoted to present and analyse the board realized to stimulate the chip and to read the current containing the information about infection status of the blood drop. In the first part of this chapter a discussion on the set of possible implementations of this technique is presented. Once defined which one will be the chosen architecture a more detailed discussion will be carried on, explaining the pros and cons of the choice.
Then an analysis of every stage implemented on the board will be performed passing through:

- Generation of stimuli and reference
- Multiplexing
- Reading and acquisition chain

It will be also presented how the power management has been implemented keeping in mind that this board is supposed to be used on the field in Cameroon. In addition to that, the designed layout will be presented and discussed justifying the choices taken. A final part dedicated to a brief introduction of the software coded will end this chapter.

5.1 Possible LIA implementations

As already presented previously, a modulation in the MHz range is of fundamental importance to get useful information on the changing value of the impedance.
Basically, to implement a LIA in the MHz range, nowadays there are 3 options, respectively based on:

1. Field Programmable Gate Array (FPGA)
2. Digital Signal Processor (DSP)
3. Analog multiplier followed by a low pass filter (LPF)

5.1.1 FPGA

To implement a LIA with a FPGA there is the need to generate in the digital domain a suitable sinusoid. In order to do this, lookup tables (LUTs) are used, which are basically an array of values. For instance, a normalized sine wave can be stored there. To correctly output the needed sinusoid LUT values must be scanned with the right timing. Frequency in this kind of systems is synthesized by updating the phase value by a specific phase increment. By scanning the LUT with the latter, the correct frequency signal is output, while to convert it into an analog signal a dedicated DAC must be used, which needs to be fast enough with respect to the sinusoid frequency. The obtained signal can be used to stimulate electrodes, while to read their signal an ADC is necessary, which must fulfil Nyquist sampling theorem, thus resulting in a very high speed component as the demodulation has not been performed up to now. Indeed this is done in the digital domain, in real time, and a subsequent digital LPF stage can be added. There are two types of filters that can be implemented which are finite impulse response (FIR) and infinite impulse response (IIR). The first one is simpler, since it requires no feedback, it's always stable and features a more linear phase compared to IIR. The latter, on the other hand, is more efficient, thus requiring a lower order to implement the same filtering of a FIR, but it is usually harder to design.
The FPGA approach is by far the most versatile among the three. This should be the preferred way to go in the future, when a large quantity of devices will be produced. The ability to push software updates to increase performance is for sure a big advantage, but due to the fact that it is not cost efficient for a single prototype, plus, it would have required a large amount of time and effort to write a proper VHDL code, and keeping in mind that an on field test in Cameroon was scheduled in early 2019, this option has been discarded. Moreover at the beginning of the project it was not very clear how many channels would have required parallel processing and this option is not easily scalable from this point of view.
There are commercially available boards which are FPGA-based like Red Pitaya [36]. This solution uses Xilinx Zynq 7010, it is very expandable, but not really flexible from the custom programming point of view. It has very

high compatibility with software like MATLAB, but it has been discarded anyway due to cost reasons (more than $300) and limitations coming from proprietary software. Going on, Red Pitaya is guaranteed to work properly with EIS for frequencies up to 1MHz, which would not leave any margin for future development or refinements on the actual setup. Furthermore with a $\frac{\Delta R}{R} = 10^{-4}$ and a electrode resistance of around 100Ω, the minimum detectable variation should be $\Delta R = 10m\Omega$, but on the official website it is reported a range going from 100mΩ to 10MΩ.
Due to the previous considerations Red Pitaya has been discarded and the FPGA way is left viable for a future in which mass production will take place.

5.1.2 DSP

The DSP option has been carefully evaluated since it was supposed to bring strong advantages both in terms of ease of development (namely, writing a suitable code) and cost. Since the DSP operates on instructions, or code, the programming mechanism is C, which for this project could mean faster developing times. On the other hand, FPGAs must be programmed with an hardware descriptive language, either Verilog or VHDL. These are languages to describe a specific hardware and then implement it into the FPGA. Moreover, DPSs are characterized by their multiply and accumulate (MAC) capabilities. Since every mathematical operation can require multiple instructions the data must be first captured at the input, then forwarded to the processing core, it then cycles through it for every operation and then it will be released at the output. This is a heavy difference with respect to FPGAs, which, on the other hand, are clock based. This means that a FPGA potentially can perform a mathematical operation on the incoming data stream for every clock cycle. Unfortunately, trying to implement the demodulator digitally means that the ADC must be, also in this case, according to Nyquist sampling theorem, at least twice as fast as the fastest frequency component of the signal of interest. Noting that the modulation happens to be, in the worst case, around 10MHz, at least a 20MSPS ADC is mandatory.
A single chip embedding ADC, DSP and DAC is not something easily found in the market when combined to the specifications of having a high number of bits and a easy to solder package in order to keep the prototype as simple and flexible as possible. Plus, on the board, a system with ADC, DSP and DAC is needed to integrate also sensors' stimulation part.
Among the best commercial solutions there is the "PIC24FJ128GC010" [37], which is Microchip's fastest microcontroller (μC), but with its 10MSPS ADC

and 1MSPS DAC it is not fast enough for the system.
Another solution could have been Texas Instruments's TMS320C2000 DSP [38] which has an almost acceptable speed ADC (12.5MSPS), but the lack of a dedicated DAC makes it an impractical choice.
Pointing the attention to an already developed board seemed the right way to proceed since Altera offers a board with ADC and DAC at suitable speeds (ADC @65MSPS and DAC @125MSPS)[39]. This option has been discarded as well since its cost is around $300, even without accounting for FPGA/DSP cost itself.

5.1.3 Analog Multiplier and LPF

Historically this has been the first implementation ever made of a LIA. It is rather simple compared to the previous ones, but its main downside is represented by its performance. Indeed an analog LIA has bigger offset, limited input dynamic range, bigger $\frac{1}{f}$ at the output and a lower spectral purity. Moreover, for this project, only one demodulation is needed, therefore being doable even with an analog LIA.
This consists just of a multiplier with a LPF in cascade. On the other hand, being the ADC after the demodulator, its requirements are very much more relaxed. If a in-phase demodulation is performed, in principle, the useful signal is at DC frequency: this means that timing performances are not demanding at all and precision requirements are way easier to satisfy on slow ADCs. An analog LIA happens to be the most suited solution for this project being it cheaper and faster to develop with respect to a digital one to be designed from scratch. The downside of this choice is that some degree of flexibility is lost, since in practice only a standard single demodulation is achievable, while in a digital approach multiple demodulations can be managed more easily. Nevertheless it represents a perfect starting point for a prototype.
On the other hand, analog multiplier is not a young approach, so, commercially, not so many solutions are available and the choice fell on AD835.
As clearly discussed before, the main reason behind this choice is to develop a single prototype to validate on the field a developing technology. In other words, the necessity of a compact, low cost, fast to develop system highly pushed the choice to an analog multiplier implementation. Moreover, by having already produced the chips in the same thesis work and having characterized their frequency response, values in play are not so uncertain to justify the extreme flexibility offered by a FPGA approach on the demodulations side. Frequency response has been assessed and the resistive plateau

is expected to be large enough to be exploited in a range of frequencies easily covered by an analog LIA. Nevertheless, an FPGA implementation could represent an important future update once accessing mass market.

5.2 System overview

In this section a general overview of the complete system is given to help the reader follow the subsequent stage by stage discussion. Indeed, Figure 5.1 shows a high level view of the system highlighting also the communications between integrated circuits, Arduino Due and MATLAB, namely the PC.

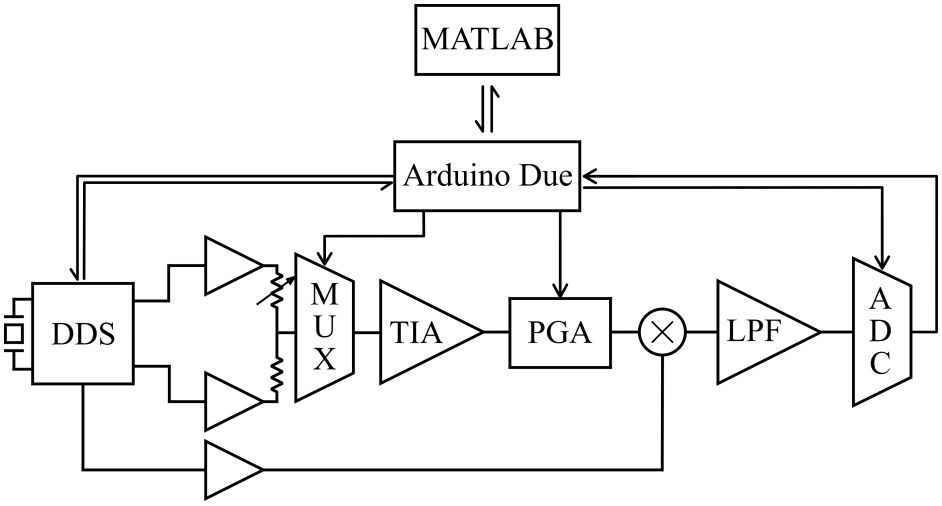

Figure 5.1: Block diagram view of the complete system

The first block is devoted to generate the stimuli for the 4 channel chip. It relies on a clock generator integrated circuit and a direct digital synthesizer (DDS) with 4 differential DACs. Two of those outputs are used to drive the chip and one is employed as reference signal in the analog multiplier stage. Once those stimuli are generated they get converted into two single ended sinusoidal signals and they are provided to the chip by means of a 30 pin board-to-board mezzanine connector. Its number of lines may seem unnecessarily high, but, as highlighted before, crosstalk is a problem which should not be overlooked. The mezzanine has 2 layers of contacts and the board was designed to place the couples of stimuli right above the connection with the virtual ground of the corresponding sensor. Then, at least one connection to ground between the stimuli and three between the virtual grounds readings are placed as shown in Figure 5.2.

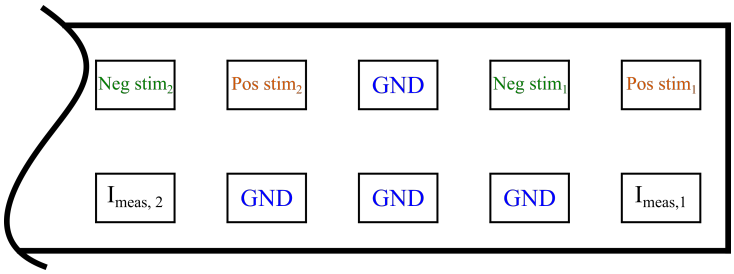

Figure 5.2: Schematic front view of part of the connections implemented in the mezzanine connector

From the chip, 4 differential currents are sequentially read every 250ms by means of a multiplexer stage. The latter connects the reading chain to one channel at a time, allowing the current reading for the aforementioned 250ms, then Arduino Due toggles a new channel selection value, thus changing channel reading. Since this project features a current signal, a transimpedance amplifier operates a current to voltage conversion and feeds its output to a PGA. The latter is used to bring the signal into the correct dynamic for the following analog multiplier, where the demodulation is implemented. A 3^{rd} order Sallen-Key (SK) LPF cell completes the analog LIA implementation with a bandwidth of 100Hz. The latter was selected taking into account noise and a spurious component at twice the original signal frequency arising from the in-phase sinusoidal demodulation. The next stage takes care of converting that analog demodulated signal into a digital one to be provided to Arduino and then to MATLAB for the on-display plot. Arduino Due is the microcontroller selected for this project since it has SPI protocol to communicate with DDS and ADC. Moreover, its high number of digital pins leave a high degree of flexibility for future expansions. Nonetheless, being very popular, it has a wide variety of libraries and support from the community. MATLAB, instead, is the program chosen to manage system synchronization with the motor, as well as to process data and plot them on the PC's display.

5.3 Generation of stimuli and reference signals

This stage has a particular importance since it generates the sinusoidal stimulus for the sensor, thus directly affecting the subsequent measurement. Since this project uses a differential type of stimulus, sinusoid's amplitude is critical and having the possibility to tune it would be a great benefit. Moreover, the number of channels, and therefore of DACs, must be high enough to pro-

duce three sinusoids: a positive one, a negative one and a reference one for the analog multiplier. Sinusoid's frequency should be also tunable, since in a prototyping phase some experiments with different frequency values could be done. Moreover, those DACs should have a sufficient number of bit not to require additional filtering to smooth the waveform. Instead, from the system integration point of view, this stage should communicate with an Arduino Due, therefore SPI protocol would be preferable. For all these reasons, to generate the stimulus signal, an AD9106 by Analog Devices was selected. It is a 12 bit, quad digital to analog converter (DAC) and waveform generator. It features a Direct Digital Synthesiser (DDS) and it is combined with a 540BAA80M0000BAG integrated circuit by Silicon Labs which embeds in the same package a crystal oscillator at a frequency of 80MHz, a dedicated built-in power supply noise rejection filter to achieve a PSRR of -80dBc and a DSPLL to provide a very low jitter clock (typically 125fs). In particular, a DSPLL is a proprietary technology by Silicon Labs embedding a DSP to control a PLL, thus achieving great performance. This oscillator clocks the AD9106 (except for the SPI part, which has its separate synchronous clock) as it is shown in Figure 5.3.
The DDS is a single resource shared between all four DACs. It can generate four sinusoids at a single frequency and a selectable phase. These are determined by specific values loaded in its registers. The tuning word (DDS_TW) register contains the coefficient by which the frequency resolution must be multiplied to have the desired DDS output frequency f_{DDS}. In this case it is a 24 bits wide word giving the possibility of a very fine tuning, especially considering that Equation (5.1) rules DDS's frequency resolution and Equation (5.2) expresses the output frequency achieved:

$$\Delta f = \frac{f_{CLK}}{2^{24}} \tag{5.1}$$

$$f_{DDS} = DDS\_TW \cdot \Delta f = DDS\_TW \cdot \frac{f_{CLK}}{2^{24}} \tag{5.2}$$

where f_{CLK} is the frequency coming out from the oscillator at 80MHz.
The choice fell on the AD9106 thanks to the possibility of tuning individually each of its 4 channels. For instance, each one of the analog gains could be finely adjusted, which is a very useful feature, since a differential measure has to be done, hence the correct amplitude is crucial. Moreover, it can be noted that every sinusoid can be phase regulated individually and even multiplied by a specific pattern stored in the embedded SRAM. Other important features that lead to this choice were represented both by project's requirement of a maximum 10MHz frequency, which is easily satisfied, and by the digital

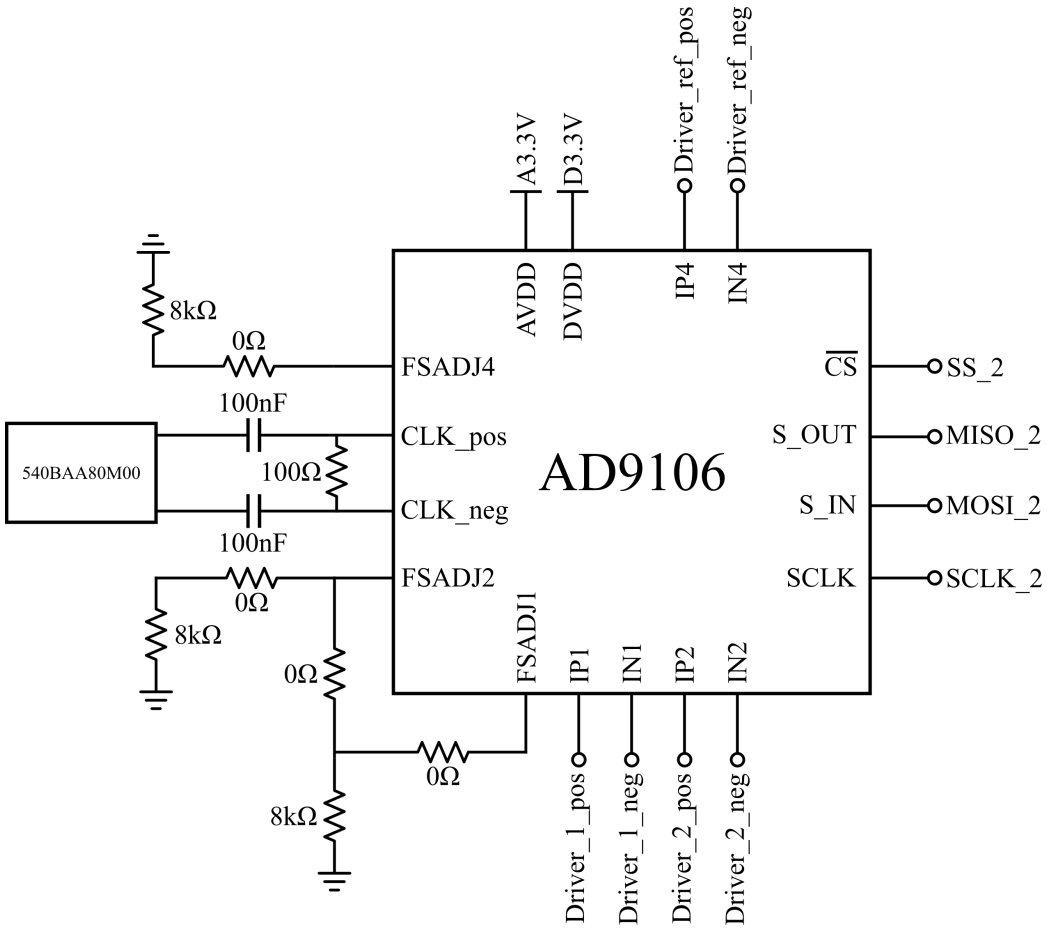

Figure 5.3: Particular of the crystal oscillator and the DDS

transfer protocol Serial Peripheral Interface (SPI). This board must be interfaced with an Arduino Due, which natively supports SPI, therefore protocol compatibility was kept in mind. Going on, both the crystal oscillator and the AD9106 work at 3.3V which is perfectly compatible with Arduino Due's SPI ports. Note as well that analog (A3.3V) and digital (D3.3V) power supplies have been separated as it will be discussed more in depth later.
Analysing AD9106's operation it must be noted that it features an internal band gap reference of 1.04V which, anyway, can be bypassed by externally connecting resistors on its FSADJx pins: for this reason 0Ω resistors were prepared, as can be seen in Figure 5.3, even though they should not be necessary in future. Those pins regulate independently each DAC's reference current I_{ref} which in turn sets the full scale range current $I_{OUT,FS}$ and therefore the output current of each DAC. The possibility to set a different full scale range current for the stimuli part and for the reference part may be used in future, but for now it has been preferred to leave the standard current values of 4mA for the tail generator thus, a complete unbalance, would lead to having a maximum output voltage of 500mV, thanks to the feedback resistor on the TIA shown in Figure 5.4.
To convert the differential current signal coming out from the DACs into a single ended one there are mainly two possibilities[41]: one features transformers and the other one, implemented here, relies on transimpedance amplifiers. The first route provides optimum distortion performance, it is power saving, almost noiseless and simple to implement, since it is just a single package passive component to route. On the other hand, due to project's setup containing high magnetic fields in close proximity to the board, it was impossible to prove its reliability (remember that magnets generate 0.9T each, while Earth only 70μT). Moreover, to keep output resistance low there would be the need for an active driver, thus nullifying the advantages in terms of ease of layout, power saving, and compactness. Therefore, being linearity not a critical parameter, the second approach was implemented. To do this an ADA4897 by Analog Devices has been used to build the TIA, thanks to its very low noise level of only $\left(1\frac{nV}{\sqrt{Hz}}\right)^2$.
The resistive net shown in Figure 5.4 is useful in the case that a sensor may be faulty, thus creating a short circuit and so sinking the maximum current from the amplifier. This way, instead, a resistive path to ground is provided therefore current consumption should never exceed a reasonable value of 12.5mA. So, thanks to that, the operating condition is maintained, even if a sensor out of four is not useful. Moreover, this resistive net would minimize cross-talk phenomena arising when a snub resistor was put on the OpAmp's output to stabilize it. In addition to that, this resistive net steps down the

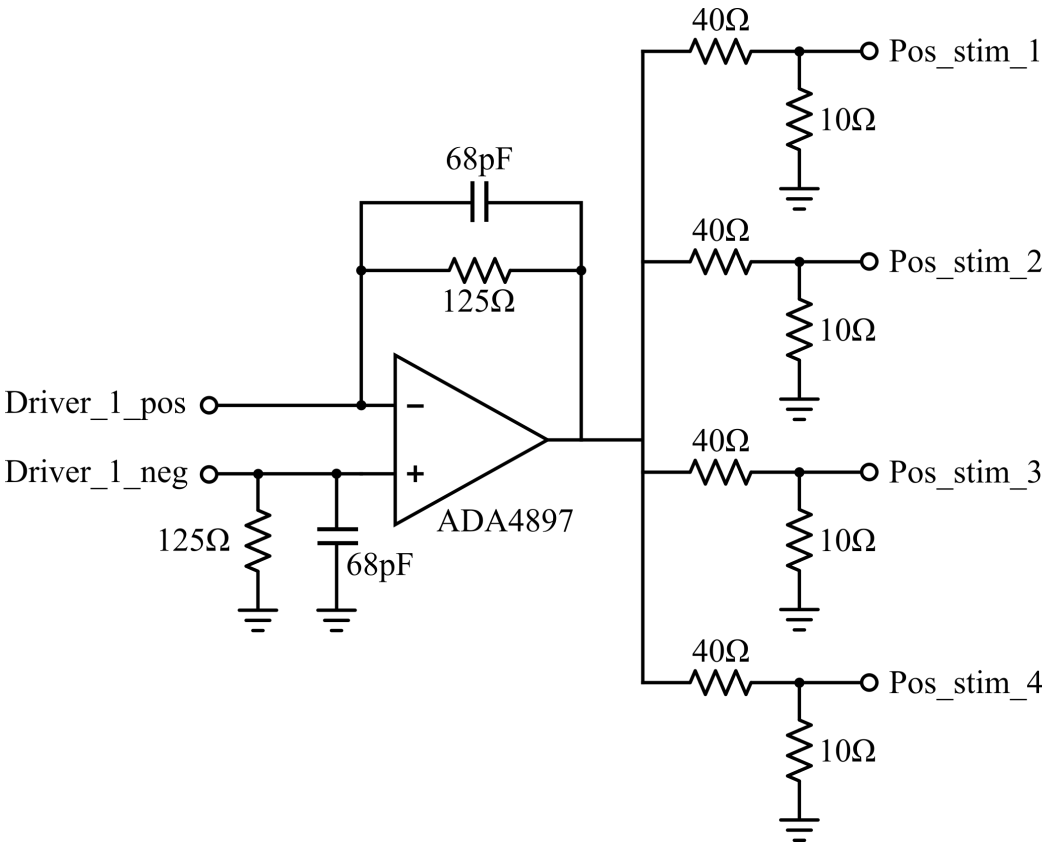

Figure 5.4: Particular of the TIA used to obtain a voltage stimulus

500mV stimuli to 100mV, thus reducing TIA's noise.
The complementary stage devoted to create an anti-phase sinusoid uses a different AD9106's output. It is not shown, as the only difference is software thanks to the possibility offered by the AD9106 to insert a phase value by programming a specific register.
For what concerns the frequency analysis of the stimuli part, it must be noted that the ideal gain from the DAC output to the sensor is 125Ω up to the frequency given by the feedback capacitor and resistor which is approximately 20MHz, more than enough for a 1MHz measurement.

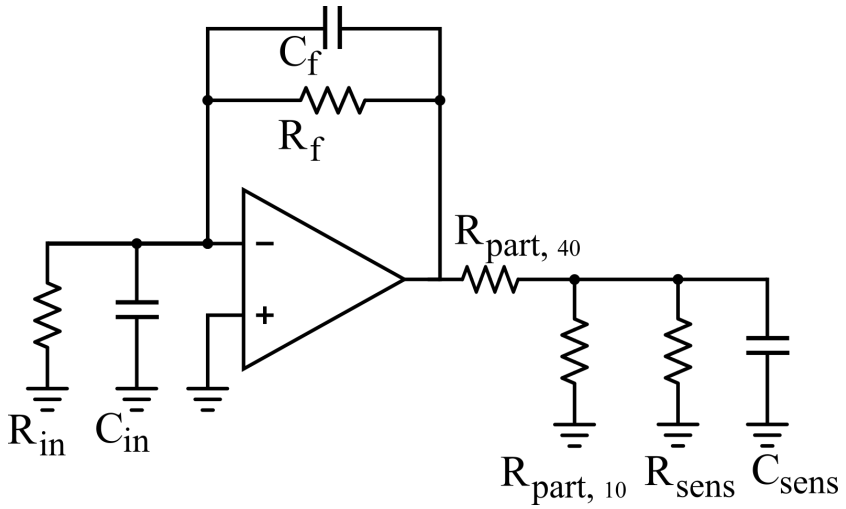

Figure 5.5: Model of a TIA

In Figure 5.5 an equivalent model of a TIA is reported to analyse its stability. It must be noted that the ADA4897 is unity gain stable, indeed, at high frequency, with $C_{in} = 11pF$ from the amplifier input and $C_f = 68pF$ by design, the capacitive partition is $\frac{C_f+C_{in}}{C_f} \simeq 1.17$, so the selected component is perfectly suited for this job. Moreover R_{in} is 10 kΩ, and DAC output capacitance is not even reported in the official datasheet, thus assumed to be negligible.
As far as the noise is concerned, the dominant contribution at the amplifier output is represented by the feedback resistor which brings approximately $\left(1.45\frac{nV}{\sqrt{Hz}}\right)^2$ and the OpAmp voltage noise itself, even if it is $\left(1\frac{nV}{\sqrt{Hz}}\right)^2$. All in all, accounting for the DAC output resistance, the OpAmp's input one, feedback resistor and resistive net on their output, no more than $\left(2.5\frac{nV}{\sqrt{Hz}}\right)^2$ should be present at the generation stage output. Then, the resistive partition lowers this value to $\left(0.5\frac{nV}{\sqrt{Hz}}\right)^2$. A brief calculation with the usual $4KTR_{sens}$ gives a voltage noise contribution of $\left(1.29\frac{nV}{\sqrt{Hz}}\right)^2$, which, compared

with the obtained noise from the stage before, sets noise requirements for the reading chain.
The same discussion applies to the amplifier used for the reference signal with slightly different values. Since its output is directly fed to the analog multiplier, which has a maximum range of ±1V, the resistance value was doubled, obtaining a R_f of 250Ω. To keep the bandwidth unchanged C_f this time is set to 34pF, therefore the high frequency partition is $\frac{C_f+C_{in}}{C_f} \simeq 1.32$. Then, a passive high pass filter has been placed in order to cancel out every DC spurious component before passing the obtained signal to the analog multiplier.

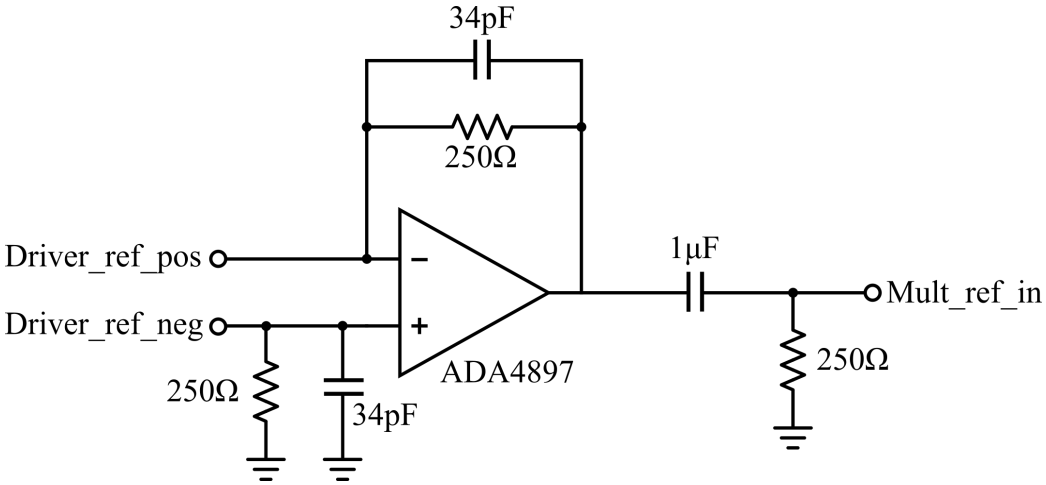

Figure 5.6: Particular of the TIA used to obtain the voltage reference

5.4 Multiplexers

Since this project exploits in liquid measurements, simple analog switches where the state is either closed or open, were not sufficient. In fact, voltage differences must be kept under control not to trigger red-ox reactions at the interface electrode-electrolyte. Moreover, leaving their input floating, whenever they get connected some transient will arise. For those reasons, the attention has been redirected to single-pole double-throw switches. In this case the connection is made either with the virtual ground of the transimpedance amplifier, or with system ground, keeping sensor's potential well defined at every time instant. Note that, to avoid any transient due to the instant application of a voltage step, the stimulus of each sensor is continuous in time and only the current reading is switching. What has been done

to correctly read all the currents is to make use of two MAX4622 [42] which are analog switches controlled by digital pins in TTL/CMOS-Logic, shown in Figure 5.7.

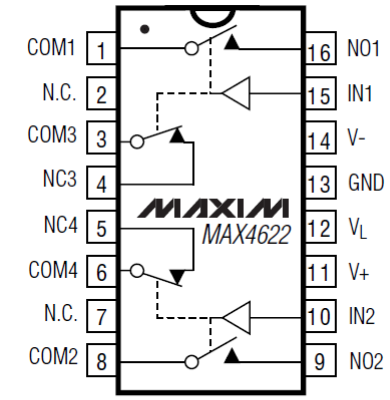

MAX4622		
LOGIC	SWITCHES 1, 2	SWITCHES 3, 4
0	OFF	ON
1	ON	OFF

SWITCHES SHOWN FOR LOGIC "0" INPUT

Figure 5.7: Pinout configuration of the MAX4622

Thanks to this compatibility the aforementioned Arduino Due can easily control their switching period. Project's specification was to switch between channels to read each of them every 250ms, therefore an Arduino Due is more than enough for this purpose.
Moreover, choosing the analog switches, an important trade-off appeared: the lower the on state resistance R_{on}, the bigger the on state capacitance C_{on}. For this project a low R_{on} was crucial, therefore, since they exhibit a very low resistance (3Ω typically) and good matching properties between channels, with their worst case $\Delta R_{on} = 0.5\ \Omega$, those multiplexers are perfectly fulfilling project's requirements. Unfortunately, as mentioned earlier, all these resistance parameters come at the expenses of a rather large on-state capacitance C_{on} of about 150pF and a off-state capacitance C_{off} nearly of 35pF. Those capacitances are detrimental for noise performance, so they enforce severe requirements on the operational amplifier to be used in building the TIA designed for current reading.
Among other features, they can be supplied with voltages already present on the board, limiting the complexity of the layout and keeping costs low.
Another important feature is possibility of controlling each switch individu-

ally, so to allow the reading of only one sensor at a time without affecting the other three, thus leaving them to the normally close state. The last is ease of maintenance. Keeping in mind that this project will be used on the field in Africa, ease of soldering, inspection and repairing are not second order advantages, so the choice of MAX4622 is now fully justified thanks to its SOIC-8 package.

5.5 Reading and acquisition chain

The acquisition chain is the key part of this readout board. It should be carefully designed not to worsen the signal-to-noise ratio and to allow a proper reading by the Arduino Due for the consequent post processing. This chain mainly consists of a TIA, implemented to read the current signal coming from the electrodes, a programmable gain amplifier (PGA), to further condition the signal, an analog multiplier, which implements the actual demodulation, a low pass filtering (LPF) stage as anti-aliasing filter before the analog-to-digital conversion to finally acquire the signal, pass it to the Arduino Due and then MATLAB for the on screen display of the measurement. In Figure 5.8 there is a visual sum up of what has been stated right now.

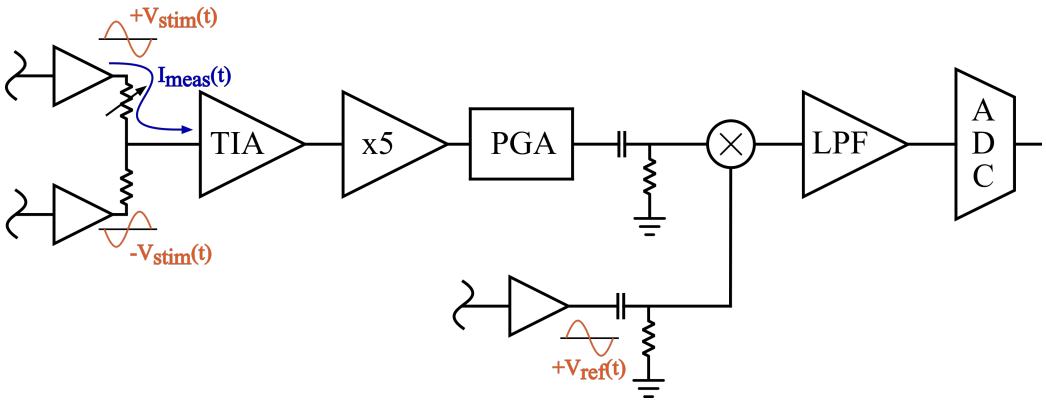

Figure 5.8: Schematic view of the acquisition chain

5.5.1 Transimpedance Amplifier (TIA)

As the chip itself performs a voltage to current conversion it is natural to pick up this signal with the virtual ground of a feedback operational ampli-

fier. Since the signal is modulated in the MHz range 1/f noise is not very important neither it is OpAmp's offset which is a pure DC non ideality. Furthermore, later in the chain, a passive HPF has been implemented to clean out every low frequency disturbance. It is very important, on the contrary, that this component features a ultra-low white noise not to overwhelm the tiny signal coming out from the chip. Referring to Figure 5.9, and keeping in mind that the current noise spectral density introduced by the sensor is a $\left(\frac{4KT}{R_{sens}}\right)^2$ of $\left(12.87\frac{pA}{\sqrt{Hz}}\right)^2$, the stage was designed.

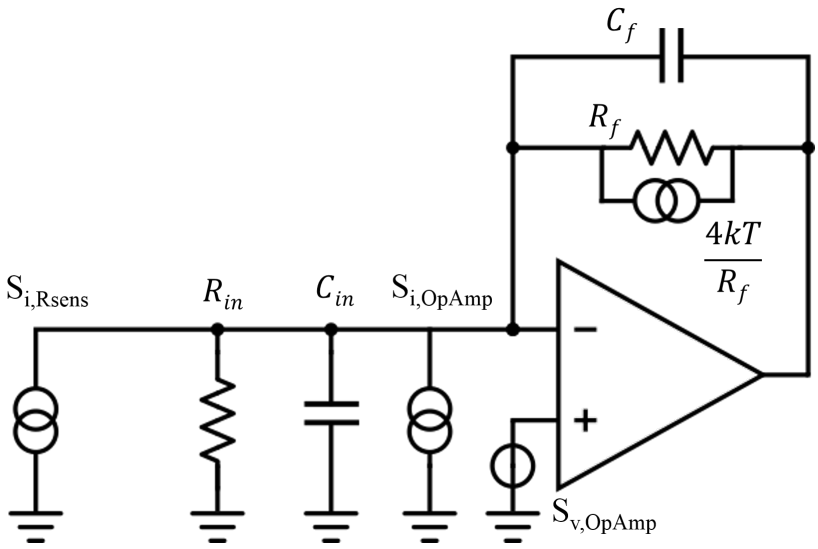

Figure 5.9: Model of a TIA, including all the noise generators

The condition to satisfy, in order not to limit the achievable resolution with the electronics, is reported in Equation (5.3). Basically, it asserts that the current noise coming from the chip must be greater than all other current noises contribution of the electronic reading, namely OpAmp's current noise, feedback resistor's current noise and OpAmp's voltage noise properly reported on the input pin through the division by the impedance seen from that pin to ground. In order to perform this calculation it has been chosen to compare noise contributions in current at the virtual ground pin of the feedback OpAmp.

$$S_{I,\,R_{sens}} > S_{I,\,OpAmp} + \frac{4KT}{R_f} + \frac{S_{V,\,OpAmp}}{\left|Z_{vg}\right|^2} \tag{5.3}$$

Z_{vg} is the impedance present at the virtual ground node toward ground. It

is formed by the parallel of Z_{in} and Z_f and it turns out to be:

$$Z_{vg} = \frac{R_{sens}//R_f}{1 + s \cdot (C_{in} + C_f) \cdot (R_{sens}//R_f)} \tag{5.4}$$

With the chosen multiplexers and one channel selected, by considering in parallel the on-capacitance $C_{on} = 150pF$ of the MUX, three off-capacitance $3 \cdot C_{off} \simeq 100pF$ and sensor's parasitic capacitance C_{sens} of 100pF, a C_{in} of 350pF is calculated. By design, on the other hand, the feedback has been chosen to be resistive around the operating frequency. Moreover, a trade-off is present when choosing R_f: a high value would be desirable from signal point of view, but it would decrease the bandwidth. To leave the latter unchanged C_f should be decreased accordingly. Nevertheless, in so doing, the capacitive partition made with C_{in} would decrease as well, so, to guarantee the same closed loop bandwidth more stringent requirements are enforced onto the OpAmp used for the TIA. Hence, a 1kΩ R_f value has been deemed reasonable, and given bandwidth constrain of 20MHz, a feedback capacitance C_f of 8pF was used. Note that, being C_f practically negligible with respect to C_{in}, according to Equations (5.4) and (5.3) it can be said that noise performance has not been worsened. Indeed, at high frequencies, Z_{vg} can be considered to approach $\frac{1}{sC_{in}}$ and by substituting the expected working frequency of 1MHz with an additional safety margin of 2, Equation (5.3) numerically becomes Equation (5.5):

$$\left(12.87\frac{pA}{\sqrt{Hz}}\right)^2 > \left(5.2\frac{pA}{\sqrt{Hz}}\right)^2 + \left(4\frac{pA}{\sqrt{Hz}}\right)^2 + \left(1\frac{nV}{\sqrt{Hz}}\right)^2 \cdot (4mS)^2 \tag{5.5}$$

By selecting as OpAmp the AD8099 by Analog Devices, which features extremely low noise values as shown in Equation (5.5), it can be seen, in Equation (5.6), that the previously explained requirement is clearly fulfilled.

$$\left(12.87\frac{pA}{\sqrt{Hz}}\right)^2 > \left(7.8\frac{pA}{\sqrt{Hz}}\right)^2 \tag{5.6}$$

As far as stability is concerned, the $\frac{1}{\beta}$ has been analysed. Basically, it is the reciprocal of the transfer function between the output of the OpAmp and its input (in this case the negative one), through the feedback network. It will be discussed with the help of Figure 5.10.
The feedback path gives birth to a $\frac{1}{\beta}$ that is:

$$\frac{1}{\beta} = \frac{R_{sens} + R_f}{R_f} \cdot \frac{1 + s \cdot (C_{in} + C_f) \cdot (R_{sens}//R_f)}{1 + s \cdot C_f \cdot R_f} \tag{5.7}$$

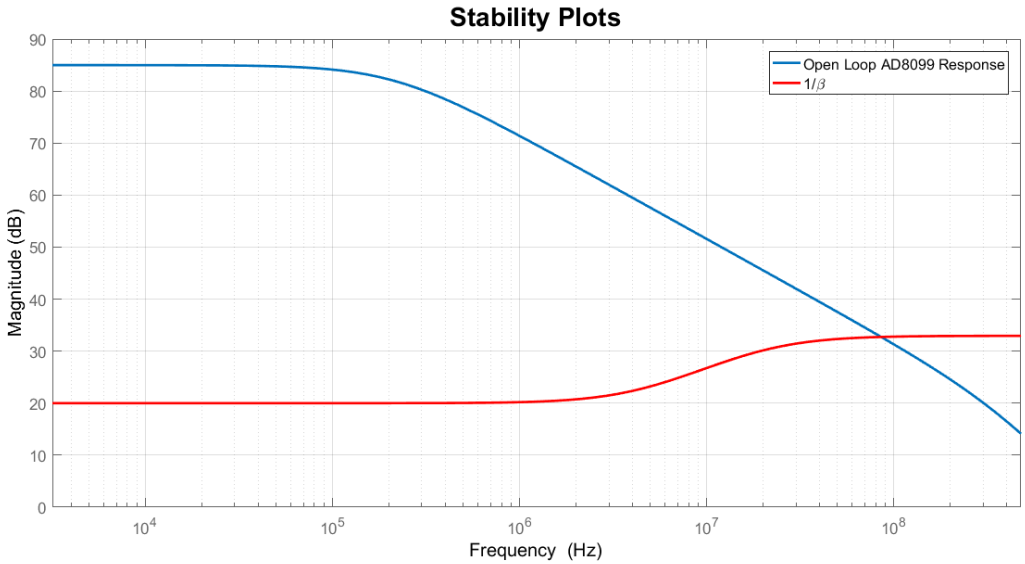

Figure 5.10: AD8099: Closed Loop stability evaluation

So, from Equation (5.7), it can be seen than at low frequency $\frac{1}{\beta}$ gain is 10 (20dB), while at higher frequencies the capacitive partition sets the gain at 45 (roughly 33dB). From this, with the usual gain-bandwidth product (GBWP) rules, a crossing frequency f_{cross} of around 84MHz is assessed. Moreover, the pole frequency $f_{p,\frac{1}{\beta}}$ is 20MHz, directly set by choosing the bandwidth, while the zero is mainly set by the sensor at a frequency $f_{z,\frac{1}{\beta}}$ of 4.45MHz. For what concerns the OpAmp, in its datasheet a GBWP of 3.8GHz is declared, therefore, dividing by its 85dB DC gain, a first pole at a frequency $f_{p_1,OpAmp}$ of 213zz is assessed. Going on, by inspecting the open loop gain plots in its datasheet a second pole around an $f_{p_2,OpAmp}$ of 400MHz is found and so included in the simulation. To check stability, phase margin was calculated by means of Equation (5.8):

$$\Phi_m \simeq 90° - tg^{-1}\left(\frac{f_{cross}}{f_{z,\frac{1}{\beta}}}\right) + tg^{-1}\left(\frac{f_{cross}}{f_{p,\frac{1}{\beta}}}\right) - tg^{-1}\left(\frac{f_{cross}}{f_{p_2,OpAmp}}\right) \tag{5.8}$$

where 90° accounts for the first pole contribution, which is assumed to be complete as it is at 213kHz. By plugging in the numbers exposed before a phase margin Φ_m of about 65° was calculated, therefore leading to a stable stage. In the design phase of the board, an additional degree of safety has been taken by placing a 20Ω snub resistor at the output of the TIA to

decouple any capacitive load that would have been possibly driven. Furthermore, by considering chip capacitances as lumped, while in reality they are distributed, errors can arise especially for a high frequency analysis. By connecting with short traces a well known capacitive component the loop gain can be considered well defined in the frequency range of interest. On the other hand, by raising the C_{in}, noise performance will be worsened accordingly. This operational amplifier features a compensation pin to finely tune the open loop frequency response. The compensation capacitor decreases the open-loop gain at higher frequencies where the phase is degrading, therefore a better phase margin is achieved, reaching stability. Being the typical range 0 to 5 pF, a C_c of 0.5pF was used. When soldering a capacitor to a pin a parasitic LC resonant circuit is created with the lead inductance of the package. To avoid this, a 50 Ω resistor has been used to dampen it. In parallel to it a capacitor footprint has been prepared in case of a future need. Its role would be to decrease the peaking at low closed-loop gains. A complete view of the TIA implemented in the schematic is available in Figure 5.11.

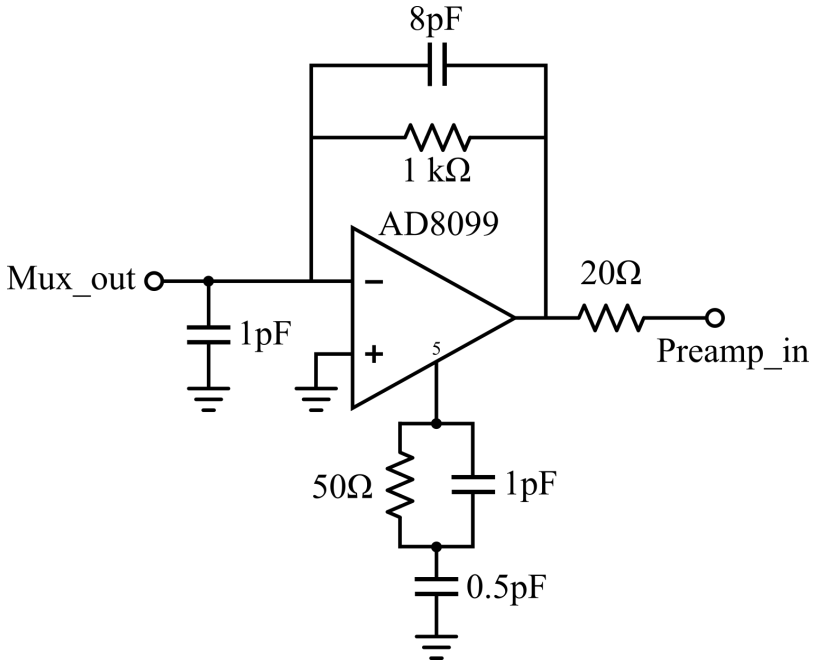

Figure 5.11: Schematic of the implemented TIA. In particular, pin 5 requires the connection of an external compensation network

To spend some more words on signal and noise, it is important to note that, as highlighted in the previous chapter, a minimum current signal around 30nA is expected to appear at the virtual ground node. Then, thanks to

R_f, a current to voltage conversion takes place and at TIA's output a 30μV signal is present, while a voltage spectral density of $\left(15\frac{nV}{\sqrt{Hz}}\right)^2$ is also there. This tiny signal is superimposed to a much greater one arising from the mismatches between variable resistor and its reference one. In the case of ideal matching no current, except for the one due to the variation of resistance, flows in the virtual ground, therefore the TIA should be implemented with a very high resistor to have a nice signal on its output. Unfortunately a perfect match is never achievable, so a maximum 10% mismatch is taken in consideration. A feedback resistor of 1kΩ has been chosen, so to have a 50mV_{pk} in case of 10% mismatch and a 5mV_{pk} in the case of 1% mismatch.

5.5.2 Programmable Gain Amplifier (PGA)

After the TIA it has been decided to place a PGA. The choice comes from the fact that the following analog multiplier is very noisy, therefore there is the need to have a signal as large as possible. The limitation in this sense comes once again from the analog multiplier, which has a dynamic range of $\pm$1V. Moreover, due to mismatches in the chip, there are various possible signals coming from the TIA which can range between 5 and 50 mV_{pk} respectively for 1% and 10% matching. For those reasons it has been deemed useful to add a PGA, which can be controlled in TTL/CMOS logic by the Arduino Due. In a future update this may even be synchronous to channel switching, therefore implementing a custom gain control for each channel. The selected component is a THS7001 by Texas Instruments (TI). The choice fell on this device thanks to the fact that its bandwidth is fulfilling project's requirements as well as its gain interval. In addition to that gain selection is very simple thanks its previously mentioned TTL/CMOS logic. Moreover, it has a built-in low noise preamp, as shown in the block diagram reported in Figure 5.12.
The possibility to use the preamp is very important as it features a $\left(1.7\frac{nV}{\sqrt{Hz}}\right)^2$ voltage noise spectral density that, compared to the already present $\left(15\frac{nV}{\sqrt{Hz}}\right)^2$, is negligible. On the other hand, the PGA itself is a lot noisier ranging from $\left(10\frac{nV}{\sqrt{Hz}}\right)^2$ in the maximum gain configuration (10 linear or 20dB), up to $\left(500\frac{nV}{\sqrt{Hz}}\right)^2$ for the minimum gain one (0.08 linear or -22dB). For sure an attenuation will not be used in this stage but in the worst case, which from the noise point of view is lower gain, an amplification of 2.5 linear is used and looking into the datasheet a $\left(25\frac{nV}{\sqrt{Hz}}\right)^2$ is obtained. Without the preamp this would be directly present at TIA's output, therefore not being negligible with respect to the $\left(15\frac{nV}{\sqrt{Hz}}\right)^2$ already present, so worsening noise performance. By implementing a gain of 5 for the preamp stage all the noise contributions

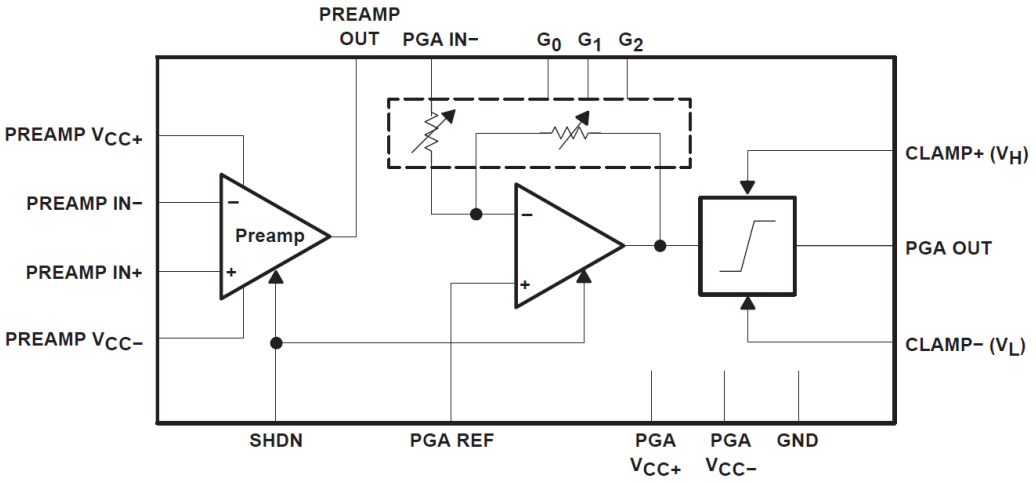

Figure 5.12: Block diagram view of the THS7001

coming from the PGA are no more relevant and, in addition to that, a total gain higher than the maximum 10 is achieved. Going on in the discussion, it must be noted that the preamp has a declared gain-bandwidth product of 100MHz, which, combined with the aforementioned gain of 5, gives a closed loop bandwidth of 20MHz, more than a decade higher than the stimulus frequency. From the DC non idealities point of view it must be said that the AD8099 has a typical offset of 100μV, which amplified by 10, becomes a 1mV contribution at preamp input. The latter adds its own 5mV offset, thus resulting in 30mV DC impurity at PGA's input. In the worst case, namely an amplification of 10, 300mV are present at PGA output, which, in the case of a 10% mismatch could result in a dynamic limitation enforced by the following analog multiplier and thus, in distortion. For this reason a passive HPF stage has been between the two. This way, DC non idealities are not important as well in this stage.
In the implemented design a distinction between the two mismatch cases must be done. In the case of 10% mismatch the input signal resulting from a minimum resistance variation is 30μV, superimposed to a 50mV$_{pk}$, which ends up in a output signal of 375μV, on top of a 625mV$_{pk}$ signal. In this case, with a PGA amplification of 2.5, the noise at its output becomes $\left(187.5\frac{nV}{\sqrt{Hz}}\right)^2$. On the other hand, in the case of 1% mismatch, the amplification is 10, while the input signal is of course the same. However, superimposed to a lower 5mV$_{pk}$ one, so, after this stage, a 1.5mV signal on top of a 250mV$_{pk}$ one is present. The noise, instead, becomes $\left(750\frac{nV}{\sqrt{Hz}}\right)^2$. Those amplification levels were chosen to leave enough room for a bigger signal coming from the sen-

sor without risking to saturate the following analog multiplier. Using LIA bandwidth of 100Hz a SNR of 44dB is calculated.

5.5.3 Analog multiplier

To implement the actual multiplication an AD835 by Analog Devices has been utilized. This is made in a complementary bipolar process, hence the need to keep HPF's resistor value low: in fact, as can be seen on its datasheet, a 10μA bias current is present at both its input pins. The HPF is a passive one since high attenuations are not needed. Pole frequency is set by its capacitor and resistor values. The former has been chosen of 1μF, while for the latter a trade-off arose. A high resistor value was requested because PGA's output resistance is 20Ω, thus at least a decade had to be taken not to create unfavourable partitions, but on the other hand, a low resistor value is useful to better filter low frequency disturbances. For these reasons it has been selected a resistor value of 200Ω. On the reference stimulus branch an identical HPF filter was placed to keep the stage symmetric.
With this HPF sizing the resulting DC disturbance is 2mV. For comparison, an offset voltage of $\pm$3 to $\pm$20mV is declared in the datasheet, thus being more limiting than the one introduced by bias currents. AD835 is also pretty noisy with a voltage spectral density of $\left(50\frac{nV}{\sqrt{Hz}}\right)^2$, but it ends up being negligible when compared to the noise values reported earlier.
In Figure 5.13 a block diagram of the analog multiplier is shown.

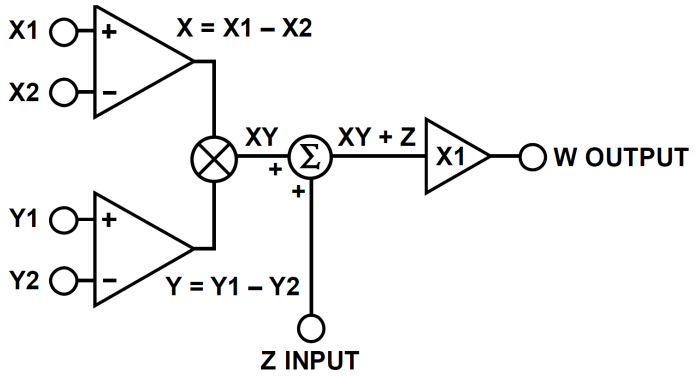

Figure 5.13: Block diagram of the analog multiplier

Both inputs have a linear dynamic range of $\pm$1V, which can not be fully exploited by the signal branch, due to the variability and mismatches, but it actually is on the reference path, as discussed in Section 5.3. The main drawback brought by the impossibility of using the complete dynamic is that,

by operating a demodulation using a sinusoid a factor of 2 is lost, therefore further attenuating the signal.

$$A \cdot sin(\omega t) \cdot B \cdot sin(\omega t) = \frac{A \cdot B}{2} + \frac{A \cdot B}{2} \cdot sin(2\omega t) \tag{5.9}$$

Moreover, as illustrated by Equation (5.9), the input signal splits in two parts: the first one is at DC frequency; the second one, instead, is a sinusoidal signal at double the frequency of the original one.
AD835 was also chosen thanks to its Z input pin, which allows the user to sum another signal to the demodulated one. In this project, to shift the dynamic upward to half the supply of the ADC, a reference voltage of 1V was connected to this pin. This is supplied by an ADR130 voltage reference by Analog Devices. With its $3\mu V_{p-p}$ it can provide a very clean and stable voltage, therefore it has been chosen to perform this DC shift. So, at multiplier's output there can be a range of possible signals which are mainly depending on the mismatch once again. In the first case of a 10% mismatch, the useful signal is expected to be 187.5μV at DC, superimposed onto a 312.5mV both at DC and at the frequency discussed earlier. Voltage noise should be of the order of $\left(130\frac{nV}{\sqrt{Hz}}\right)^2$ instead. On the other side, in case where a 1% mismatch is present, the useful signal should be 750μV at DC, laying on a 125mV DC and AC voltage. Its related noise is expected to be $\left(530\frac{nV}{\sqrt{Hz}}\right)^2$. Note that noise levels are a factor of two lower in power than the input levels, thanks to the multiplication. Indeed white noise components have random phase and an equal probability to occur. Therefore, its power is split in two halves: one is in-phase, the other in quadrature. Those components are equal and they feature half the input noise power.
Nevertheless, being signal halved as well, but linearly, the SNR is worsened by a factor $\sqrt{2}$.

5.5.4 Low Pass Filter (LPF)

At this point the signal is still buried in noise, hence the need, to complete an effective LIA measurement, to perform a narrow band filtering. It has been chosen to go for a 3^{rd} order Sallen-Key[43] (SK) cell. One of the advantages of this filter typology is its simplicity, while its major drawback is represented by components' interactions which hinder an easy tuning. It has been decided to use a non inverting filter to bring the DC voltage of 1V at half the ADC dynamic, which is between 0 and 5V. Indeed, in this stage, a

non inverting gain of $1+\frac{3}{2} = 2.5$ was implemented. Moreover, signal's dynamic benefits from this amplification, thus being wider at the ADC input. In Figure 5.14 the actual schematic and the choice of values are shown. To avoid stability issues a 0Ω resistor footprint has been placed at its output in case it will be necessary to add a snub resistor.

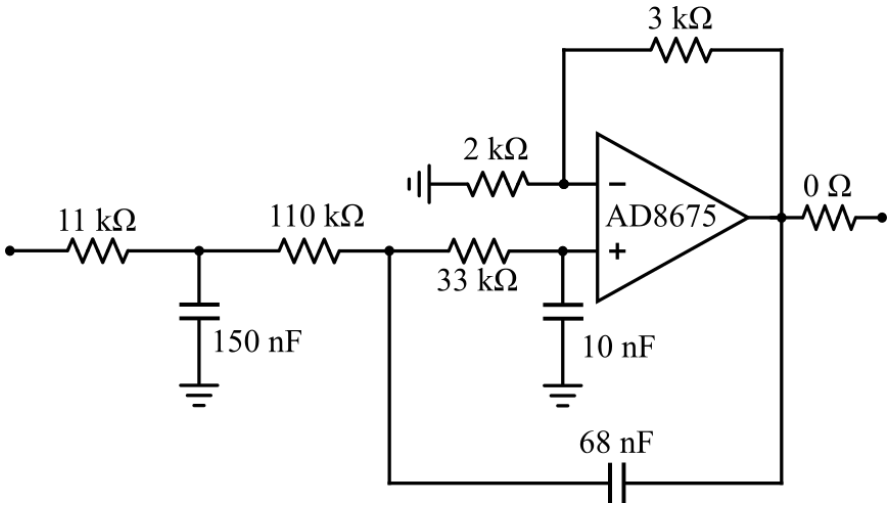

Figure 5.14: Schematic of the implemented 3^{rd}-order SK LPF

The proposed sizing will bring the pole at a frequency of 100Hz. This choice is mainly due to the attenuation needed for the signal at twice the stimulus frequency, which is still present superimposed to the useful signal. A minimum attenuation of -160dB is obtained at 2MHz, where the unwanted signal is expected to be. A closed form of a 3^{rd}-order Sallen-Key does not exist, therefore a numerical simulation has been performed leading to the frequency response reported in Figure 5.15.
To implement the SK cell, unlike the rest of the chain, low frequency and DC performances are critical not to worsen the DC signal, which is the one of interest that will not be filtered out. To this purpose an AD8675 by Analog Devices was selected. Among its features there are ultra low DC offset voltage, typically of 10μV, as well as a very low temperature offset drift coefficient of $0.2\frac{\mu V}{^\circ C}$. The latter is a very important parameter in this project since temperature fluctuations usually occur at very low frequencies and could easily cover the useful signal. Another key feature is the very low noise, both wideband and $\frac{1}{f}$. White noise is not a big problem since the input signal comes with a $\left(130\frac{nV}{\sqrt{Hz}}\right)^2$ voltage spectral density and, in addition to that, the bandwidth of 100Hz is very narrow. The real problem is $\frac{1}{f}$ noise. Indeed, these kind of measures are at risk of being buried in pink noise if

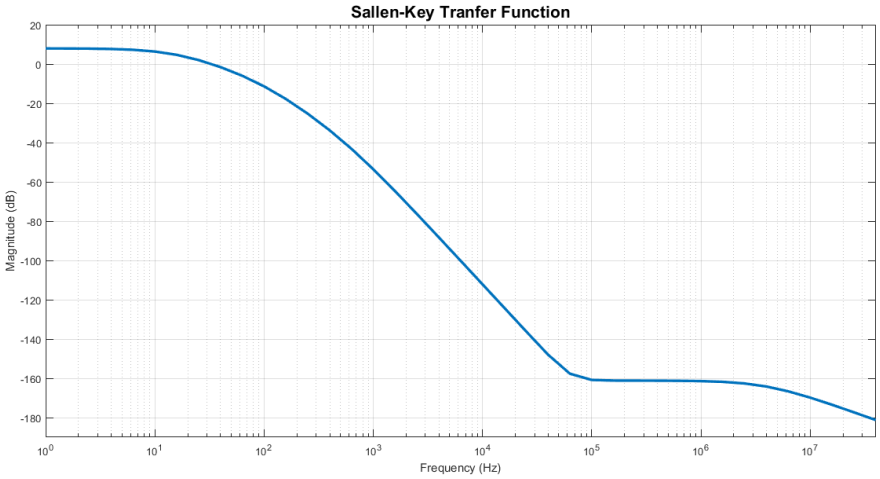

Figure 5.15: Frequency response of the 3rd order LPF stage

the component selection is not made carefully. In its datasheet a $0.1\mu V_{p-p}$ is declared between 0.1 and 10Hz, which must be compared to the white noise ones. Those depend on resistance mismatch, but the minimum RMS value for a 10% mismatch is around $4\mu V_{RMS}$, which makes $\frac{1}{f}$ negligible. Again, it is important to understand which are signals' ranges. In the case of 10% matching, at LPF's output, a $470\mu V$ signal is present on top of a 800mV one. With a linked voltage noise of $\left(325\frac{nV}{\sqrt{Hz}}\right)^2$ and a bandwidth of 100Hz, as said earlier, a resulting $4\mu V_{RMS}$ is obtained. On the other hand, with 1% matching, a 1.875mV signal stays onto a 312.5mV one, and they go along with a $\left(1.325\frac{\mu V}{\sqrt{Hz}}\right)^2$ voltage noise. Being the bandwidth of course the same, $16.6\mu V_{RMS}$ are present, therefore none of the possible cases can be limited by the active stage. The achieved signal to noise ratio (SNR) is around 41dB, thus leading to the possibility of reading clearly signal of interest. To conclude, note that, as said earlier, all of the above mentioned signals are sitting on top of a 2.5V DC voltage signal resulting from the amplification of the 1V offset brought to the analog multiplier.

5.5.5 Analog-to-Digital Converter (ADC)

Now that the DC information has been extracted, a digitalization stage is necessary to bring data to the Arduino Due. Knowing that the minimum signal that shows at the ADC input is around $470\mu V$ and that ADC's input dynamic is 5V, by means of Equation (5.10) the minimum number of bit is

calculated:

$$n_{bit} > log_2\Big(\frac{5V}{470\mu V}\Big) = 13.37\,bits \tag{5.10}$$

therefore at least 14 bits are needed.

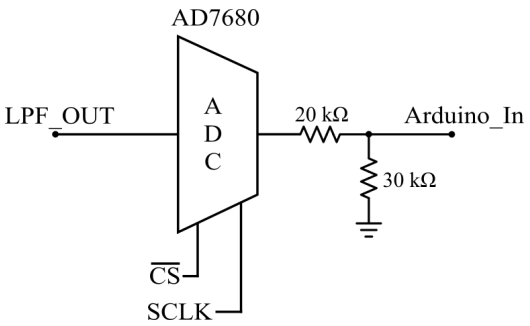

Figure 5.16: Schematic view of the ADC stage

The selected converter was the AD7680, again by Analog Devices. Being a 16-bit ADC it fulfils number of bits requirement. Moreover, this is a successive approximation register (SAR) ADC which was preferred to switched capacitor alternatives to protect over noise injection. Going on, it was chosen also thanks to the possibility of supplying it with 5V, thus making its layout routing simple since it is a voltage already present in the board. Moreover, being its reference voltage internally derived from its supply voltage, this directly affects its input dynamics, which is therefore in the range of [0V, 5V]. From those data a least significant bit (LSB) of 76μV was assessed. Moreover, it supports serial peripheral interface (SPI) as communication protocol, thus being perfectly compatible with Arduino. The only thing to take care of is to put a resistive divider between the digital output of the ADC and the input of the Arduino Due (as shown in Figure 5.16), since AD7680's output reaches 5V and this would break Arduino's 3.3V rated input port. On the other hand, 3.3V are enough to toggle the high level on the ADC.
Another very useful feature is represented by the possibility of asking for data asynchronously with Arduino. Indeed, just by driving a specific ADC pin, the chip not selected ($\overline{\text{CS}}$) one, the conversion starts and in 24 clock cycles it is over. Moreover, its maximum throughput rate is of 100kSPS (samples per second), which is a relaxed specification, not to get Arduino stuck by unnecessarily processing too much data.
About the frequency of operation a trade-off was considered. By having a higher frequency a more effective oversampling is made possible. The latter can be defined as the ratio between the sampling frequency and Nyquist frequency for the signal of interest as shows Equation (5.11) defining the

oversampling factor N:

$$N = \frac{f_{sampling}}{2 \cdot f_{signal}} \tag{5.11}$$

Oversampling is a technique which gives better SNR if noise components are white. In this case, in fact, noise components have equal probability to occur, therefore, when averaging, their variance is lower by a factor equal to the oversampling factor N, so SNR linearly increases by $\sqrt{N}$. Therefore, since a 100Hz filtering has been designed, a Nyquist frequency of 200Hz is requested, so by sampling at a $f_{sampling}$ of 1kHz an oversampling factor N of 5 is achieved.
To compute the obtained SNR with oversampling, in dB, Equation (5.12) was used:

$$SNR_{OS} = SNR_{start} + 10 \cdot log_{10}(N) \tag{5.12}$$

where SNR_{start} is the starting SNR without oversampling.
This enhances SNR from 41 to around 48. In case the maximum frequency of 100kHz will be used a SNR of 68 could be achievable.

5.6 Power Supplies Design

To feed power to this board a HAA15-0.8-AG linear power supply from Bel Power Solutions was selected. This is an external supply aiming to convert the AC 220V of Cameroon's electricity grid as well as 230V Italian one into ±12V DC. For what concerns its outputs they are three: ±12V providing up to 1A and ground.
On the board 4 different supplies are present: -5V, analog 3.3V (A3.3V), digital 3.3V (D3.3V) and 5V. In order to obtain those values, linear regulators have been employed. It has been looked for an external power supply having ±7V or ±8V outputs to connect to regulators inputs. However, combined with the requirements of being linear and having a ground output to share the same ground potential across the whole system, no option was found, hence the only solution was to use this ±12V external power supply, even if power dissipation problems may arise on the board regulators as it will be discussed later.
The choice of a linear power supply goes along with the one of selecting linear regulators as well for the on-board part of the project: this way noises introduced by switching regulators are avoided. The main drawback is that linear power supplies usually feature cleaner output voltages at the expenses of efficiency, thus dissipating more power. This is not a detail at all since for the operation in African market the ambient temperature must be considered

significantly higher than the normal 25°C, so heating problems may arise.
To evaluate the junction temperature of a component, which in brief is the one reached by silicon inside the package, three parameters must be taken into account: its voltage drop, output current and thermal resistance.
Due to thermal considerations it has been chosen to step down the ±12V to ±7V by means of two regulators, thus splitting power dissipation in two halves. This choice will be fully justified in Subsections 5.6.1 and 5.6.2. Moreover, an early assessment of the temperature reached by the on board regulators has been done to determine whether additional heatsinks should be mounted or not. To show at a glance the estimated currents flowing in each branch of the power supply network and regulators estimated final temperatures Table 5.1 is reported. Those temperature values are reached just by stepping down the ±12V to ±7V except for the D3.3V which needed an additional heatsink and for the 7V regulators that need heatsink as well. Moreover, they must be two in parallel to bring the total 490mA current with a voltage drop of 5V, from 12V to 7V. In fact, if a single regulator without heatsink had been used it would have reached 200°C. Adding another 7V regulator in parallel, thus splitting in two the current flowing through them, and mounting a heatsink featuring a $25\frac{^\circ C}{W}$ thermal resistance, an acceptable 77°C junction temperature is calculated.

Regulator	I_{out} [mA]	T_j [°C]
+5V	210	67.5
D3.3V	250	68
A3.3V	30	47.5
-5V	120	55.5
7V	245	77
-7V	120	79

Table 5.1: Currents flowing in each regulator and its reached junction temperature

All regulators have been selected in the TO220 package, both for its high temperature performance and to leave space for heatsinking improvements. On their datasheet a thermal junction-ambient resistance in the range of $50 - 65\frac{^\circ C}{W}$ is declared, while a junction-case one of $3 - 5\frac{^\circ C}{W}$ is the usual one. Instead, to provide a stable and clean +1V at multiplier's offset pin, a voltage reference has been used directly connected to the +5V regulator.
For the sake of clarity Figure 5.17 shows the power supply network at a block diagram level.

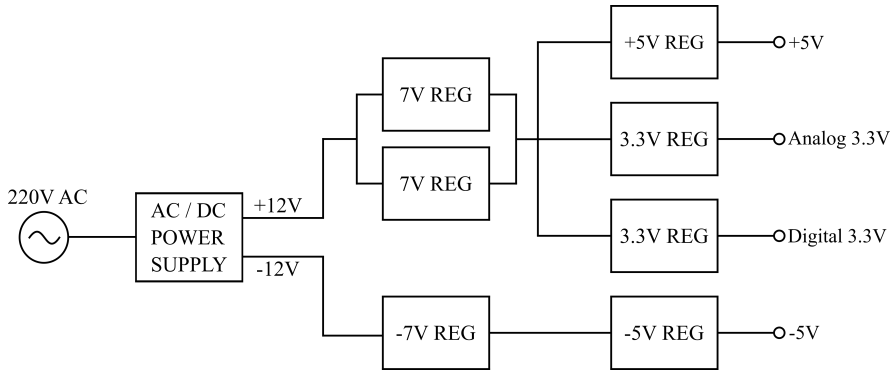

Figure 5.17: Block diagram view of the derived power supply values

5.6.1 Positive power supply

This part features 2 different values, +5V and +3.3V, supplied by 3 regulators, given the choice to split the 3.3V rail in an analog 3.3V and a digital 3.3V one. The +5V regulator is a MC7805 by On Semiconductor which can output up to 1A and sustain a junction temperature up to 150°C, while the 3.3V ones are UA78M33 by Texas Instruments. To calculate junction temperatures two equations[45] have been used: (5.13) is accounting for the bare package and (5.14) in the case of a heatsink:

$$T_j = T_{amb} + \Delta V \cdot I_{out} \cdot R_{j,amb} \tag{5.13}$$

$$T_{j,sink} = T_{amb} + \Delta V \cdot I_{out} \cdot R_{j,c} + R^{sink}_{c,amb} \tag{5.14}$$

From 12V to 5V there is a voltage drop of 7V. In the adverse case of a faulty sensor almost 50mA are drawn from the drivers. In addition to that, MUXs, PGA, analog multiplier, ADC and every OpAmp are supplied by the 5V regulator, thus resulting in an output current of 210mA. Accounting for a T_{amb} of 40°C, T_j of 135°C can be calculated; too close to the maximum rating specification, therefore a heatsink or a previous step down are needed. Trying the first way, just by choosing a heatsink which features a $25\frac{^\circ C}{W}$ thermal resistance, a new $T_{j,sink}$ value of 84°C is inferred. This has not been considered satisfactory, instead by just stepping down the 12V to the previously mentioned 7V, a good 67.5°C junction temperature will be obtained without the additional help provided by a heatsink.
For the digital 3.3V it must be noted that AD9106 and the oscillator IC are

asking, in the worst case, for almost 250mA. In addition to that, if the 12V input are not step down, an almost 9V voltage drop is present, therefore an unacceptable 181.5°C junction temperature is calculated. With the help of a heatsink, instead, the junction should stay at 105°C therefore being inside the rated range. On the other hand, just by stepping down the previous 12V to 7V, a temperature of 100°C can be achieved. This has not been considered enough, so, by combining both heatsink and down stepping to 7V, a temperature of 68°C is calculated, cool enough for a long lifespan. For the analog 3.3V instead, no problem arises since it is connected only to the DDS, sinking no more than 30mA. Its temperatures, therefore, are calculated only in the cases of 12V and 7V input, since heatsinks will never be necessary for this regulator.
To sum up, for the positive rails it is clear that a step down from 12V to 7V is mandatory and, in addition to that, D3.3V needs a heatsink to further cool down the corresponding regulator.

5.6.2 Negative power supply

Only one MC7905 by On Semiconductor has been used for this project. Since the current that it should deliver is around 120mA, with an input voltage of -12V, a T_j of 94.5°C is assessed. Just by stepping down the -12V to -7V a T_j of 55.5°C can be calculated, therefore not needing any heatsink.
For convenience, in Table 5.2 there is a sum up of all the achieved junction temperatures and the different possibilities.

Regulator	I_{out} [mA]	T_j [°C]	$T_{j,sink}$ [°C]	$T_{j,sd}$ [°C]	$T_{j,sink,sd}$ [°C]
+5V	210	135	84	67.5	/
D3.3V	250	181.5	105	100	68
A3.3V	30	57	/	47.5	/
-5V	120	94.5	/	55.5	/

Table 5.2: Junction temperatures summing table, cases with heatsink (sink) and stepdown (sd) are calculated only when deemed useful

To conclude, Table 5.3 is reported, where it is shown a sup up of the most important parameters, their selected or obtained values, and possible ranges.

# of channels	Stimulus Freq	Stimulus Ampl	$BW_{pre\,demod}$
4	4.76Hz - 80MHz	up to 200mV	1MHz

Min signal	$BW_{after\,demod}$	Expected Noise	Current consumption
30nA	100Hz	$< 16.6\mu V_{RMS}$	490mA

Gain	f_{sample}	$f_{sample,\,max}$	SNR_{min}
5 - 625	1kHz	100KHz	41dB

Table 5.3: Sum up of the most relevant features of this electronic board

5.7 Layout

The complete readout system is composed by the Arduino Due and this board, which connects to it like a shield on its top side. In the design phase it was soon clear that a 4 layer board should have been used, then the following subdivision was implemented:

- Top layer for analog connections
- Internal layer 1 used as ground plane
- Internal layer 2 used for power planes
- Bottom layer for digital lines and connections with the Arduino

This sorting mainly aims to place as further as possible digital signals, on the bottom of the board, from the analog ones, which lay on the top side. To further improve decoupling the ground plane was put right under the analog connections one, thus leaving power plane as internal layer 2.

5.7.1 Top Layer

This layer hosts all the active components and is the one devoted to the links between every stage. The possibility of arrangement were not completely up to designer's will, given some constrains arising from the holes to connect with Arduino. In Figure 5.18 it can be seen that not all traces have the same width, an estimate of the current flowing through them was done, then they were made as wide as possible to decrease their resistance, especially

for power lines. Moreover, every active component has a ceramic 100nF capacitor from supply to ground to stabilize that voltage and it is placed as close as possible to component's pin. Some of them, like the AD9106, have a very high number of capacitors requested by the datasheet, therefore some of them were moved to the bottom layer. Some others, like the AD8099, require a 10μF one in parallel to the 100nF to further increase the charge bucket reservoir.

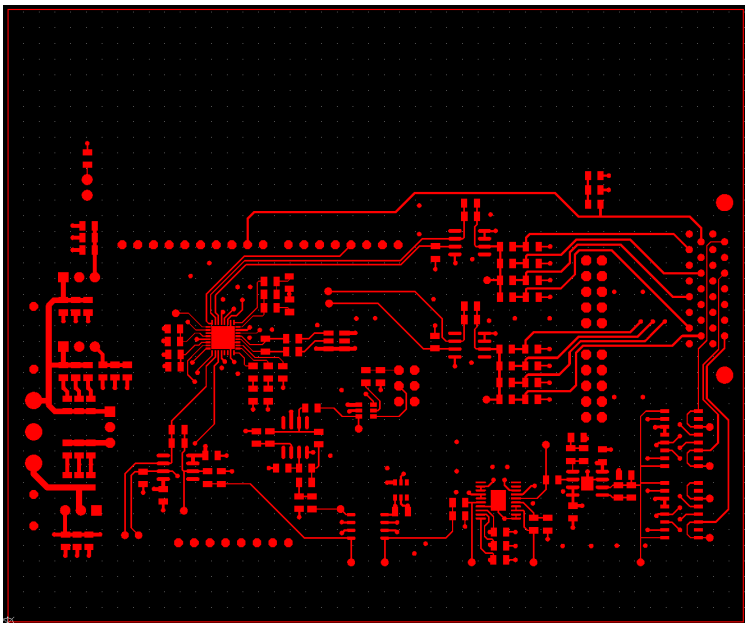

Figure 5.18: Top layer routing and layout

5.7.2 Internal layer 1

This layer is used as a ground plane. It was deemed useful not to make slots or to arrange it in a star-point fashion[46, 47] in order to leave it plain instead, as can be observed in Figure 5.19.
The only cut-outs were made under OpAmps' virtual grounds to better control parasitic capacitances seen toward ground. Furthermore, having placed digital components close together and to their regulator, spurious currents are not expected to be relevant, since, as demonstrated in [48], currents at high frequencies tend to minimize parasitic inductances, thus flowing right under the forward path. In order to let them flow freely, a plain ground is the best way to go, having the foresight of arranging components in such a

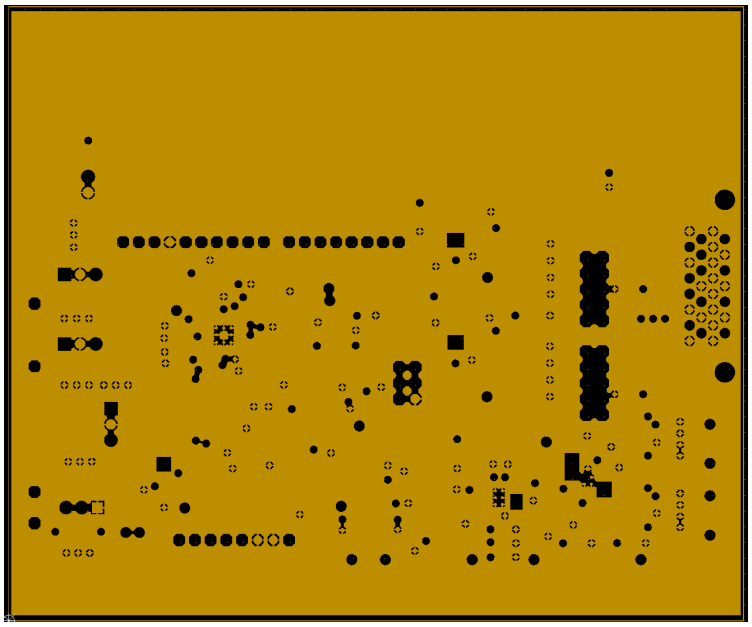

Figure 5.19: Ground plane

way to minimize analog and digital return current crossing points. Going on, it must be noted that this ground and the Arduino one are connected, so to have a common ground potential among PC, Arduino and board.

5.7.3 Internal layer 2

The second inner layer is used to deliver currents to every component, not limiting the path in a trace of narrow width. Instead, in this way, currents can flow in a much lower resistance, thus limiting heating problems. Note that, being analog and digital voltages separated, also their underlying planes are. Thanks to that, analog and digital current crosses are avoided under the AD9106. Figure 5.20 shows what has been discussed right now.

5.7.4 Bottom layer

The bottom layer is used both to host some 100nF capacitors and to route all digital signals. Placing those capacitors right under their component's power pin minimizes their distance, so it implements a more effective decoupling. For digital signals, instead, it has been decided to gather them into three different groups. In Figure 5.21 leftmost, central and rightmost one can be seen, circled respectively in green, pink and red.

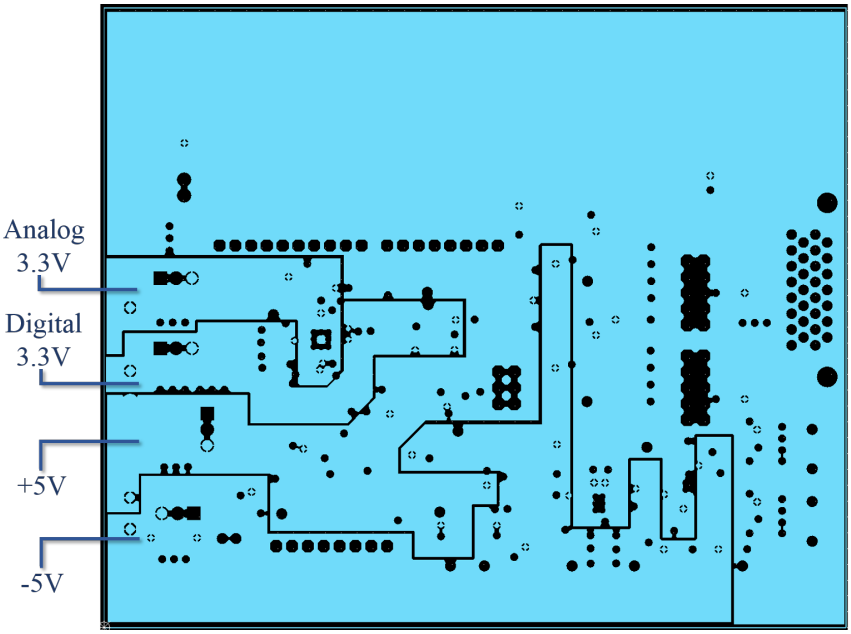

Figure 5.20: Power planes

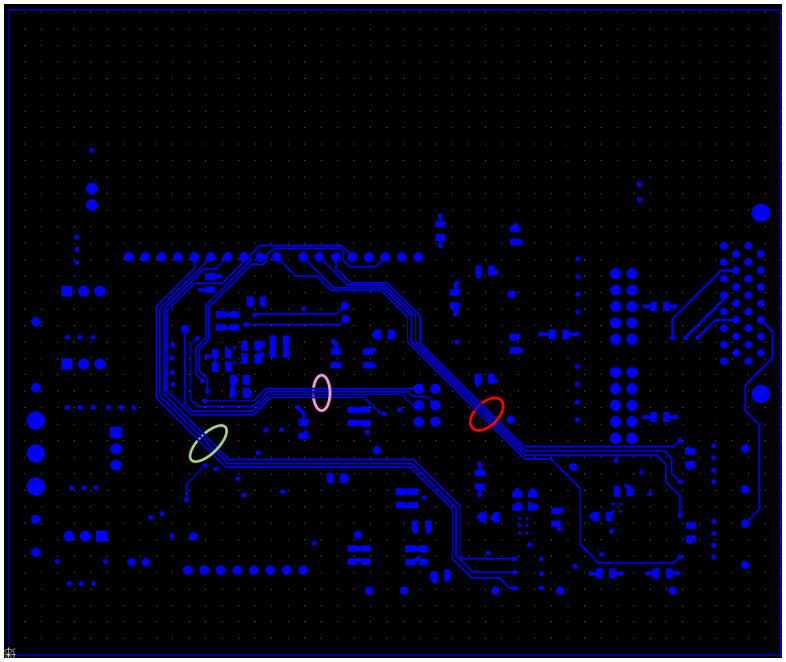

Figure 5.21: Bottom layer routing

The leftmost, green one contains only PGA's digital pins. They are practically a DC signal once they have been set. In future, if a dynamic gain adjustment will be implemented, they are not expected to exceed the 250ms switching time, so they will be at very low frequency anyway. The central, pink horizontal group embeds SPI connections for DDS and ADC, namely clock, master-slave selection and data. In principle, this clock can reach 80MHz, so it was deemed useful letting those lines pass under the digital power plane to preserve the analog part. Last, the rightmost, red set of lines selects MUXs' channel, so it is switching every 250ms, meaning that this is a very low frequency signal as well. In order not to have disturbances given by fast rising times (in the order of 20ns), crossing of those lines with critical analog ones has been avoided in routing phase. Moreover, all those groups of connections have been routed perpendicularly to the analog line crossing them on the top layer to minimize their interaction.

5.8 Firmware and Software

Since this board was developed in order to be placed right on top of an Arduino Due, it is first discussed what is its own purpose, than a more comprehensive view of the project will be obtained explaining MATLAB role. A microcontroller like the Arduino Due is important thanks to its SPI protocol, which allows both DDS and ADC to communicate with it. This way the Due can program DDS's registers to synthesize the correct frequency and can read the data output from the ADC. Moreover, Arduino Due has GPIOs which allow a programmable gain in the PGA stage and, above all, make possible the 250ms switching between channels as previously discussed.
To MATLAB, on the other hand, is committed the management of the communication with Arduino Due, PI motor and above all the human operator. Indeed, this program takes care of the timing synchronization, motor motion, data processing and plotting as well as parameter setting given by human input.

5.8.1 Arduino Due

The decision to use an Arduino Due is mainly to be attributed to the fact that it has superior performances with respect to its predecessors and up to 54 general purpose digital I/O pins, which leave plenty of space for future upgrades and expansions. The Due used in this project mainly takes care of SPI communication with the AD9106 and ADC. To use correctly a DDS, in its initialization, the most important part is to set the tuning word (TW).

This is a 24-bit digital word which, as shown previously in Equation (5.2), determines the output frequency. In Figure 5.22 a very brief extract of the code has been shown.

```
76    short DDS_TW32_add = 0x3E;                              // TW MSB address in hexadecimal code
77    short DDS_TW32_data = (B00000011 << 8) + B00110100;     // TW 16MSB: 8MSB, then bitshift and 8 LSB sum
78    SPI.transfer16(DDS, DDS_TW32_add, SPI_CONTINUE);        // TW MSB communication: address
79    SPI.transfer16(DDS, DDS_TW32_data);                     // TW MSB communication: data
80    short DDS_TW1_add = 0x3F;                               // TW LSB address
81    short DDS_TW1_data = (B10100100 << 8) + B00000000;      // TW LSB data
82    SPI.transfer16(DDS, DDS_TW1_add, SPI_CONTINUE);         // TW LSB communication: address
83    SPI.transfer16(DDS, DDS_TW1_data);                      // TW LSB communication: data
```

Figure 5.22: Extract of the code showing tuning word (TW) initialization

This code aims to implement a f_{DDS} of 1MHz. By substituting this value in Equation (5.2), as well as an f_{CLK} of 80MHz, it has been calculated a DDS_TW of 210 084 in decimal value. Now it can be converted into hexadecimal or binary. Since AD9106 provides a map of every register with its associated binary code, this option has been chosen, therefore, DDS_TW is now 11 0011 0100 1010 0100. Unfortunately, Arduino's "B" operator, which lets the user employ binary numbers, works only on 8 bit words, therefore a slight manipulation with the help of bit shift was necessary. Indeed, the AD9106 can read only words of 32 bits, where it expects 16 bits to specify register address and 16 for the actual data to be written inside of it. In the standard `SPI.h` Arduino library there is a command named `SPI.transfer16()` which allows 16-bit words to be passed, so 2 words per register are needed. For synchronization reasons the parameter `SPI_CONTINUE` is specified, which does not close the communication therefore simulating a 32-bit word. Once AD9106's registers are initialized correctly PGA's gain is programmed just by setting the corresponding pins as outputs and by writing on them a high or low digital level.
In the DDS there are special read-only registers suited to report specific errors. By reading and comparing them to the proper value a diagnosis on calibration state can be done. When there are no errors left the program will go on communicating to MATLAB its state through USB and waiting for the permission to continue. Now, MATLAB communicates with the Arduino to start the actual measurement. The sequence to be followed is standard from the first sensor to the fourth, at least for the moment. For now it is embedded in Arduino program, therefore it can not be changed in the GUI. In a future upgrade this may be implemented, but to keep the program simple and reliable this option was discarded. Arduino reads ADC samples, stores it and changes channel by selecting a different switch inside the MUXs. Once all four channels have been read it passes the obtained data burst to MATLAB. A check on the value of a particular variable is performed and in case

it fails, Arduino starts the reading and switching back from the first sensor. This process repeats until MATLAB passes a specific value to the Arduino which understands that the measurement is over and exits from the routine. To have a visual understanding of what has been discussed Figure 5.24 is reported, where on the left branch there is Arduino's part.

5.8.2 MATLAB

To manage all this project's components it was decided to use MATLAB thanks to its wide support and ease of use. Libraries for this program were available both by Zurich instruments in validation stage and by PI for their stepper motor motion control. Moreover, with this program, it is not very hard to create a simple graphical user interface (GUI) which very much helps people on the field to use this setup. A complete discussion of the code used in MATLAB is out of the scope of this thesis work, anyway, in this section, Figure 5.24 shows a simplified flowchart, which summarizes at a high level the routine.
When starting the program MATLAB asks for some parameters, like measurement time duration and motor motion control. From those values it calculates all the needed parameters to pass to the Arduino like the number of samples. MATLAB manages as well the synchronization, so, when the gasket has been sealed by the chip, MATLAB lets the magnets go in contact with the chip itself and the measurement start. At this point it receives data from Arduino every second, then it processes them and updates the four plots. Whenever a dedicated counter reaches the time limit set at the beginning by the user MATLAB stops the measurement and makes the motor move to open the sealed room.
As can be observed, MATLAB manages both Arduino, data, and PI motor taking care that everything is synchronized correctly. In Figure 5.23, to conclude, the actual GUI is shown.

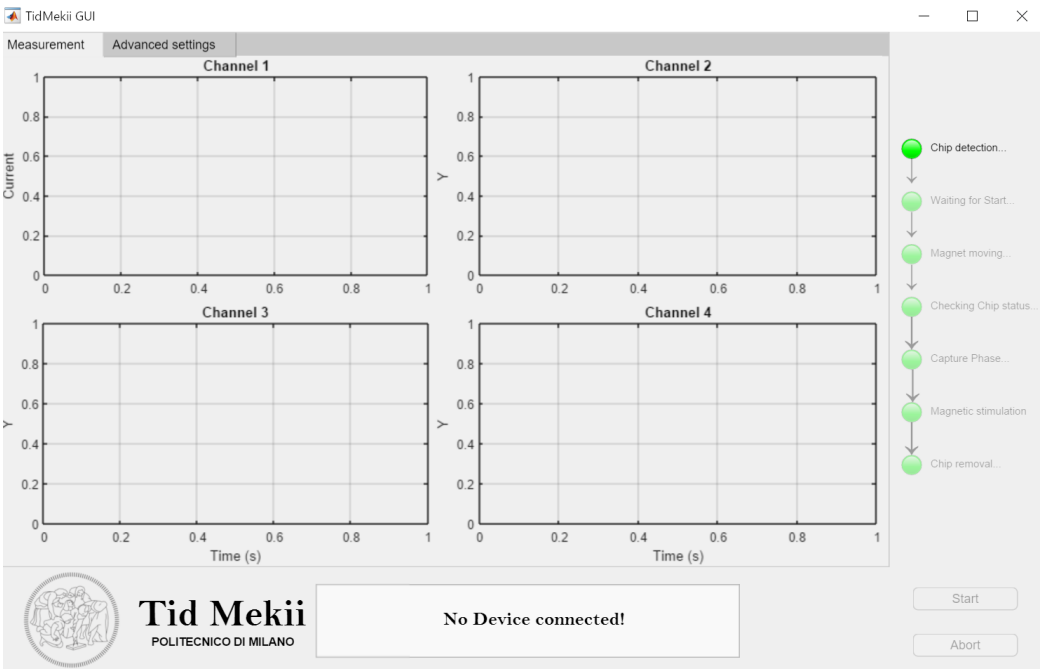

Figure 5.23: Implemented GUI to control the program

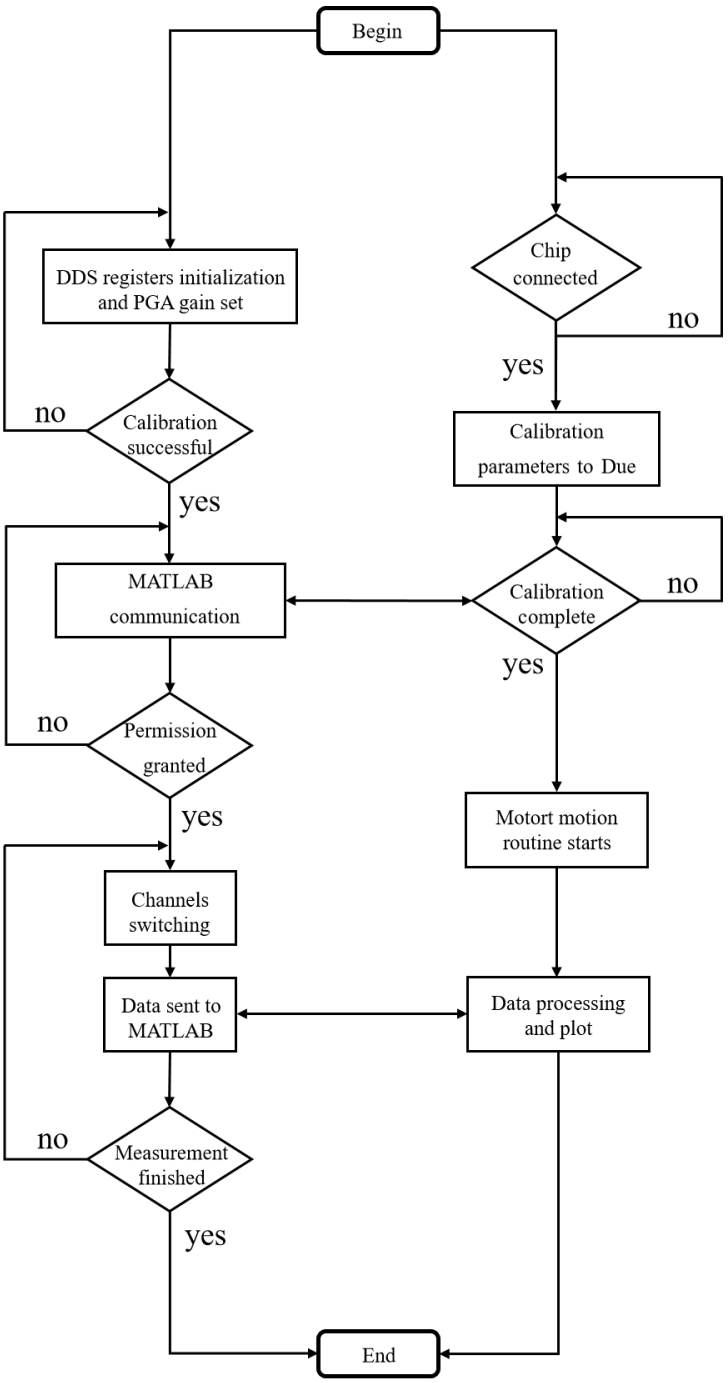

Figure 5.24: Simplified flowchart of the complete program

Chapter 6

Conclusions and perspectives

This thesis work started from a previous one in which both the analytical models of the sensor have been proved and an early experimental validation was performed.
The first part of this work focused on the realization of a chip in order to start the development of a suitable readout electronics. This was indeed the second and last part of the work, where design and realization of the discussed board took place.
To sum up the achieved results it can be said that the realization of a 4 differential channel chip has been carried out: chip resistance is in the order of 100Ω, while traces are in the order of 50Ω and parasitic capacitance is around 100pF. The spacing between pillars is 160μm, while their diameter is 40μm. A resistive plateau shows in the impedance spectrum from 500kHz to more than 100MHz, thus allowing a 1MHz measurement. As far as the electronic board is concerned among its parameters the most important ones are the achieved noise level never exceeding 16.6μV_{RMS}, while the minimum detectable signal is in the order of 30nA. Moreover, it has been designed to cover completely the bandwidth between 1MHz and 10MHz where iRBCs give signal. Since the implemented LIA is analog, signal bandwidth at its digitalization stage is only 100Hz, allowing a sample frequency of 1kHz, upgradable up to 100kHz if needed and the achieved minimum SNR is 41dB.
Tid-Mekii project is of unquestionable relevance and its future possibilities are clear to everyone, indeed it won the 2018 edition of Switch2Product competition. This is a fast and, above all, low cost diagnostic test that can represent the difference between life and death for many people.
From technical project's point of view, it was decided carefully whether to go for a analog or digital way. The former was preferred due to very strict deadlines and cost reasons. Preliminary tests at Sacco hospital are currently scheduled and in February an on-field test in Cameroon is set.

In conclusion, so much work has been done and at least the same must be done in the future, thus, hopefully, many improvements can be implemented to brighten up this project's future.

Bibliography

[1] World Health Organization. *World malaria report 2017*. World Health Organization, 2018.

[2] Coy D Fitch and Phitsamai Kanjananggulpan. "The state of ferriprotoporphyrin IX in malaria pigment." In: *Journal of Biological Chemistry* 262.32 (1987), pp. 15552–15555.

[3] Simão Nunes Paula. "Exploring impedance spectroscopy as a mean of malaria diagnostic". In: (2014).

[4] Tao Sun and Hywel Morgan. "Single-cell microfluidic impedance cytometry: a review". In: *Microfluidics and Nanofluidics* 8.4 (2010), pp. 423–443.

[5] Gregory S Noland, Noelle Briones, and David J Sullivan Jr. "The shape and size of hemozoin crystals distinguishes diverse Plasmodium species". In: *Molecular and biochemical parasitology* 130.2 (2003), pp. 91–99.

[6] Lorena M Coronado, Christopher T Nadovich, and Carmenza Spadafora. "Malarial hemozoin: from target to tool". In: *Biochimica et Biophysica Acta (BBA)-General Subjects* 1840.6 (2014), pp. 2032–2041.

[7] S Hackett et al. "Magnetic susceptibility of iron in malaria-infected red blood cells". In: *Biochimica et Biophysica Acta (BBA)-Molecular Basis of Disease* 1792.2 (2009), pp. 93–99.

[8] *Tid-Mekii*. URL: `http://www.polisocial.polimi.it/wp-content/uploads/2016/07/TID_MEKII.pdf`.

[9] Jeongho Kim et al. "Removal of malaria-infected red blood cells using magnetic cell separators: A computational study". In: *Applied mathematics and computation* 218.12 (2012), pp. 6841–6850.

[10] Surasak Kasetsirikul et al. "The development of malaria diagnostic techniques: a review of the approaches with focus on dielectrophoretic and magnetophoretic methods". In: *Malaria journal* 15.1 (2016), p. 358.

[11] Peter A Zimmerman et al. “Diagnosis of malaria by magnetic deposition microscopy”. In: *The American journal of tropical medicine and hygiene* 74.4 (2006), pp. 568–572.

[12] Dave M Newman et al. “A magneto-optic route toward the in vivo diagnosis of malaria: preliminary results and preclinical trial data”. In: *Biophysical journal* 95.2 (2008), pp. 994–1000.

[13] Ágnes Orbán et al. “Efficient monitoring of the blood-stage infection in a malaria rodent model by the rotating-crystal magneto-optical method”. In: *Scientific reports* 6 (2016), p. 23218.

[14] Jeonghun Nam et al. “Magnetic separation of malaria-infected red blood cells in various developmental stages”. In: *Analytical chemistry* 85.15 (2013), pp. 7316–7323.

[15] Ki-Ho Han and A Bruno Frazier. “Paramagnetic capture mode magnetophoretic microseparator for high efficiency blood cell separations”. In: *Lab on a Chip* 6.2 (2006), pp. 265–273.

[16] Wallace H Coulter. *Means for counting particles suspended in a fluid*. US Patent 2,656,508. Oct. 1953.

[17] Mouhamad Ibrahim et al. “Geometric parameters optimization of planar interdigitated electrodes for bioimpedance spectroscopy”. In: *Journal of Electrical Bioimpedance* 4.1 (2013), pp. 13–22.

[18] John Bertrand Johnson. “Thermal agitation of electricity in conductors”. In: *Physical review* 32.1 (1928), p. 97.

[19] David C Grahame. “The electrical double layer and the theory of electrocapillarity.” In: *Chemical reviews* 41.3 (1947), pp. 441–501.

[20] Marcel Giesbers, J Mieke Kleijn, and Martien A Cohen Stuart. “The electrical double layer on gold probed by electrokinetic and surface force measurements”. In: *Journal of colloid and interface science* 248.1 (2002), pp. 88–95.

[21] Marco Carminati et al. “Towards the impedimetric tracking of single magnetically trailed microparticles”. In: *Systems, Signals & Devices (SSD), 2014 11th International Multi-Conference on*. IEEE. 2014, pp. 1–5.

[22] SE Moulton et al. “Studies of double layer capacitance and electron transfer at a gold electrode exposed to protein solutions”. In: *Electrochimica Acta* 49.24 (2004), pp. 4223–4230.

[23] Andrea Collovini. *Development of an on-chip malaria diagnostic test based on electrical impedance detection*. 2017.

[24] Takaya Sato, Gen Masuda, and Kentaro Takagi. "Electrochemical properties of novel ionic liquids for electric double layer capacitor applications". In: *Electrochimica Acta* 49.21 (2004), pp. 3603–3611.

[25] Alfred S Brown. "A type of silver chloride electrode suitable for use in dilute solutions". In: *Journal of the American Chemical Society* 56.3 (1934), pp. 646–647.

[26] S Takashima, K Asami, and Y Takahashi. "Frequency domain studies of impedance characteristics of biological cells using micropipet technique. I. Erythrocyte". In: *Biophysical journal* 54.6 (1988), pp. 995–1000.

[27] G Kästle et al. "Size effect of the resistivity of thin epitaxial gold films". In: *Physical Review B* 70.16 (2004), p. 165414.

[28] *PoliFAB*. 2018. URL: `http://www.polifab.polimi.it/`.

[29] Livia Calligari. *Development of a magnetic on-chip diagnostic test for malaria*. 2017.

[30] Norman M Osero. "An overview of pulse plating". In: *Plat. Surf. Finish.* 73.3 (1986), pp. 20–22.

[31] John S Chapin. *Sputtering process and apparatus*. US Patent 4,166,018. Aug. 1979.

[32] Paul A Remillard and Michael C Amorelli. *Lock-in amplifier*. US Patent 5,210,484. May 1993.

[33] Zurich Instruments AG. *HF2 User Manual - LabOne Edition*. 2017.

[34] Zurich Instruments AG. *HF2TA Current Amplifier*. 2014.

[35] Molex. *PicoBlade Connector System*. 2018.

[36] *Red Pitaya*. 2018. URL: `http://www.redpitaya.com/`.

[37] Paul Schreiber. "PIC24FJ128GC010 Analog Design Guide". In: (2013).

[38] Pradeep Shinde. "An Overview of Designing Analog Interface With TMS320F28xx/28xxx DSCs". In: ().

[39] Altera. *THDB-ADA User Manual*. 2014.

[40] Analog Devices. "AD835: 250 MHz, voltage output 4-quadrant multiplier". In: *1994, 14s.* ().

[41] Michael Steffes. "Design For A Wideband Differential Transimpedance DAC Output Interface". In: ().

[42] Maxim Integrated. *MAX4621/MAX4622/MAX4623 Datasheet*. 1999.

[43] Hank Zumbahlen. "Sallen-Key Filters". In: *Analog Devices Mini Tutorial MT-22* (2012).

[44] Robert Kiely. “Understanding and Eliminating 1/f Noise”. In: ().

[45] Darvin Edwards and Hiep Nguyen. “Semiconductor and IC Package Thermal Metrics”. In: *Application Report, Texas Instruments, Dallas, TX, Report No. SPRA953B.* (2012).

[46] Hank Zumbahlen. “Staying Well Grounded”. In: *Analog Dialogue* 46.2 (2012), p. 17.

[47] Walt Kester, James Bryant, and Mike Byrne. “Grounding Data Converters and Solving the Mystery of "AGND" and "DGND"”. In: *Analog Devices Tutorial* (2006).

[48] Howard W Johnson, Martin Graham, et al. *High-speed digital design: a handbook of black magic*. Vol. 1. Prentice Hall Upper Saddle River, NJ, 1993.

Ringraziamenti

Concludendo il mio percorso scolastico e accademico, sento di dover ringraziare alcune persone in particolare.
Ovviamente, la prima parola voglio spenderla per i miei genitori, che mi hanno sempre sostenuto e incoraggiato lasciandomi libero nelle mie scelte.
Vorrei poi ricordare i miei nonni, per i quali questo momento è stato motivo di orgoglio prima ancora che arrivasse, tanta era la loro fiducia nella mia riuscita.
Un ringraziamento speciale va anche ai miei amici di Cremona, coi quali sono cresciuto e che hanno saputo aspettarmi pazientemente nei miei momenti di latitanza augurandomi scherzosamente "Buon Natale" a fine Settembre.
Un grazie anche agli amici e amiche (poche, ma buone) del Poli con i quali gli anni di studio sono passati veloci.
Per ultimi, ma solo cronologicamente, i Professori Bertacco, Ferrari e Sampietro per avermi dato modo di partecipare a questo progetto ampliando incredibilmente le mie abilità e permettendomi di vivere un'esperienza di alto livello in termini umani e professionali.
Una menzione speciale al Professor Ferrari, che è stato un riferimento esemplare con i suoi consigli puntuali e lungimiranti.
Infine Marco, che ha saputo seguirmi con attenzione, passione e infinita disponibilità pur non avendo mai un momento libero.
Un grazie anche a tutti i dottorandi del LabSAMP per la generosità con cui hanno condiviso le loro conoscenze.
Grazie davvero a tutti.